Magnetic resonance imaging techniques for pre-clinical lung imaging

Andrea Bianchi

université de BORDEAUX

THÈSE PRÉSENTÉE

POUR OBTENIR LE GRADE DE

DOCTEUR DE

L'UNIVERSITÉ DE BORDEAUX

ÉCOLE DOCTORALE DES SCIENCES DE LA VIE ET DE LA SANTÉ

SPECIALITÉ BIOIMAGERIE

Par Andrea, BIANCHI

MAGNETIC RESONANCE IMAGING TECHNIQUES FOR PRE-CLINICAL LUNG IMAGING

Sous la direction de : Yannick, CRÉMILLIEUX

Soutenue le 28 mars 2014

Membres du jury :

M. QUESSON, Bruno	Université de Bordeaux	Président
M. BARBIER, Emmanuel	Université Joseph Fourier, Grenoble	Rapporteur
M. BERTHAULT, Patrick	CEA – Saclay, Gif sur Yvette	Rapporteur
M. BECKMANN, Nicolau	Novartis Pharma AG, Bâle	Examinateur
M. LUX, François	Université Claude Bernard, Lyon	Examinateur
M. FRANCONI, Jean-Michel	Université de Bordeaux	Invité

Titre : Techniques d'IRM pour l'imagerie préclinique du poumon

Résumé : Dans ce travail, les s´séquences Imagerie par Résonance Magnétique (IRM) radiales à temps d'écho ultra-court (UTE) sont analysées pour évaluer leur potentiel dans l'étude non-invasive de différents modèles expérimentaux de maladies pulmonaires chez la souris. Chez le petit animal, les séquences radiales UTE peuvent efficacement limiter l'impact négatif sur la qualité de l'image dû au déphasage rapide des spins causé par les nombreuses interfaces air/tissu. En plus, les séquences radiales UTE sont moins sensibles aux artefacts de mouvement par rapport aux séquences Cartésiennes classiques. En conséquence, chez le petit animal, les séquences radiales UTE peuvent permettre d'obtenir des images du poumon avec une résolution bien inférieure au millimètre avec des rapports signal/bruit importants dans le parenchyme pulmonaire, tout en travaillant en conditions physiologiques (animaux en respiration spontanée).
Dans cette thèse, il sera démontré que les séquences d'IRM protonique UTE sont outils efficaces dans l'étude quantitative et non-invasive de différents marqueurs distinctifs de certaines pathologies pulmonaires d'intérêt général. Les protocoles développés seront simples, rapides et non-invasifs, faciles à implémenter, avec une interférence minimale sur la pathologie pulmonaire étudiée et, en définitive, potentiellement applicables chez l'homme. Il sera ainsi démontré que l'emploi des agents de contraste, administrés via les voies aériennes, permet d'augmenter la sensibilité des protocoles développés. Parallèlement, dans cette thèse des protocoles suffisamment flexibles seront implémentés afin de permettre l'étude d'un agent de contraste paramagnétique générique pour des applications aux poumons.

Mots clés : Poumon, Imagerie par Résonance Magnétique, Temps d'écho ultra-court, IRM UTE, Asthme, Cancer du poumon, Agents de contraste, Nanoparticules à base de gadolinium, Imagerie optique, Modèles animaux

---

Title : Magnetic resonance imaging techniques for pre-clinical lung imaging

Abstract : In this work, ultra-short echo time (UTE) Magnetic Resonance Imaging (MRI) sequences are investigated as flexible tools for the noninvasive study of experimental models of lung diseases in mice. In small animals radial UTE sequences can indeed efficiently limit the negative impact on lung image quality due to the fast spin dephasing caused by the multiple air/tissue interfaces. In addition, radial UTE sequences are less sensitive to motion artifacts compared to standard Cartesian acquisitions. As a result, radial UTE acquisitions can provide lung images in small animals at sub-millimetric resolution with significant signal to noise ratio in the lung parenchyma, while working with physiological conditions (freely-breathing animals).
In this thesis, UTE proton MRI sequences were shown to be efficient instruments to quantitatively investigate a number of hallmarks in longitudinal models of relevant lung diseases with minimal interference with the lung pathophysiology, employing easily-implementable fast protocols. The synergic use of positive contrast agents, along with an advantageous administration modality, was shown to be a valuable help in the increase of sensitivity of UTE MRI. At the same time, UTE MRI was shown to be an extremely useful and efficacious sequence for studying positive contrast agents in lungs.

Keywords : Lung, Magnetic Resonance Imaging, Ultra-short echo time, UTE MRI, Asthma, Lung cancer, Contrast agents, Gadolinium nanoparticles, Optical imaging, Mice models

---

Centre de Résonance Magnétique des Systèmes Biologiques,
CNRS UMR 5536

”Pour ce qui est de l’avenir, il ne s’agit pas de le prévoir,
mais de le rendre possible”

Antoine de Saint-Exupéry

Contents

Abstract

Magnetic Resonance Imaging for pre-clinical lung imaging

In this work, ultra-short echo time (UTE) Magnetic Resonance Imaging (MRI) sequences are investigated as flexible tools for the noninvasive study of experimental models of lung diseases in mice. In small animals radial UTE sequences can indeed efficiently limit the negative impact on lung image quality due to the fast spin dephasing caused by the multiple air/tissue interfaces. In addition, radial UTE sequences are less sensitive to motion artifacts compared to standard Cartesian acquisitions. As a result, radial UTE acquisitions can provide lung images in small animals at submillimetric resolution with significant signal to noise ratio in the lung parenchyma, while working with physiological conditions (freely-breathing animals).

In this thesis, UTE proton MRI sequences were shown to be efficient instruments to quantitatively investigate a number of hallmarks in longitudinal models of relevant lung diseases with minimal interference with the lung pathophysiology, employing easily-implementable fast protocols. The synergic use of positive contrast agents, along with an advantageous administration modality, was shown to be a valuable help in the increase of sensitivity of UTE MRI. At the same time, UTE MRI was shown to be an extremely useful and efficacious sequence for studying positive contrast agents in lungs.

Keywords: Lung, Magnetic Resonance Imaging, Ultra-short echo time, UTE MRI, Asthma, Lung cancer, Contrast agents, Gadolinium nanoparticles, Optical imaging, Mice models

Techniques d'IRM pour l'imagerie préclinique du poumon

Dans ce travail, les séquences Imagerie par Résonance Magnétique (IRM) radiales à temps d'écho ultra-court (UTE) sont analysées pour évaluer leur potentiel dans l'étude non-invasive de différents modèles expérimentaux de maladies pulmonaires chez la souris. Chez le petit animal, les séquences radiales UTE peuvent efficacement limiter l'impact négatif sur la qualité de l'image dû au déphasage rapide des spins causé par les nombreuses interfaces air/tissu. En plus, les séquences radiales UTE sont moins sensibles aux artefacts de mouvement par rapport aux séquences Cartésiennes classiques. En conséquence, chez le petit animal, les séquences radiales UTE peuvent permettre d'obtenir des images du poumon avec une résolution bien inférieure au millimètre avec des rapports signal/bruit importants dans le parenchyme pulmonaire, tout en travaillant en conditions physiologiques (animaux en respiration spontanée).

Dans cette thèse, il sera démontré que les séquences d'IRM protonique UTE sont outils efficaces dans l'étude quantitative et non-invasive de différents marqueurs distinctifs de certaines pathologies pulmonaires d'intérêt général. Les protocoles développés seront simples, rapides et non-invasifs, faciles à implémenter, avec une interférence minimale sur la pathologie pulmonaire étudiée et, en définitive, potentiellement applicables chez l'homme. Il sera ainsi démontré que l'emploi des agents de contraste, administrés via les voies aériennes, permet d'augmenter la sensibilité des protocoles développés. Parallèlement, dans cette thèse des protocoles suffisamment flexibles seront implementés afin de permettre l'étude d'un agent de contraste paramagnétique générique pour des applications aux poumons.

Mots clés: Poumon, Imagerie par Résonance Magnétique, Temps d'écho ultra-court, IRM UTE, Asthme, Cancer du poumon, Agents de contraste, Nanoparticules à base de gadolinium, Imagerie optique, Modèles animaux

Preface

Motivation The spectrum of pulmonary pathologies is extremely broad and includes, among others, lower respiratory tract infections, chronic obstructive pulmonary diseases, asthma, and respiratory apparatus tumors. According to the World Health Organization surveys these diseases, altogether, represent the first cause of death worldwide [1]. The burden of lung pathologies could be greatly reduced with an effective policy of prevention and early diagnostics, which often results in a positive prognosis.

In the race to improve global health through an early detection of diseases, imaging techniques play a major role since they can provide early diagnostics of pathologies, noninvasive longitudinal follow-ups of the patients, and can help preparing and guiding surgery.

Chest radiography and computed tomography currently represent the gold standard for lung diseases diagnostics. Nuclear medicine imaging techniques (e.g., gamma scintigraphy, positron-emission tomography, single photon-emission computer tomography) have shown to be of significant aid in the validation of X-ray or computed tomography observations, and can provide further information about several lung pathologies (e.g., stage of lung cancer) [2]. Nonetheless, all these *in vivo* imaging techniques imply the exposure of the patient to ionizing radiation. As a consequence, repeated acquisitions are discouraged to reduce the cumulative radiation to which patients are exposed, which has been shown to be associated with an increased risk of developing cancer [3].

In this context, magnetic resonance imaging (MRI) has shown to be especially promising because of its high soft tissue contrast, good spatial resolution, and absence of ionizing radiation [2, 4–6]. MRI was proven to be the most adequate imaging technique for the screening and diagnostics of a number of pathologies in brain, heart or liver. Nevertheless, this consideration cannot yet be applied to the lung, which remains one of the most difficult organs to

image with MRI because of its intrinsic properties [5, 7–9].

In this work, ultra-short echo time (UTE) MRI sequences are investigated as flexible tools for the noninvasive study of experimental models of lung diseases in mice. In small animals, radial UTE sequences can indeed efficiently limit the negative impact on image quality due to the fast spin dephasing caused by the multiple air/tissue interfaces [10, 11]. In addition, radial UTE sequences are less sensitive to motion artifacts compared to standard Cartesian acquisitions [12]. As a result, radial UTE acquisitions can provide lung images in small animals at submillimetric resolution with significant signal to noise ratio in the lung parenchyma, while working with physiological conditions (freely-breathing animals) [13, 14].

Aim The aim of this thesis is to implement, apply and validate MRI techniques dedicated to the investigation and diagnostic of lung diseases, and to the monitoring of drug effects in animal models of pulmonary pathologies. UTE proton MRI sequences are investigated to evaluate their potential in the quantitative and noninvasive study of a number of hallmarks in longitudinal models of relevant lung diseases with minimal interference with the lung pathophysiology. The objective of this work is to develop easily-implementable noninvasive protocols that are fast, simple and potentially translatable to human studies. The possibility of using positive contrast agents to increase the sensitivity of the developed protocols is a main objective of this work. On the other hand, this thesis aims also at the development of imaging protocols flexible enough to guarantee their applicability to the study of a generic paramagnetic contrast agent applied to lungs. Multimodal imaging techniques and conventional *ex vivo* procedures are used to validate MRI results.

The main contributions of this thesis are the following:

- Implementation of a robust method to longitudinally characterize with MRI a murine model of chronic asthma in a completely noninvasive way. The characterization includes both the standard detection of inflammatory fluids and the quantification of the subtle changes that take place in the bronchial walls after bronchial remodeling.

- Implementation of a protocol able to detect lung cancer in a reproducible and precise way. The protocol, validated with complementary techniques (bioluminescence imaging and histology), shows the advan-

tages and limitations of radial UTE sequences in small animal studies compared to standard gradient-echo sequences.

- Implementation of an MRI protocol to study the Nuclear Magnetic Resonance (NMR) properties of T_1-shortening contrast agents. The protocol enables to study the gross biodistribution and elimination pathways of the contrast agent and to test its potential interest in lungs. The imaging protocol can be applied to study any positive contrast agent with special interest for the MRI of the lung.

- Implementation of an MRI pharmacokinetic modelization of the biodistribution of a positive contrast agent in lungs. The MRI protocol is based on the negligibility of the T_2^* effect generated by the contrast medium when an ultra-short echo time is used and it allows to compute the concentration of the contrast agent in the organ of interest. In addition, the protocol permits to obtain quantitative information about the pharmacokinetics of the contrast agent.

- Application of the previously implemented protocols to improve the detection of lung cancer in a mouse model. A detailed comparison between two different administration routes (orotracheal and intravenous) is carried out and the advantages and limitations of both are critically discussed.

Organization The research work of this thesis is organized as a collection of articles, either published or submitted for revision in peer-reviewed journals. Each of them will be introduced in the context of the aforementioned aims and an overall discussion of the results will be provided in the last chapter. Supplementary material related to the thesis research outputs is provided in the appendices to complement the data presented and analyzed in the body of this work.

In chapter 1, the basic concepts and terminology about the functions and anatomy of lungs are introduced. A special attention is given to the description of the main pulmonary pathologies, with a major focus on asthma and lung cancer, the diseases which will be object of investigation throughout the entire work. An overview of the main challenges to image lung with MRI is provided along with a short summary of the main techniques used to encompass these limiting factors. A synopsis of the contrast agents principles and of the state-of-the-art of contrast media applied to lungs is presented as well.

In chapter 2, two tools used throughout the whole thesis are described in detail: the UTE reconstruction program and the ultra-small multimodal rigid gadolinium-based platforms (USRPs). The former was optimized in order to obtain the most accurate reconstruction for the subsequent analysis of UTE MR images with standard medical imaging softwares in chapters 3, 4 and 5. The USRPs have been used to improve the sensitivity of UTE MRI and are largely employed in the work described in chapters 4 and 5.

In chapter 3, the UTE MR imaging technique was applied to longitudinally investigate a chronic murine model of asthma. This study showed for the first time that high-resolution UTE proton MRI of the lungs may allow non-invasive quantification of the main hallmarks of asthma, namely the peribronchial inflammation with airway occlusion by mucus and the bronchial remodeling. The data obtained with MRI successfully correlated with the functional information obtained from plethysmography, used to assess the bronchial hyperresponsiveness.

The same imaging technique was then applied to an orthotopic model of lung tumor in immunodeficient mice. The study showed that UTE MRI is an effective sequence to detect carcinogenic formations in the lung parenchyma. Nevertheless, the need to visualize small metastatic lesions suggested the potential interest in using positive contrast agents to improve UTE MRI sensitivity.

In chapter 4, ultra-small multimodal rigid gadolinium-based platforms were therefore chosen for their interesting characteristics, including their multimodal capacity and their high longitudinal relaxivity. In order to test their MR properties in the lung in conjunction with an optimized T_1-weighted UTE sequence, an intra-tracheal instillation was selected as route of administration. The study of the signal enhancements evolution in time after the administration of the contrast agent allowed detecting the elimination pathway of the administered nanoparticles. The MRI measurements confirmed that the size of the nanoparticle is small enough to ensure a negligible hepatic clearance, making the contrast agent and the instillation protocol good candidates for applications in imaging and treatment of selected lung diseases.

To further exploit the wealth of information which MRI can provide, a protocol for the quantification of the contrast agent concentration in the lung was proposed. Quantitative pharmacokinetics models of tracheally-administered ultra-small rigid platforms were implemented and validated against optical imaging of fluorescent USRPs.

In chapter 5, the nanoparticles and the developed protocol were eventually tested on the lung tumor model in mice mentioned above. The results showed that a significant increase in the contrast-to-noise and signal-to-noise ratios can be observed in the tumor after administration of the nanoparticles. The orotracheal administration was proven to be more effective in the detection of lung tumors, compared to the standard intravenous injection. The localization of the tumor observed with UTE proton MRI was confirmed with complementary imaging modalities such as bioluminescence, fluorescence imaging, and histology.

In chapter 6, the results obtained in this thesis are discussed in the light of the data previously published in scientific literature. The perspectives and limitations of the present work are critically analyzed and some close- and long-term possible applications of the innovative protocols proposed in this thesis are discussed. Finally, in chapter 7, the conclusions of this thesis are presented considering the aforementioned aims.

In appendix A, the patent publication relative to the variety of applications which may potentially arise from the use of the USRPs administered in animals or humans through the airways is introduced and referenced. The patent discusses the interest of these nanoassemblies administered *via* the oral route for the diagnostics and therapeutics of lung diseases. The patent request was submitted in April 2012, before the submission of the articles presented in chapter 4. The work presented in this thesis was the basis for and the natural development of the ideas presented in the patent.

In appendix B, the theranostic potential of the USRPs applied to lung cancer was investigated in mice which underwent xenotransplantation of lung tumor. The pre-clinical study showed that the direct administration of the nanoparticles into the airways before conventional X-ray radiation significantly increased the life-span of mice compared to control mice that did not receive any administration before the radiotherapy. The encouraging result, most probably due to the radiosensitizing properties of the USRPs, can be seen as a first step towards theranostic and image-guided therapy. The work presented in chapter 5 was an important contribution to this work for the investigation about the diagnostic potential of USRPs. In addition, the fluorescence imaging technique presented in this section further validates the results presented in chapter 5.

In appendix C, an invited review about the diagnostic and therapeutic

properties of the USRPs is presented. The work includes part of the results obtained in this thesis along with additional applications to other heterotopic and orthotopic tumor models. The review represents a summary of the results obtained with such a contrast agent up to now and a starting point for future developments.

In appendix D, the synthesis and characterization of the USRPs used in chapters 4 and 5 is presented for sake of completeness.

Résumé

Motivation Le spectre des pathologies pulmonaires est extrêmement vaste et inclut, entre autres, les infections des voies respiratoires inférieures, bronchopneumopathies chroniques obstructives, asthme et tumeurs du système respiratoire. Selon les rapports de l'Organisation Mondiale de la Santé, l'ensemble de ces maladies représente la première cause de mortalité dans le monde [1]. Par ailleurs, la mise en place d'une politique de prévention avec l'aide d'un diagnostic préventif plus efficace pourrait sensiblement améliorer la prise en charge des pathologies liées au poumon.

Dans la course pour améliorer la santé globale à travers la détection précoce des maladies, les techniques d'imagerie jouent un rôle fondamental. En effet ces techniques permettent un diagnostic rapide et précis des pathologies ainsi qu'un suivi non-invasif des patients. Enfin, elles peuvent aider à la préparation et au guidage des interventions.

La radiographie et la tomodensitométrie du thorax sont actuellement les techniques de référence pour le diagnostic des maladies pulmonaires. Les techniques d'imagerie en médecine nucléaire (scintigraphie, tomoscintigraphie par émission de positons, tomographie d'émission monophotonique) se sont révélées être des instruments précieux pour valider les observations faites en radiographie ou tomodensitométrie. En outre, elles peuvent fournir des informations importantes sur plusieurs pathologies (par exemple, le stade d'une tumeur) [2]. Cependant, toutes ces techniques d'imagerie *in vivo* impliquent l'exposition du patient aux radiations ionisantes. Par conséquent, les acquisitions répétées sont déconseillées afin de réduire la dose totale de radiations à laquelle les patients sont exposés. Il a, en effet, été démontré que cela augmente le risque de développement d'un cancer [3].

Dans ce contexte, l'imagerie par résonance magnétique (IRM) est particulièrement prometteuse puisque elle permet d'obtenir un contraste élevé dans les tissus mous et une bonne résolution spatiale sans utiliser des ra-

diations ionisantes [2, 4–6]. Plusieurs études ont déjà démontré que l'IRM est la technique d'imagerie la plus appropriée pour le dépistage et le diagnostic de plusieurs pathologies du cerveau, du cœur et du foie. Cependant, cette considération n'est pas encore valable pour le poumon, qui reste un des organes les plus difficiles à imager avec l'IRM à cause de ses propriétés intrinsèques [5, 7–9].

Dans ce travail, les séquences IRM radiales à temps d'écho ultra-court (UTE) sont analysées pour évaluer leur potentiel dans l'étude non-invasive de différents modèles expérimentaux de maladies pulmonaires chez la souris. Chez le petit animal, les séquences radiales UTE peuvent efficacement limiter l'impact négatif sur la qualité de l'image dû au déphasage rapide des spins causé par les nombreuses interfaces air/tissu [10, 11]. En plus, les séquences radiales UTE sont moins sensibles aux artefacts de mouvement par rapport aux séquences Cartésiennes classiques [12]. En conséquence, chez le petit animal, les séquences radiales UTE peuvent permettre d'obtenir des images du poumon avec une résolution bien inférieure au millimètre avec des rapports signal/bruit importants dans le parenchyme pulmonaire, tout en travaillant en conditions physiologiques (animaux en respiration spontanée) [13, 14].

Aim L'objectif de ce travail de thèse est d'implémenter, d'appliquer et de valider des techniques IRM dédiées à l'investigation et au diagnostic de maladies pulmonaires ainsi qu'au suivi des effets de molécules pharmaceutiques dans des modèles de pathologies du poumon. Les séquences d'IRM protonique à temps d'écho ultra-court seront analysées pour évaluer leur potentiel dans l'étude quantitative et non-invasive de différents marqueurs distinctifs de certaines pathologies pulmonaires d'intérêt général. Ces études seront effectuées sur des modèles animaux avec un suivi dans le temps. L'objectif de cette thèse est ainsi de développer des protocoles simples, rapides et non-invasifs, faciles à implémenter, avec une interférence minimale sur la pathologie pulmonaire étudiée et, en définitive, potentiellement applicables chez l'homme. En outre, la possibilité d'utiliser des agents de contraste pour augmenter la sensibilité des protocoles développés est un des objectifs principaux de ce travail. Parallèlement, cette thèse a pour objectif supplémentaire l'implémentation de protocoles suffisamment flexibles pour permettre l'étude d'un agent de contraste paramagnétique générique pour des applications aux poumons. Les techniques d'imagerie multimodales et les procédures conventionnelles *ex vivo* seront utilisées dans ce travail de thèse pour valider les résultats obtenus par IRM.

Les principales contributions de cette thèse sont les suivantes :

- Implémentation d'une méthode robuste et complètement non-invasive pour la caractérisation longitudinale par IRM d'un modèle murin d'asthme chronique. La caractérisation inclut la détection standard des zones d'inflammation ainsi que la quantification de subtiles modifications qui ont lieu dans la paroi bronchique suite au remodelage bronchique.
- Implémentation d'un protocole capable de détecter la tumeur du poumon de façon précise et reproductible. Ce protocole, validé au moyen de techniques complémentaires (bioluminescence et histologie), montre les avantages et les limites des séquences radiales UTE chez le petit animal par rapport aux séquences classiques à écho de gradient.
- Implémentation d'un protocole IRM pour étudier les propriétés de la résonance magnétique nucléaire des agents de contraste qui sont responsables du raccourcissement du temps de relaxation longitudinal T_1. Le protocole permet d'étudier la biodistribution générale et les voies d'élimination de l'agent de contraste ainsi que de tester son intérêt potentiel dans les poumons.
- Implémentation d'un protocole d'IRM pour la modélisation pharmacocinétique de la biodistribution d'un agent de contraste positif dans les poumons. Le protocole IRM se base sur le fait que l'effet T_2^* généré par l'agent de contraste est négligeable quand un temps d'écho très court est utilisé. Ce protocole permet de calculer la concentration de l'agent de contraste dans l'organe d'intérêt et d'obtenir des informations quantitatives sur la pharmacocinétique de l'agent.
- Application des protocoles précédemment développés afin d'améliorer la détection de la tumeur du poumon dans un modèle murin. Une comparaison entre deux différentes modalités d'administration (intratrachéale et intraveineuse) a été effectuée et les limites de chacune sont discutées en portant un regard critique.

Organization Dans cette thèse, le travail de recherche est organisé à la manière d'une collection d'articles scientifiques. Certains sont déjà publiés tandis que d'autres ont été soumis dans des journaux de peer-review et sont maintenant sous révision. Chacun de ces articles sera introduit dans le contexte des objectifs mentionnés précédemment et une discussion générale des résultats sera proposée dans le dernier chapitre. Afin de compléter les données présentées et analysées, des documents supplémentaires relatifs aux résultats

scientifiques de cette thèse seront proposés en annexe.

Dans le chapitre 1, les concepts principaux et la terminologie sur les fonctions et l'anatomie des poumons seront introduits. Les pathologies pulmonaires principales y seront décrites avec une attention toute particulière pour l'asthme et le cancer du poumon. Ces deux maladies feront l'objet du travail d'investigation présenté dans cette thèse. Enfin, une vue d'ensemble des principaux défis à surmonter pour obtenir une image de poumon de bonne qualité par IRM sera aussi exposée, ainsi qu'un bref résumé des techniques couramment utilisées pour surmonter les facteurs limitant les applications de l'IRM pulmonaire.

Dans le chapitre 2, deux outils utilisés dans tout le travail de thèse seront présentés en détail : le programme de reconstruction UTE et des nanoparticules multimodales ultrafines à base de gadolinium (USRPs, ultra-small rigid platforms). Le premier outil a été optimisé dans le but d'obtenir une reconstruction précise des images IRM UTE et pour l'analyse par des logiciels standards d'analyse d'imagerie médicale dans les chapitres 3, 4 et 5. Le deuxième outil sera utilisé pour améliorer la sensibilité de l'IRM UTE et sera largement employé dans les travaux décrits dans les chapitres 4 et 5.

Dans le chapitre 3, les techniques d'IRM radiales à temps d'écho ultracourt seront appliquées à l'étude longitudinale d'un modèle d'asthme chronique chez la souris. Cette étude montrera, pour la première fois, que l'IRM protonique UTE à haute résolution du poumon permet la quantification des facteurs distinctifs de l'asthme de manières non-invasive, c'est-à-dire l'inflammation peribronchique avec occlusion liée à la présence de mucus ainsi que le remodelage bronchique. Les données obtenues par IRM seront corrélées avec succès aux informations fonctionnelles obtenues par la pléthysmographie, utilisée pour évaluer l'hyperréactivité bronchique.

Une technique semblable sera ensuite appliquée dans un modèle orthotopique de tumeur pulmonaire chez la souris immunodéficiente. L'étude montrera que l'IRM UTE est une séquence efficace pour la détection des formations carcinogènes dans le parenchyme pulmonaire. Cependant, la nécessité de visualiser les petites lésions métastatiques suggérera l'intérêt potentiel des agents de contraste positifs pour améliorer la sensibilité de détection de l'IRM UTE.

Dans le chapitre 4, des nanoparticules ultrafines à base de gadolinium seront alors utilisées pour leurs caractéristiques particulières telles que leur re-

laxivité longitudinale très élevé et leur capacité multimodale. Afin de mesurer leurs propriétés RM dans le poumon conjointement avec une séquence UTE optimisée et fortement pondérée en T_1, une instillation intratrachéale sera employée comme voie d'administration. L'étude de l'évolution du rehaussement du signal en fonction du temps après administration de l'agent de contraste montrera la possibilité de détecter les voies d'élimination des nanoparticules. Les observations IRM confirmeront, en outre, que la taille des nanoparticules est suffisamment réduite pour assurer une clairance hépatique négligeable. Ces résultats démontreront donc que cet agent de contraste administré selon le protocole d'instillation est un bon candidat pour le développement d'applications d'imagerie et le traitement thérapeutique de certaines maladies pulmonaires.

Pour davantage exploiter la richesse des informations fournies par l'IRM, un protocole de quantification de la concentration de l'agent de contraste sera proposé. De plus, des modèles pharmacocinétiques quantitatifs des nanoparticules administrées intratrachéalement seront implémentés et validés à travers l'utilisation de l'imagerie par fluorescenceeffectuée grâce aux propriétés multimodales des USRPs.

Dans le chapitre 5, les nanoparticules et le protocole développé seront enfin appliqués au modèle de tumeur pulmonaire décrit ci-avant. Les résultats montreront qu'une augmentation significative des rapports signal/bruit et contraste/bruit peut être atteinte suite à l'administration des nanoparticules. Il sera par ailleurs montré que l'administration intratrachéale est plus efficace qu'une administration intraveineuse classique pour la détection des tumeurs. La localisation de la tumeur par IRM UTE sera confirmée avec l'aide de différentes techniques d'imagerie (bioluminescence, fluorescence) et de l'histologie.

Dans le chapitre 6, les résultats obtenus pendant ce travail de thèse seront discutés à la lumière des connaissances disponibles dans la littérature scientifique. Les perspectives tout comme les limites de ce travail seront analysées avec un regard critique. De plus, ces protocoles innovants ainsi présentés feront alors l'objet d'une discussion dans le cadre de plusieurs applications à court et long terme. Enfin, dans le chapitre 7, les conclusions de cette thèse seront proposées en considérant les objectifs susmentionnés.

Dans l'annexe A, un brevet relatif aux nombreuses applications potentielles pouvant être développées sur l'administration par voie respiratoire des USRPs chez la souris ou l'homme est introduit et référencé. Le brevet

expose l'intérêt de ces nanoparticules administrées par voie intratrachéale pour le diagnostic et la thérapie des maladies pulmonaires. La demande de brevet a été soumise au mois d'avril 2012, avant la soumission des articles présentés dans le chapitre 4. Les travaux de cette thèse sont basés sur les idées présentées dans ce brevet et en sont le développement naturel.

Dans l'annexe B, le potentiel théranostique des USRPs appliquées à la tumeur du poumon sera investigué sur le modèle de cancer pulmonaire discuté dans les chapitres 4 et 5. L'étude préclinique montrera que l'administration directe des nanoparticules dans les voies ariennes avant radiothérapie conventionnelle augmente significativement la survie des souris par rapport à celles qui reçoivent la radiothérapie sans administration préliminaire des nanoparticules. Le résultat encourageant, probablement lié aux propriétés radiosensibilisantes des USRPs, peut être vu comme un premier pas vers la théranostic et la thérapie guidée par imagerie. Le travail présenté dans le chapitre 5 constitue une contribution importante au manuscrit présenté dans cette annexe en ce qui concerne l'investigation du potentiel diagnostique des USRPs. En outre, l'imagerie par fluorescence présentée dans cette annexe valide d'autant plus les résultats présentés dans le chapitre 5.

Dans l'annexe C, une revue invitée sur les propriétés diagnostiques et thérapeutiques des USRPs sera présentée. Le manuscrit contient une partie des résultats présentés dans cette thèse ainsi que des applications supplémentaires des USRPs dans d'autres modèles hétérotopiques et orthotopiques de tumeur. Cette revue représente une synthèse des résultats obtenus avec cet agent de contraste jusqu'à présent et un point de départ pour de futurs développements.

Dans l'annexe D, la synthèse et la caractérisation des USRPs utilisées dans les chapitres 4 et 5 sont présentées par souci d'exhaustivité.

List of Figures

List of Acronyms and Abbreviations

ADC Analog to Digital Converter

BHR Bronchial Hyperresponsiveness

BLI Bioluminescence Imaging

BW Bandwidth

CNR Contrast-to-Noise Ratio

COPD Chronic Obstructive Pulmonary Disease

cRAD Cyclic arginine-alanine-aspartic acid

cRGD Cyclic arginine-glycine-aspartic acid

CT Computed Tomography

Cy Cyanine dye

DOTA 1,4,7,10-tetraazacyclododecane-1,4,7,10-tetraacetic acid

ECG Electrocardiogram

EPR Enhanced Permeability and Retention

FA Flip Angle

FFT Fast Fourier Transform

FID Free Induction Decay

FLASH Fast Low-Angle Shot

FOV Field Of View

FRI Fluorescence Imaging

FT Fourier Transform

HD Hydrodynamic Diameter

HES Haematoxylin-Eosin-Safran

HP Hyperpolarized

ICC Interclass Correlation Coefficient

ID Injected Dose

IRM Imagerie par Résonance Magnétique

IS Inner Sphere

LPS Lipopolysaccharide

MEMRI Manganese-enhanced Magnetic Resonance Imaging

MR Magnetic Resonance

MRI Magnetic Resonance Imaging

NMR Nuclear Magnetic Resonance

NMRD Nuclear Magnetic Resonance Dispersion

NSCLC Non-Small-Cell Lung Cancer

OE Oxygen-enhanced

OS Outer Sphere

OVA Ovalbumin

PBSI Peribronchial Signal Index

Penh Enhanced Pause

PET Positron Emission Tomography

PK Pharmacokinetic

PR Projection Reconstruction

PS Peribronchial Signal

RES Reticuloendothelial System

RF Radiofrequency

RGD Arginine-glycine-aspartic acid

ROI Region Of Interest

SCLC Small-Cell Lung Cancer

SD Standard Deviation

SE Signal Enhancement

SEM Standard Error of the Mean

SNR Signal-to-Noise Ratio

SPECT Single-Photon Emission Computed Tomography

SPIO Super Paramagnetic Iron Oxide

TE Echo Time

TR Repetition Time

TRE Typical Respiratory Epithelium

USPIO Ultra-small Super Paramagnetic Iron Oxide

USRP Ultra-Small Rigid Platform

UTE Ultra-short Echo Time

WHO World Health Organization

1 Introduction

This chapter will provide the readers with the basic concepts and terminology about the functions and anatomy of lungs. In view of the in vivo pre-clinical studies presented in this work, a special attention will be given to the differences between rodents and human's respiratory systems. In addition, the main pulmonary pathologies will be reviewed, with special focus on asthma and lung cancer, the diseases which will be object of investigation in the next chapters.

An overview of the main challenges to image lung with MRI will be provided along with a short summary of the main techniques used to encompass these limiting factors.

Finally, a synopsis of the contrast agents principles and of the state-of-the-art of contrast media applied to lungs will be presented.

1.1 Anatomopathology of lung

1.1.1 Lung anatomophysiology and morphology

The lung is the essential respiration organ in air-breathing animals. Its principal function is to fulfill gas exchanges, transporting oxygen from the atmosphere to the bloodstream and removing carbon dioxide from the blood circulation. In addition, the lungs carry out other functions like the metabolization of some compounds and the filtration of undesired materials from the circulation; moreover, it acts as a reservoir for blood and as a blood pH balance [15].

1.1.1.1 Lung structure and physiology

In order to perform these physiologic functions, a specific architecture of the lung is needed. Even though this differs between species, many structural components remain consistent among animals [16–18]. In reptiles, birds and mammals, respiration takes place through a sequence of steps where air is brought into the lungs through the airways. Since the diffusion of a gas

through a sheet of tissue is proportional to the area of the sheet and inversely proportional to its thickness (Fick's law of diffusion), commonly the blood-gas barrier is exceedingly thin and has an internal total area which is much larger than the outer surface of the lung (between 50 and 100 m^2 in humans) [15]. Such enormous surface is achieved through a complex branching pattern of the tracheobronchial tree.

The airways consist in a series of branching conducting tubes, which become narrower, shorter and more numerous as they penetrate deeper into the lung. As shown in Figure 1.1 they can be divided into two zones: the *conducting airways* and the *respiratory ones*. The conducting zone, whose function

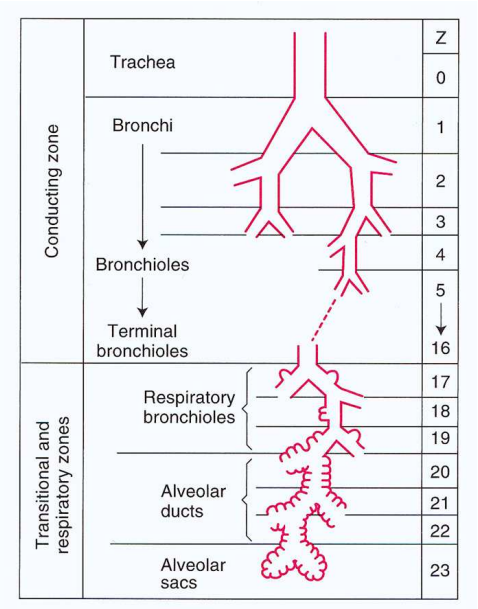

Figure 1.1: Schematic representation of the tracheobronchial tree. The major bronchi, bronchioles, and terminal bronchioles make up the conducting zone, while the respiratory bronchioles, alveolar ducts, and alveolar sacs make up the transitional and respiratory zones. Z denotes the airway generation. Reprinted from [15].

is to transport the inspired air to the gas-exchanging regions of the lungs, is formed by the trachea which divides into the bronchi, bronchioles and terminal bronchioles. The respiratory zone, where the gas-exchange occurs, begins when the terminal bronchioles divide into the respiratory bronchioles and eventually to the alveolar ducts, which are lined with alveolar sacs (*alveoli*). Alveoli associated with the respiratory airways and with the more distal alveolar sacs constitute the lung *parenchyma* [19].

The portion of the cardiovascular system which carries deoxygenated blood away from the heart, to the lungs (via the pulmonary artery), and returns oxygenated blood back to the heart (via the pulmonary veins) constitutes the pulmonary circulation. The pulmonary blood vessels branch from

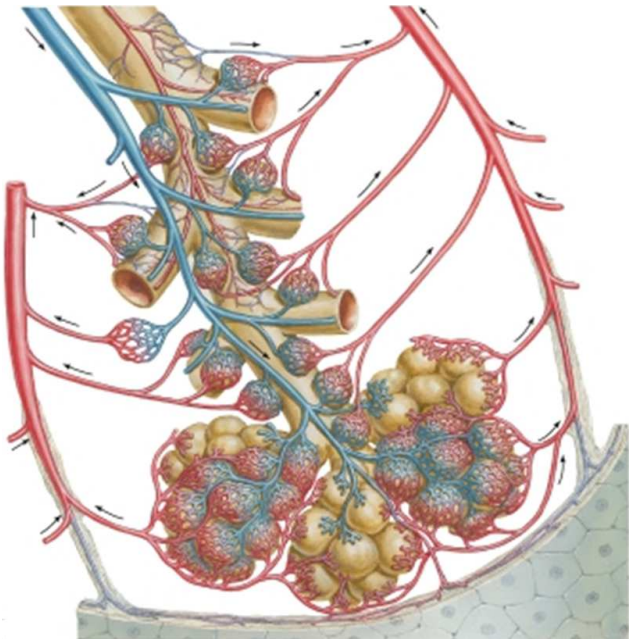

Figure 1.2: Terminal alveoli connected to the network of the capillary system. Alveoli are in contact with capillaries. The thin barrier between the alveolar and the capillary walls allows a rapid exchange of oxygen and carbon dioxide. Adapted from [20].

the pulmonary artery accompanying the tracheobronchial tree deep into the respiratory zone. The smallest branches of the cardiovascular system, the *capillaries*, form a dense network of short interconnecting segments which cover and embed the alveoli, providing an efficient arrangement for gas exchange, as shown in Figure 1.2 [15].

From a mechanical point of view, the respiration in mammals is made possible thanks to several muscles: the diaphragm, the intercostal and accessory muscles, and the abdominal muscles. During inhalation, the diaphragm is the most important muscle. Briefly, when it contracts, it moves in the inferior direction, thus enlarging the volume of the thoracic cavity. The decrease of the internal pressure generates a gradient of pressure which allows air to enter the lungs. During the inspiration phase, alveoli expand in volume, resulting in an overall lower parenchyma density (Figure 1.3a).

During the expiration phase, the diaphragm relaxes, lung and chest wall

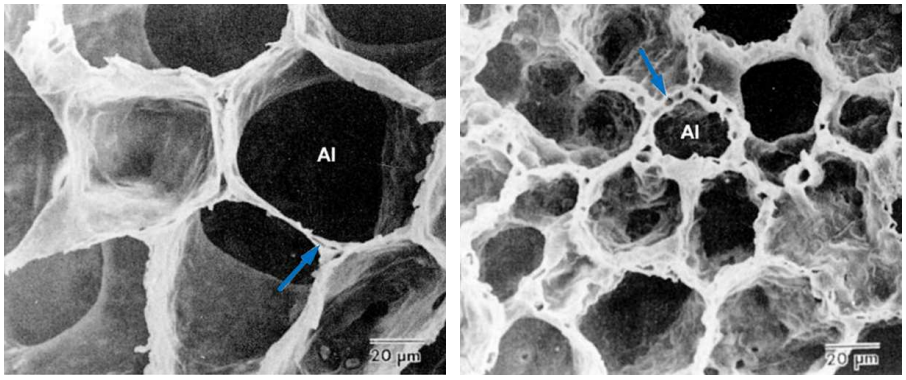

(a) Inspiration phase (b) Expiration phase

Figure 1.3: Scanning electron microscope view of lung alveoli, magnified × 750, showing the way in which their shape is retained as their size alters with changes in lung volume. The blue arrows underline the changes in capillaries shape, which varies proportionally to the degree of stretching undergone by the alveolar walls. Adapted from [21]

return to their equilibrium position because of elastic recoil. The decrease in lung volume and the increase in the alveoli pressure generate the flow of air from the lungs to the atmosphere, increasing the parenchyma density (Figure 1.3b) [15, 19].

1.1.1.2 Lung morphology

The airway wall can be considered as being composed of inner and outer layers, the former extending from the *lumen* to the outermost layer of *smooth muscle* and the latter from the smooth muscle to the airway parenchymal boundary, as shown in Figure 1.4.

The basic morphology of lung varies while moving from the conducting to the respiratory zone, as schematically shown in Figure 1.5. The conducting airways are characterized by a surface *epithelium* largely composed of ciliated and secretory cells (e.g., goblet cells), overlying subepithelial tissue that consists predominantly of connective tissues and glands. The proportion and type of these elements vary at different levels of the conducting system [19].

The tracheal and proximal bronchial epithelia are composed predominantly of columnar ciliated and goblet cells, attached to the underlying basal lamina. These cells are attached to one another by tight junctions, forming a barrier physically impermeable to most substances [9, 19].

The subepithelial tissue can be subdivided into a *lamina propria* and a *submucosa*, consisting of all the remaining airway tissue.

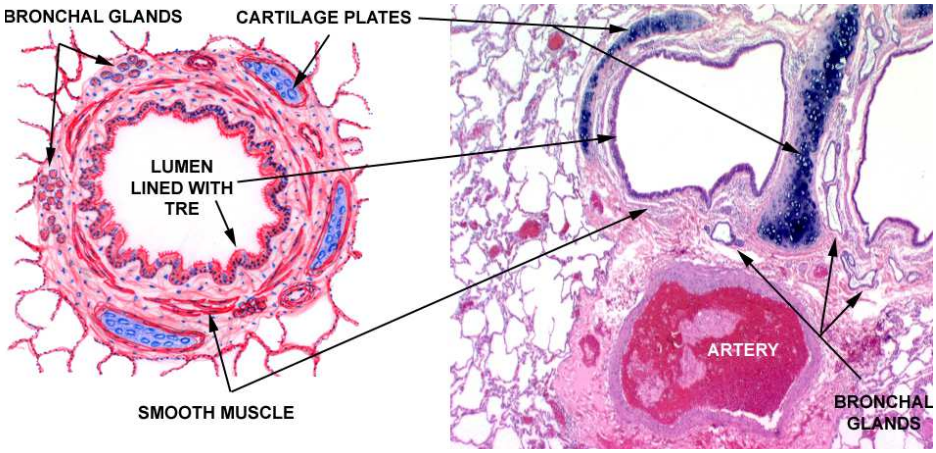

Figure 1.4: Schematic diagram and real image of a medium-sized bronchus. The cartilage reinforcement is clearly visible in dark blue. In the wall of the bronchus it is possible to recognize the smooth muscle. The lining of all bronchi is the typical respiratory epithelium (TRE). In the image on the right it is possible to observe one of the large arteries that run alongside the bronchi. Numerous smaller blood vessels are present among the profiles of the gas exchange areas. Bronchioles have a similar structure but do not present cartilage plates since, when the airways diameter is smaller, smooth muscle in the wall has sufficient tone to resist collapse [22].

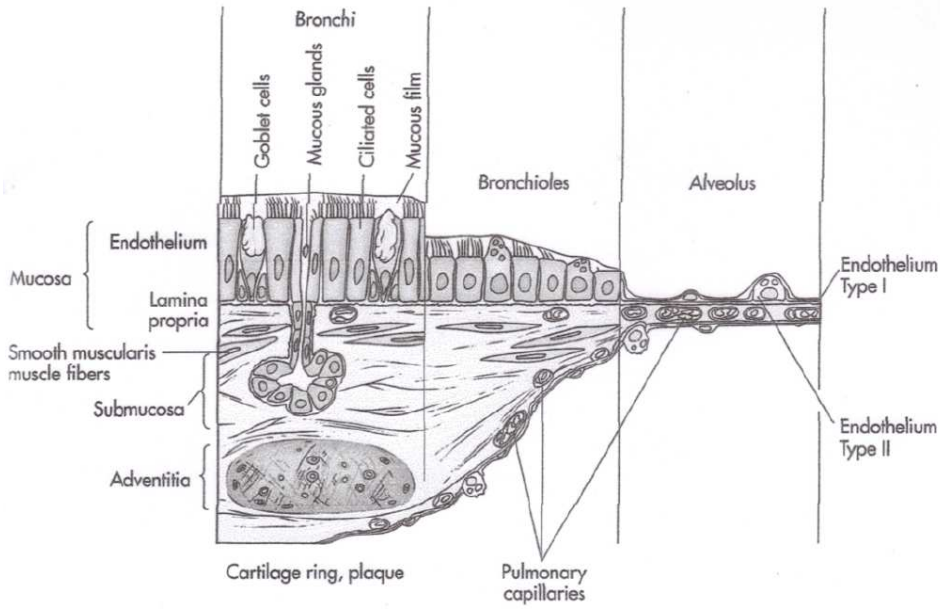

Figure 1.5: Tissue layers of the tracheobronchial tree. Reprinted from [23].

The lamina propria consists principally of a network of capillaries, of reticular fibers, and bundles of elastic and nerve fibers. These fibers are believed to help transmit to the more rigid and stronger cartilaginous fibrous tissue the tension that arises in the airway epithelium and lung parenchyma during breathing [9, 19].

The submucosa contains cartilage, muscle, and other supportive connective tissue elements, including the loose connective tissue known as *adventitia* (whom mainly serves as a support for trachea and bronchi). The majority of the tracheobronchial glands are located in the submucosa and they are almost absent in the smallest bronchi and bronchioles. These glands are mainly responsible to secrete mucus. A variety of substances that are potentially important in local airway defense are also secreted by serous cells [9, 19].

Moving towards the respiratory zone, the surface of respiratory bronchioles is lined by cuboidal epithelium that gradually decreases in extent as the number of alveoli increases. Bronchiolar-type epithelium and lamina propria are absent in alveolar ducts [9, 19].

Alveoli are demarcated by septa composed of a continuous layer of epithelial cells overlying a thin interstitium. The interstitium contains capillaries involved in gas exchange (Figure 1.3), as well as connective tissue and a variety of cells responsible for maintaining alveolar shape and defense. Of particular interest is their secretion of surfactant, a phospholipid which forms an extremely thin (4 nm) layer of material that covers the alveolar epithelial surface and is responsible to reduce the alveoli surface tension, preventing them from collapsing [15, 19].

1.1.1.3 Defense system

Letting aside the first-pass metabolism constituted by the nasopharyngeal anatomy (able to stop particles with size $\geq$ 2-3 μm), lungs have several defense mechanisms to clean and protect themselves from external potentially harmful pathogens. Some of the most relevant of such mechanisms include the *mucociliary clearance* , the *epithelial barrier* , and the *phagocytic system* [24].

The mucociliary clearance is the removal of impacted particles from the terminal bronchioles to the trachea by the ciliary beats of epithelial cells in the mucus of bronchi. The mucus acts as a barrier for bacteria as well.

Epithelial cells provide a mucosal barrier (with antimicrobial properties) and contribute to the mucociliary clearance function just mentioned. At the same time, lining the luminal surface of the airways and being tightly attached one to the other, they form a physical barrier between the luminal space and

the pulmonary parenchyma. Similarly, the alveolar epithelial cells strongly contribute to pulmonary host defense through the surfactant.

Many cells concerned with airways defense are found in the lungs, including lymphocytes, dendritic cells, and mast cells [19, 24]. Nevertheless, *macrophages* are the resident mononuclear phagocytes of the lung which provide the first line of defense against organisms or particles reaching the lower airways. In a normal lung, they account for about the 95% of all the nonepithelial cells in lung parenchyma [19]. Even though still matter of debate, it is acknowledged the possibility that pulmonary macrophages have different functional capabilities. For this reason they are often divided in several groups on the basis of their anatomic location [19, 24, 25]. Commonly the following groups are distinguished: (a) the airway macrophages, situated on the epithelial lining of conducting airways; (b) the alveolar interstitial macrophages; (c) the alveolar surface macrophages; (d) the intravascular macrophages, located adjacent to the capillary endothelial cells; and (e) the pleural macrophages.

Finally, depending on the load of pathogens, various non-resident effector cells can be recruited. For example, *eosinophils* are abundant in the infiltrates of late phase reactions and contribute to many of the pathological processes in allergic diseases whereas the recruitment of *neutrophils* is a major component of the protective host response to bacterial infections [24].

1.1.1.4 Rodents and human's lungs comparative anatomy

In both rodents and humans, the right and the left lungs are enveloped by a thin layer of connective tissue (the *visceral pleura*), which extends into the parenchyma, dividing it into several lobes. Nevertheless, at this level, substantial structural differences can be found between the two orders (*Rodentia* and *Primates*). In mice (Figure 1.6a) and rats the left lung consists of one single lobe whereas the right one consists of four lobes (superior, middle, inferior and post-caval lobes) [26]. Conversely, as shown in Figure 1.6b, human's left lung is composed of two lobes (upper and lower) while the right side is divided into three lobes (upper, middle, and lower) [15].

The total capacity of mouse lungs has been reported to be about 1 ml, compared to 10 ml of the rat and 6,000 ml of a human. Mouse lungs have fewer respiratory bronchioles and airways generations (13-17 generations) than human lungs (17-21 generations) [27, 28]. It has also been found that, while the branching pattern in humans is dichotomous (that is, the parent branch divides into two parts), in rodents monopody (a small segment branching off from the main stem) is commonly observed [16, 27, 29]. The parenchyma in

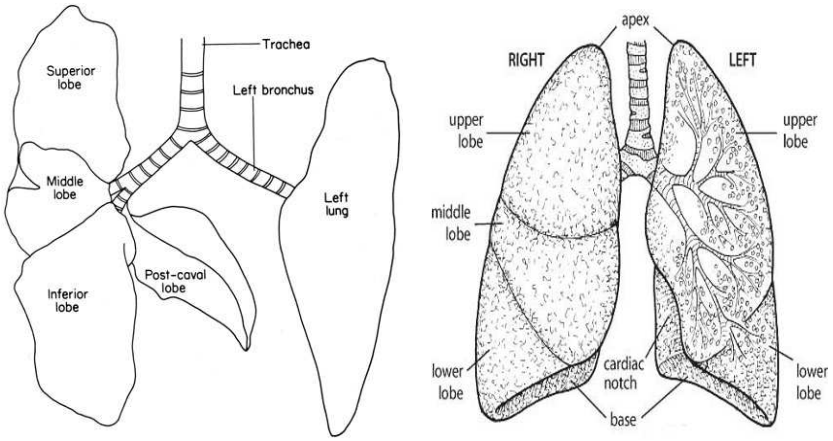

(a) Mouse lung (b) Human lung

Figure 1.6: Schematic representation of mouse and human's lung structure.

mice occupies roughly the 18% of the total lung (24% in rats), with an average alveolus mean linear intercept of 80 μm (100 μm for rats) and a blood-gas barrier thickness of 0.32 μm (0.38 μm for rats) [27, 29, 30]. The parenchyma of the human occupies a smaller fraction of the total lung (12%), with larger alveoli mean linear intercept (210 μm) and gas-blood barrier (0.62 μm) [15, 27]. An important functional difference observed between rodents and humans is the paucity of submucosal glands and the presence of a high number of nonciliated cells (Clara cells) in rodents [27].

Even though the significance of all these anatomical features of the mouse lung for lung function is matter of debate, it is generally believed that they might explain the different inflammatory effects of specific allergens on rodents and humans [27].

1.1.2 Lung pathologies

Respiratory diseases comprise a vast number of pathological conditions affecting the pulmonary tract, including conditions of the upper respiratory tract, trachea, bronchi, bronchioles, alveoli, pleura, pleural cavity, and the nerves and muscles of breathing. They range from mild (e.g., common cold) or self-limiting to life-threatening (e.g., bacterial pneumonia, lung cancer, etc.) [1, 31].

While a comprehensive classification of these pathologies can be found in specific reports of the World Health Organization (WHO) [32], for practical

reasons the major part of the most common lung diseases can be categorized as follows [31]:

- *Obstructive diseases* : All these diseases are characterized by airways obstruction, which can originate for different reasons. Firstly, the lumen can be partially or totally obstructed by excessive secretions (e.g. in chronic bronchitis); secondly, the obstruction can take place in the wall of the airway because of an excessive contraction of the bronchial smooth muscle (e.g. in asthma), hypertrophy of mucous glands (e.g. chronic bronchitis) or inflammation and edema of the wall (like both in asthma and chronic bronchitis). Finally, the obstruction can be due to changes that take place in the peribronchial region. This is for example the case of the lung parenchyma destruction typical of emphysema (with its loss of radial traction and consequent narrowing of the airway) or peribronchial edema [31].

  The most frequent pathologies which belong to this category are *asthma* [33] (see Section 1.1.2.1) and the so-called *Chronic Obstructive Pulmonary Diseases (COPDs)* [31], which include *emphysema* (enlargement of the air spaces distal to the terminal bronchioles, with destruction of their walls [9]), *chronic bronchitis* (excessive mucus production in the bronchial tree, sufficient to cause excessive expectoration of sputum) or a mixture of the two [31].

- *Restrictive diseases* : All these diseases are characterized by a restriction of lung expansion, resulting in a decreased lung volume due to alterations of the lung parenchyma or to pathological conditions of the pleura (e.g., pneumothorax), chest wall (e.g., scoliosis) or neuromuscular apparatus (e.g., muscular dystrophies) [31]. The most frequent pathology which belong to this category is the *diffuse interstitial pulmonary fibrosis*, whose main feature is the excessive thickening of the interstitium of the alveolar wall [9].

- *Vascular diseases* : All these diseases are characterized by pathological conditions of the pulmonary vasculature. The most frequent pathologies which belong to this category are the *pulmonary embolism* (blockage of the main artery of the lung or one of its branches by a substance that has travelled from elsewhere in the body through the bloodstream) and the *pulmonary hypertension* (increase of pulmonary blood pressure which may lead to heart failure). The abnormal accumulation of fluids in the extravascular spaces and tissues, known as *pulmonary edema*, belongs

to this category as well, even though it's a complication of a variety of heart and lung diseases rather than a disease on its own [31].

- *Environmental, infectious, suppurative, and diseases* : This category comprises a large range of diseases which do not fit in the previous three classes of pathologies, including many occupational lung diseases caused by inhaled dusts, abnormal functioning of exocrine glands (e.g., *cystic fibrosis*) or viruses and bacteria (e.g., *pneumonia* and *tubercolosis*). In addition, neoplastic diseases of the lung are included in this category (see Section 1.1.2.2).

1.1.2.1 Asthma

Asthma is a complex chronic inflammatory disorder of the airways which involves several inflammatory cells and mediators and which results in pathophysiological changes of the lungs. As the pathogenesis of asthma is not clear, its description is generally based on the functional consequences of airway inflammation, including the airways excessive responsiveness to various stimuli that leads to recurrent episodes of wheezing, breathlessness, chest tightness, and coughing. These episodes are often associated with diffuse airflow obstruction within the lungs. For these reasons, for didactic purposes, asthma is generally categorized as an 'obstructive disease' [31].

The burden of asthma is consistent worldwide, with an estimate of about 300 million individuals affected by this airways disorder and 250 000 annual deaths [34]. The economic impact of asthma is substantial all over the world, both for direct medical costs (cost of medications and hospitalizations) and indirect non-medical costs (asthma is a major cause of absence from work in many countries) [34].

Pathophysiology The three main hallmarks of asthma are *airway inflammation* , *bronchial remodeling* and *airway hyperresponsiveness* [33–37], as schematically shown in Figure 1.7. The relation intercurring among them is not clear; it is supposed that the inflammatory process results in the characteristic pathological changes of the airways in ways that are not well understood. Even though it is still matter of debate, it seems that inflammation and bronchial remodeling may be strongly associated to airways hyperresponsiveness and the other asthma symptoms [34, 38].

- *Airways inflammation* : the presence of inflammation is a constant feature in all asthmatic patients [34]. Typically mucosal mast cells and

macrophages are activated by allergens and release bronchoconstrictor and inflammatory mediators. Increased number of mast cells in airway smooth muscle may be linked to airway hyperresponsiveness while macrophages mediators amplify the inflammatory response [34, 36]. A significant increase in the number of airways eosinophils, neutrophils, and T-lymphocytes is commonly observed. While the pathophysiological role of neutrophils and T-lymphocytes is still unclear, eosinophils are suspected to be at the basis of the damaging process of epithelial cells and airway remodeling [34, 36].

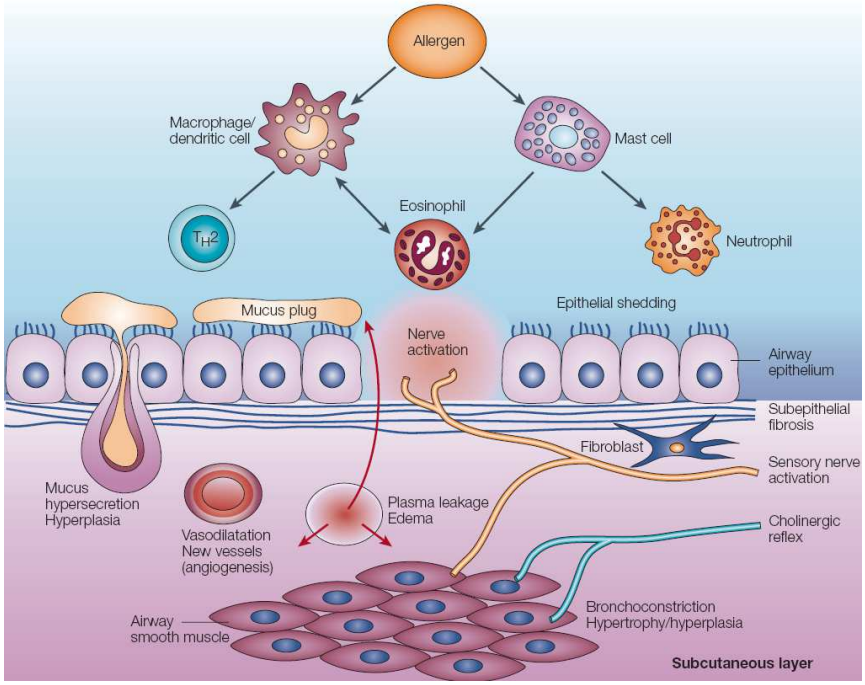

Figure 1.7: Schematic representation of asthma pathophysiology. Several inflammatory cells and mediators are recruited or activated, producing acute effects on the airway (bronchoconstriction, plasma leakage, mucus secretion, sensory nerve activation, ...), together with remodeling structural changes (subepithelial fibrosis, angiogenesis, increased thickness of airway smooth muscle, hyperplasia of mucus-secreting cells, ...). Reprinted from [36].

- *Bronchial remodeling* : with this term it is generally indicated all the characteristic structural changes in the airways of asthma patients, which often result in an irreversible thickening of bronchial walls and, consequently, narrowing of the airways [33, 34, 36, 38]. These changes include subepithelial fibrosis with deposition of collagen fibers (basement membrane thickening), airway smooth muscle hypertrophy (in-

creased size of individual cells) and hyperplasia (increased cell division), blood vessels proliferation (angiogenesis) and increased mucous secretory cells (hypertrophy of mucosal glands, hyperplasia of goblet cells,...) [33–35, 39–42].

- *Airway Hyperresponsiveness* : with this term it is generally indicated the excessive airways narrowing in response to an external stimulus which would be innocuous in a person not affected by asthma. This airway narrowing, as a consequence, leads to airflow limitation. Its mechanism is probably connected to the excessive contraction of airway smooth muscle, thickening of the airway wall, and sensitized sensory nerves [34–36, 43]. It is therefore hypothesized that both inflammation and bronchial remodeling play an important role in the hyperesponsiveness development [34].

Treatments Medications to treat asthma are classified as *controllers* or *relievers* [34]. The formers are medications which are based on a long-term approach and are taken daily to keep asthma under clinical control mainly thanks to their anti-inflammatory effects; they include inhaled and systemic glucocorticosteroids (e.g., budesonide) and long-acting inhaled β_2-agonists [36]. The latters are medications used on a as-needed basis in order to quickly reverse acute asthma symptoms [34], mainly acting on the bronchoconstriction; short-acting β_2-agonists belong to this category [36].

While it has been shown that controller medications can strongly improve patients' quality of life (controlling airways inflammation, decreasing airways hyperresonsiveness and severity of exacerbations), it is widely known that they do not cure asthma and they have to be taken continuously [34]. All these therapies are intended to treat inflammation and bronchoconstriction whereas bronchial remodeling still remains insensitive to current asthma treatments [44]. Whether and when to begin treating patients with asthma to prevent or reverse the negative effects of remodeling, which components of remodeling to target, and how to monitor remodeling are still matters of debate.

1.1.2.2 Lung Cancer

Lung cancer is a disease characterized by uncontrolled cell growth in the lung tissues. Its development is the result of multiple alterations which include the classical genetic abnormalities that cause the overactivity of growth promoting oncogenes and the inactivation of the tumor suppressor gene [45]. The most common cause of lung cancer is long-term exposure to tobacco

smoke, which accounts for 80-90% of all lung cancers [46, 47]. The other cases are generally attributed to a combination of genetic factors and exposure to a number of carcinogenic substances like radon gas, asbestos, some metals compounds (cadmium, chromium, beryllium, nickel, arsenic, ...), ionizing radiations and air pollution (including second-hand smoke) [31, 46, 47].

Lung cancer is the leading cause of cancer deaths worldwide and the third cancer for occurrence in both sexes (after breast and prostate cancers) [48]. The burden of this disease is impressive since it is estimated that lung cancer is responsible for more than 1.3 million deaths per year [46, 48].

Pathophysiology Lung cancers are mainly classified as either Small-Cell Lung Cancers (SCLCs) or Non-Small-Cell Lung Cancers (NSCLCs) [47]. SCLCs account for approximately 15% of all lung cancers, they develop mainly in the main bronchi (bronchial submucosa), and are highly malignant, spreading early in the course of the disease. The name comes from the fact that the oval-shaped cells which compose this type of tumor are smaller than normal cells with scant cytoplasm. Virtually all patients with SCLC have a smoking history [45–47]. On the other hand, NSCLCs account for approximately 85% of all lung cancers and are commonly further divided into three sub-categories: adenocarcinoma, squamous cell carcinoma, and large cell carcinoma [49].

- *Adenocarcinoma* : it is a malignant epithelial tumor with glandular differentiation and mucus production which generally develops peripherally in the lungs. Adenocarcinomas account for approximately 40-45% of lung cancers. The majority of adenocarcinoma cases are associated with smoking; nonetheless, this type of lung cancer is the most common in non-smokers [47, 49].

- *Squamous cell carcinoma* : it is a malignant epithelial tumor showing keratinization and/or intercellular bridges that arises from bronchial epithelium. It generally arises centrally in the main bronchi and it accounts for approximately 30% of lung cancers. Like for SCLCs, over 90% of squamous cell lung carcinomas occur in cigarette smokers [49].

- *Large cell carcinoma* : it is, by definition, a poorly differentiated tumor. It is a diagnosis of exclusion made after ruling out the presence of a component of squamous cell carcinoma, adenocarcinoma or small-cell carcinoma. Large cell carcinoma typically appears as a large, peripheral mass, but may also involve large bronchi. It accounts for approximately 10% of lung cancers [49].

Diagnosis and treatments Prognosis of lung cancer is generally very poor, with an overall five-year survival rate of 15% [46, 47, 50]. The main reason of this is that the disease is often diagnosed at its latest stages [45, 47]. Surgery, when applicable, is the treatment of preference. Radiotherapy and chemotherapy are generally used as adjuvant therapies or as primary/palliative therapies when the tumors are inoperable [46, 47].

The diagnosis mainly relies on chest radiograph whereas Computed Tomography (CT) imaging is generally employed to better understand the type and extent of the disease [47, 50]. The final diagnosis of lung cancer is based on histological examination of the suspected tissues after bronchoscopy in order to avoid the typical false positives of CT imaging [51]. Even though it has been shown that the benefit in monitoring subjects at risk (e.g., smokers) with conventional imaging techniques (e.g., CT) brings great advantages in terms of early diagnosis and hence prognosis [50, 52–54], concerns have been raised about the radiation risk [3, 47]. Preliminary modeling studies suggest that potential risks may largely outweigh benefits in nonsmokers or in young patients [51, 55]. No current guidelines recommend mass screening to diagnose this pathology, not even for at-risk individuals [56, 57].

1.2 MRI of the lung

1.2.1 Main challenges in MR lung imaging

MRI is a versatile imaging tool which has shown to have a huge potential in imaging lung diseases [2, 5]. *Inter alia*, its capability of providing good spatial resolution and high contrast in soft tissues without the employment of ionizing radiation (typical of Positron Emission Tomography (PET) or CT) has proven to be extremely valuable in non-invasive longitudinal studies, especially in young patients [2, 4, 5]. Furthermore, the wealth of information which MRI can provide thanks to the different image contrast mechanisms (e.g., proton density, T_1 or T_2 relaxation times, diffusion,...) has contributed to the interest in this technique. All these properties have allowed to prove that MRI is the most adequate technique for the screening and diagnostics of numerous pathologies in brain, heart or liver. Nevertheless, this consideration cannot yet be applied to the lung, which remains one of the most difficult organs to image with MRI because of its intrinsic properties [5, 7–9]. In particular, the low proton density of the lung, the enormous amount of air-tissue interfaces and the cardio-respiratory motions hamper the quality of standard proton MRI lung images. Motion artifacts typical of standard non-optimized gradient-echo sequences are shown in Figure 1.8a. When optimized conventional sequences are used, the amount of motion artifacts can be strongly reduced [7, 58, 59]. Nonetheless, the low proton density and short T_2^* of lungs generate images where the parenchyma appears extremely dark (Fig. 1.8b). Even though a number of studies is enabled by this optimized lung images (see section 1.2.2.4), especially when edematous or inflammatory signals are present [60–63], the investigation of subtle changes in lung parenchyma are often difficult with this kind of standard sequences.

1.2.1.1 Lung proton density

Human lungs weigh approximately 900-1000 g after death, including blood [9]. Considering that gas volume in lungs at end-expiration (functional residual capacity) is about 2.5 liters and at maximal inspiration (total lung capacity) is about 6 liters, it means that overall lung density varies from 0.3 g/ml to 0.15 g/ml [9]. This overall density actually does not reflect the complex lung structural organization since the density of the lung is not uniform. In the more peripheral (outer and lower) areas the conduit structures decrease in size and undergo a progressive transition from dense nonparenchymal structures (blood vessels, airways, lymph nodes, and thick accumulation of connective tissue) to parenchyma (composed of about 80% air). Therefore, lung densities

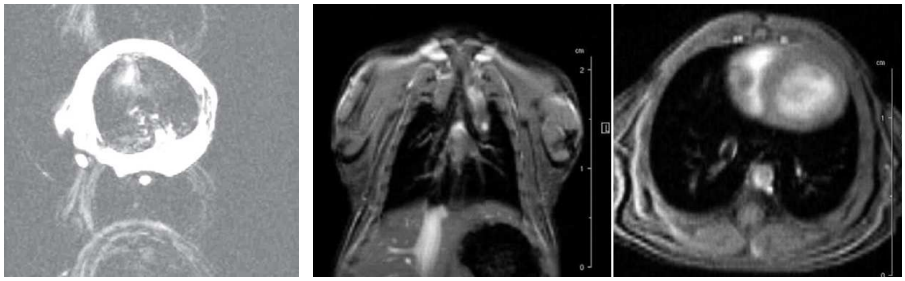

(a) Non-optimized gradient-echo sequence

(b) Optimized gradient-echo sequence

Figure 1.8: Typical gradient-echo images of the lung. (a) When standard non-optimized gradient-echo sequences are used, blurring and ghost motion artifacts can make the image impossible to be exploited. (b) When these sequences are optimized, the amount of motion artifacts can be significantly reduced and images can be used to study a few specific pathologies. Nonetheless, lung images still appear dark and carry very little information about the lung parenchyma signal. Image (a) is adapted from reference [64] (TR/TE=7.8/2.1 ms, FA=15 deg, 40 averages); image (b) is adapted from reference [65] (TR/TE=5.6/3.5 ms, FA=10 deg, 60 averages).

as low as 0.1 g/ml can be observed at the lung periphery [6, 9].

Since the proton MRI signal is directly proportional to the tissue proton density, even under ideal imaging conditions, the NMR signal of the lung is up to ten-times weaker than the one of the surrounding tissues. Furthermore, the change in lung proton density between different phases is an important source of amplitude modulation of the NMR signal during respiration.

The low Signal-to-Noise Ratio (SNR) in lung parenchyma makes the morphological proton MRI of the lung challenging. The SNR can be increased using larger voxel sizes ($SNR \propto voxel\ size$) or the number of averages ($SNR \propto \sqrt{averages}$). Nonetheless, the former choice implies a loss in spatial resolution with the possible consequent impossibility to detect small lesions whereas the latter causes a significant increase in the image acquisition times beyond 10 minutes, which would make the protocol unsuitable for clinical applications [6].

1.2.1.2 Lung air-tissue interfaces

The extensive presence of air-tissue boundaries, due to the huge amount of airways and alveoli, has profound effects on the NMR properties of the lung. Since oxygen in air is paramagnetic and tissue is diamagnetic, a substantial magnetic susceptibility difference ($\Delta\chi \approx 8\ ppm$) is present at air-tissue interfaces, leading to significant static local field gradients. The strongly in-

homogenous local magnetic field gradients at the microscopic scale lead to a rapid dephasing of the proton spins, resulting in typical magnetic resonance (MR) images of the lung which are dark and give poor information about the parenchymal tissue [6, 9].

The dephasing process that takes place because of magnetic field inhomogeneities is typically described by an apparent relaxation time T_2^* according to the monoexponential law [9]:

$$S(t) = S(t=0) \cdot exp\left(-\frac{TE}{T_2^*}\right),$$

where TE indicates the Echo Time of the MRI pulse sequence and:

$$1/T_2^* = 1/T_2 + 1/T_2^{'}.$$

Here T_2 is the transversal (spin-spin) relaxation time and $T_2^{'}$ is a contribution to the signal relaxation time from the local field inhomogeneities.

At 4.7 T, a magnetic field commonly used in small animal scanners, T_2^* in the lung parenchyma of mice has been reported to be between 0.46 *ms* [66] and 1.27 *ms* [67] whereas in humans values ranging from 0.89 to 2.18 *ms* have been measured at 1.5 T [68]. In the light of these considerations, it is clear that proton MRI of the lung becomes even more challenging and requires pulse sequences with very short echo times ($TE < 1-2$ *ms*).

A theoretical model of the static dephasing due to inhomogeneities was proposed by Yablonskiy *et al.* [69], which assumed that magnetized spherical objects (alveoli) are embedded in a given medium and obtained the following analytical formula for the apparent relaxation time of the lung:

$$\frac{1}{T_2^{'}} = \frac{2\pi}{3\sqrt{3}}\eta\gamma\frac{\Delta\chi}{3}B_0,$$

where η is the alveoli volume fraction, γ is the gyromagnetic ratio for proton, and B_0 is the magnetic flux density. This model, which provides theoretical values of lung T_2^* close to the experimental ones, clearly shows the dependence of the apparent transversal relaxation time from B_0. Such inverse proportionality explains why, for proton lung MRI, at high fields the expected SNR gain can often not be realized.

Under this point of view, low field proton MRI ($B_0 = 0.5\ T$) has shown a certain potential in lung imaging. Nonetheless, the long acquisition times required by the low signal-to-noise due to the low field strength make this tool less attractive from a clinical perspective [6].

1.2.1.3 Lung cardiorespiratory motion

Two asynchronous physiological processes contribute to the signal change in MR images of lung parenchyma: heart beats and respiration. The intensity of lung parenchyma NMR signal $i(t)$ can be modeled as [70]:

$$i(t) = i_0 - A_r cos^{(2n)}\left(\frac{\pi t}{\tau_r} - \varphi_r\right) + A_c sin^{(2m)}\left(\frac{\pi t}{\tau_c} - \varphi_c\right), \tag{1.1}$$

where i_0 is a constant value, τ_r and φ_r the period and phase of the respiratory cycle, τ_c and φ_c the period and phase of the cardiac cycle, A_r and A_c the amplitude of both cycles, and n and m parameters influencing the shape of the curve.

Heart and breathing cycles can be a major source of artifacts in lung MRI when these asynchronous movements occur on a time scale which is shorter than the time required to obtain the image [6]. In standard gradient echo sequences, the cardiorespiratory motion can result in a blurring of pulmonary and vascular structures within the lungs as well as ghostlike artifacts along the direction of the phase-encoding gradients (Fig. 1.8a) [9, 71].

The cardiac and respiratory rates for humans are 60-80 beats per minute and 12-20 breaths per minute, respectively; for mice the corresponding values are 480-600 beats per minute and 150-160 breaths per minute [9, 15, 27, 70]. Looking at equation 1.1, it is therefore clear that motion artifacts are even more relevant in small animals, where spatial resolution and image quality can be rapidly degraded.

To reduce cardiac motion artifacts, the electrocardiogram (ECG) synchronization method is the most used and precise technique [71]. ECG is a transthoracic interpretation of the electrical activity of the heart over a period of time, as detected by electrodes attached to the surface of the skin and recorded by a device external to the body. ECG gating allows the signal to be acquired in the same phase of cardiac cycle, resulting on average in reduced cardiac motion artifacts. Nonetheless, the efficacy of this technique is partially limited due to the normal beat-to-beat variability, premature heart contractions, and changes due to respiration or possible patients' arrhythmias [71]. In addition, the limitations of respiratory synchronization methods apply as well to cardiac gating techniques (see next paragraphs).

With respect to respiratory motion, a number of techniques have been proposed to reduce the influence of breathing cycle on lung MR images [71]. For example, in humans breath can be voluntarily held back (*breath-hold*

technique) and a fast pulse sequence acquisition can be performed whilst the breath is held in the acquisition window of approximately 20-30 seconds. The operation can be repeated a certain number of times (4-6) if needed. While the breath-holding can notably reduce the respiratory motion artifacts, a series of drawbacks can be identified. First of all, it is difficult to achieve consistently the same lung volume in a series of images or between subjects. Secondly, this technique requires the full cooperation of the patient, which often becomes complicate in presence of advanced pathologies which impair lung functions (e.g., COPD) [71]. In addition, the breath-hold technique cannot be applied to animal studies.

When working with animals, three main categories of motion-reduction or compensation techniques can be identified: *forced-breathing gating methods*, *non-forced-breathing gating methods* and *free-breathing methods*.

Forced-breathing gating methods This category is based on the use of mechanical ventilators. A breathing valve is generally attached directly to the endotracheal tube and allows for independent control of inspiratory and expiratory phases of ventilation. With the use of a ventilator, the imaging sequence is triggered at a well defined moment of the respiratory cycle, with a consequent improvement in the image spatial resolution. Nonetheless, this technique has several disadvantages since it can interfere with the pathophysiology of the lung and it implies complicate and invasive protocols. In addition, it has been reported that the use of the ventilator can cause lung injuries, pulmonary edema, hypoxemia, and increase the number of neutrophils in the lungs [71–73].

Non-forced-breathing gating methods This category is based on monitoring the displacement of the diaphragm during scanning, with or without the use of an external sensor. In the former case a bellow device is employed whereas in the latter *navigator-echo* or *self-gating techniques* are used. In this case, the acquisition of a partial set of k-space data is processed to track the motion and is usually collected when passing through the origin of k-space. The information about the diaphragm displacement, either obtained using an external bellow device or a navigator-echo, is used to synchronize image data acquisition through *prospective* or *retrospective respiratory gating* [71].

During prospective gating, the respiratory motion is monitored and images are acquired only when the respiratory signal is within a predetermined gating window. In retrospective gating, the signal is collected regardless of the respiration phase; after the signal has been collected, the specified pa-

rameters are used to decide whether a certain signal is accepted or rejected for inclusion in the k-space. While the post-acquisition analysis process may require more sophisticated algorithms, retrospective gating allows to reconstruct images relative to different phases of respiration and does not increase the total acquisition times as in the case of prospective gating. In addition, it has to be noted that the use of all prospective synchronization methods introduces magnetization instabilities due to variable repetition time of the imaging sequence, which may alter the image contrast and influence image quantification [9, 13, 71].

Free-breathing methods This category is based on *signal averaging*. Signal averaging consists in increasing the number of acquisitions to reduce the overall ghost artifacts and improve the SNR of the image, exploiting the inconsistency of the motion artifacts amplitude [9, 71]. A proper trade-off has to be found between the total acquisition time and the number of averages. This technique has proven to be very efficient in several studies of lung diseases, where working in physiological conditions is often required [7, 58, 59].

1.2.2 MR techniques for lung parenchyma imaging

1.2.2.1 The k-space concept

Few time after the development of MRI it was understood that the description of the time-varying signal coming from the precessing magnetization could be easily analyzed by studying two- or three-dimension trajectories in a properly defined space. This space, known as *k-space*, has become the dominating formalism in NMR and will be shortly revised here[1].

In the time domain, the signal created by the transverse magnetization can be written as:

$$S(t) = c \int \rho(\vec{r}) e^{-i\Phi(\vec{r},t)} d\vec{r}, \tag{1.2}$$

where, $\vec{r}$ is the spatial variable, $\rho(\vec{r})$ is the spin density of the excited protons, c is a proportionality constant and the phase Φ is:

$$\Phi(\vec{r},t) = \gamma \int_0^t \vec{r} \cdot \vec{G}(t')\, dt'.$$

[1] For comprehensive description of the MRI theory the reader is referred to references [71, 74].

In this expression, $\vec{G}(t')$ indicates the imaging gradients ($\vec{G}(t') = \vec{\nabla} B_0$) and γ the gyromagnetic ratio ($\gamma/2\pi \approx 42.576\ MHz/T$ for protons). Defining:

$$\vec{k}(t) = \frac{\gamma}{2\pi} \int_0^t \vec{G}(t')\, dt',$$

equation 1.2 can be written as:

$$S(t) = c' \int \rho(\vec{r})\, e^{-i2\pi \vec{k}(t)\cdot\vec{r}} d^3 r. \tag{1.3}$$

The space were $\vec{k}(t)$ resides in is known as *k-space* and corresponds to the spatial frequency domain. The time origin $t = 0$ corresponds to the time at which the transverse magnetization is created by means of a radiofrequency (RF) pulse.

Equation 1.3 shows that the MRI signal $S(t)$ is the Fourier Transform (FT) of the proton density $\rho(\vec{r})$. In other words, the spatial information of the object is encoded as FT and can be selectively sampled by varying the gradients field. The function $\vec{k}(t)$ is the Fourier conjugate variable to the spatial variable $\vec{r}$. As time evolves, $S(t)$ describes a path $\vec{k}(t)$ in the k-space, known as *k-space trajectory*.

1.2.2.2 Cartesian versus non-Cartesian k-space trajectories

The k-space trajectory illustrates the acquisition strategy and influences the type of image artifacts that may occur. Several trajectory schemes have been proposed in order to answer the different problems specific of each organ or to obtain specific contrast mechanisms. An extensive description of common acquisition trajectories is proposed for instance in references [71, 74].

The trajectories acquired in the k-space can be divided essentially in two categories [71]: *Cartesian* and *non-Cartesian*. In the Cartesian encoding scheme, the sampling points are acquired along parallel and equidistant lines, resulting in a uniformly filled k-space, as shown in Figure 1.9a; in the non-Cartesian scheme, the sampling can take place on non-regular or non-uniform paths, as shown in Figure 1.9b.

From equation 1.3, it is clear that the time domain signal corresponds to the FT of the transverse magnetization. Consequently, the MR image reconstruction simply requires a two- or three-dimension inverse-FT of the entirety of k-space. Since the received signal belongs to the complex domain, the image is characterized by complex entries, and usually the magnitude values are presented to the observer.

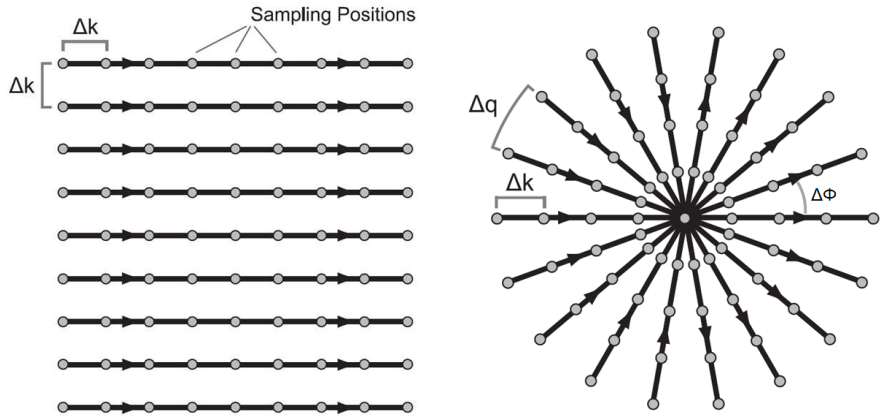

(a) Cartesian trajectory (b) Radial trajectory

Figure 1.9: Schematic representation of typical (a) Cartesian and (b) radial acquisition schemes. Adapted from [75].

When the acquired sample points lie on an equidistant grid, like for Cartesian trajectories, the reconstruction can be performed using an inverse Fast Fourier Transform (FFT). If the k-space is sampled with non-rectilinear or non-uniform trajectories (e.g., spiral or radial acquisitions) the FFT cannot be directly applied and a resampling to a uniform grid is necessary prior to its use [71].

Cartesian k-space trajectories Since the spatial information is encoded through the FT using a discrete sampling rate, specific requirements on the trajectory acquisition follow from the mathematical properties of the Fourier transform. In particular, the discrete sampling operation in the k-space inevitably leads to occurrence of periodic object copies in the image domain, with the distance between the copies equal to the reciprocal of the sampling step Δk in the spatial frequency domain [71, 74, 75]. If Δk is chosen too large, neighboring copies of the object overlap or wrap around in the image space (*aliasing artifacts*), making impossible the proper recovery of the object.

Defining the Field Of View (FOV) as the extent of the object to be imaged, the Nyquist criterion imposes the following condition to be respected in all the encoding directions in order to avoid aliasing artifacts:

$$\Delta k = 1/FOV. \tag{1.4}$$

A way to reduce the sampling step is to change the sampling rate of the receiver. It is therefore useful to define the *receiver bandwidth (BW)* as:

$$BW = 1/\Delta t,$$

where Δt is the sampling time of the receiver. Increasing the BW will therefore result in a decrease in Δk but also in a lower SNR. This is due to the fact that a larger spectrum of Larmor frequencies is used for the spatial encoding, while the noise floor can be assumed to be equally distributed in the frequency space.

The field of view in the generic direction r can be written as $FOV = n\Delta r$, where Δr is the spatial resolution (pixel size) in the selected direction and n the number of samples. From equation 1.4, it follows that the maximum k-space sampling extent is related to image pixel size by:

$$k_{max} = n\Delta k = 1/\Delta r.$$

In Cartesian acquisitions, if the phase-encoding step size is chosen so that it is smaller than in equation 1.4, no aliasing will occurr. In other words, in order to obtain a given resolution Δr without aliasing, n encoding are required, with n equal to:

$$n = 2k_{max}FOV. \tag{1.5}$$

Examples of Cartesian k-space samplings applied to lung imaging are presented in section 1.2.2.4.

Non-Cartesian k-space trajectories Non-Cartesian trajectories can assume various shapes (e.g., spiral, concentric rings, etc.). In the next sections and chapters, only the radial k-space trajectory will be discussed among the 'non-Cartesian acquisitions'. For a more general discussion about non-Cartesian trajectories, the reader is referred to [71, 74].

Projection Reconstruction (PR) (or radial sampling, projection acquisition) was the first MRI k-space trajectory, introduced by Lauterbur in 1973 [76]. It consists in filling the spatial frequency domain space with radial spokes rather than a Cartesian rectilinear raster acquisition. These projections are generally acquired with a constant increment $\Delta\Phi$ in the polar angle (azimuthal angle) Φ. For two dimensional radial acquisitions, the Nyquist criterion ensures aliasing-free images if:

$$k_{max}\Delta\Phi \leq 1/FOV,$$

where the maximum k-space radius k_{max} is related to the desired spatial resolution, as described above. In other words, Nyquist criterion requires the distance between samples on neighboring spokes (Δq in Figure 1.9b) to be

less or equal to the distance Δk between two samples along a spoke in order to ensure an isotropic spatial resolution of $\Delta r = FOV/n$. The number of required radial spokes N_s for a 2π sampling can be therefore written as:

$$N_s = 2\pi/\Delta\Phi = 2\pi k_{max} FOV. \tag{1.6}$$

Comparison of equations 1.5 and 1.6 leads to the relation:

$$N_s = \pi n, \tag{1.7}$$

which suggests the minimum number of spokes required for a radial acquisition over 360° when n samples are acquired. Data collection can be performed with $0 \leq \phi < \pi$ (full echo acquisition) or $0 \leq \phi < 2\pi$ (half-echo or Free Induction Decay (FID) acquisition) [71]. In the first case only one-half number of views are required whereas in the second case radial spokes are always acquired starting from the center of the k-space. Both the type of acquisitions result in an identical spoke distance but differ in the orientation of the spokes, leading to different responses to experimental inaccuracies [71,74,75].

1.2.2.3 UTE radial sequences

Even though radial acquisitions present a certain number of cons (e.g., sensitivity to off-resonance effects, longer acquisition times, etc.), their inherent shorter TE and reduced motion sensitivity compared to Cartesian samplings make them especially suitable for lung parenchyma imaging. Their pros and cons will be shortly discussed hereafter along with their main applications in lung imaging. The description of the pulse sequence scheme and the reconstruction algorithm used in this thesis are presented in section 2.1.

Short TE Because no phase-encoding gradient is used in PR (see section 2.1.1), the minimum TE achievable with radial acquisitions can be very short. This property is particularly interesting when imaging very short T_2^* tissues such as lung parenchyma [10–12]. Various expedients have been developed in order to further reduce the echo time achievable with PR, nurturing the interest in the UTE radial sequences for lung imaging [71,77,78]. Among these expedients, the acquisition of the FID instead of the full echo collection is rather common. The FID is thus recorded right after the slice-selective RF excitation and the slice-refocusing gradient. In this case, the echo time is defined as the interval between the center of the RF excitation pulse and the first point of the recorded FID. In order to minimize the TE, data acquisition is often started from the beginning of gradient ramp using non-linear sampling [71,77]. Echo times shorter than 300 μs can be achieved in two-dimension UTE radial acquisitions (see chapter 3).

Reduced motion sensitivity One of the strong advantages of radial acquisitions is less sensitive to motion artifacts (e.g., respiration, flow, etc.) compared to Cartesian sampling [9, 13, 71, 75, 77]. As shown by Glover and Pauly [12], the radial acquisition motion artifacts consist of streaks propagating from the moving structure. These motion artifacts have low amplitude near the moving object and often reside outside the anatomic boundaries of the subject. Conversely, in Cartesian imaging, the motion artifacts are manifested as blurring and ghosting throughout the entire image, in the phase-encoding direction. In addition, inherent oversampling of the k-space center in radial acquisitions results in signal averaging of low spatial frequencies, which further reduces the motion artifacts (at the expenses of a slightly increased image blurring) [12, 71].

A side advantage of the repeated acquisition of the central point of the k-space is the self-navigating (or auto-navigating) potential of PR. Indeed, the NMR signal amplitude measured at the center of the spatial frequency domain corresponds to the total transverse magnetization from the whole imaged volume (see equation 1.3, with $\vec{k}(t) = 0$). When the FOV contains moving structures, consecutively acquired echoes will thus exhibit peak changes proportional to the changes in the overall transverse magnetization caused by motion. Radial acquisitions allow the detection of these signal changes at each radial projection. As a consequence, the signal amplitude changes measured at the center of k-space can be used to monitor or correct for motion. Such property was shown to be useful in implementing retrospective gating without respiratory monitoring or cardiac ECG, as shown in Figure 1.10 [13, 71].

Drawbacks Radial acquisitions present some drawbacks compared to standard Cartesian sampling schemes. A detailed analysis of some of them can be found in [71, 75, 77, 78].

First of all, PRs are characterized by an increase in scan time compared to Cartesian trajectories if the Nyquist criterion is satisfied. Looking at equation 1.7, Nyquist sampled two-dimension radial acquisitions require at least $\pi/2$ ($\sim 57\%$) more views than a comparable Cartesian sampling scheme, when acquisition is performed over 180° (two times more when performed over 360°). This is due to the fact that radial acquisitions inherently oversample the k-space close to the center, while leaving the periphery undersampled. Likewise, the non-uniform sampling requires the use of regridding algorithms and weighting functions before the application of the inverse FFT (for more details see 2.1.2).

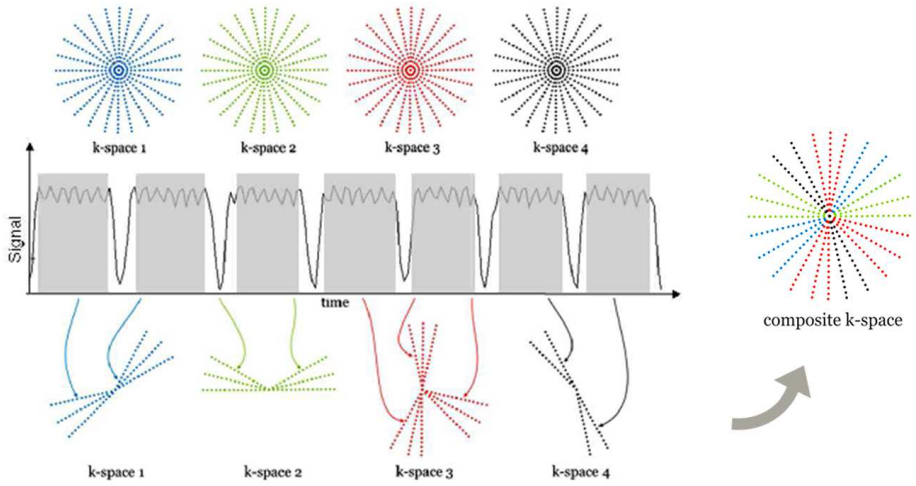

Figure 1.10: Schematic diagram of the retrospective self-navigating reconstruction technique. Only the projections that are acquired during the desired respiratory window (in grey) are used to reconstruct the image from the composite k-space. Adapted from [13].

Secondly, radial sequences are especially sensitive to off-resonance effects and eddy currents, which can result in image blurring [71, 75]. Several non-trivial solutions have been proposed to minimize these problems. Experimentally, the former can be minimized using shorter TEs and wider acquisition bandwidths BWs (taking into account the trade-off between BW and average SNR) whereas the latter can be reduced optimizing the hardware (e.g., working with self-shielded coils) or measuring the real k-space trajectory [71, 75].

Applications to lung imaging The advantages described above clearly make the UTE radial acquisitions especially interesting in lung imaging. In particular, the very short TEs achievable with UTE radial MRI allow the visualization of lung tissue with high SNR (see chapter 3). This advantage over standard Cartesian sequences has been exploited in animal studies in order to detect emphysema and fibrosis microstructural changes of the lung parenchyma [66, 79, 80]. In addition, alterations in ventilation/perfusion ratio in lung injury models have been measured with UTE radial sequences in several studies [14, 81]. Furthermore, the reduced sensitivity of UTE radial sequences to motion artifacts was shown to allow for the accurate detection and quantification of edematous signals and mucus plugging in acute models of inflammation [14, 82]. Finally, UTE radial sequences have been applied on humans to study lung morphology, physiology and pathologies [5, 83, 84].

The advantages, the limitations, some possible new applications, and the potential of this class of sequences will be discussed throughout the whole thesis, as anticipated in the Preface.

1.2.2.4 Other techniques for lung parenchyma imaging

Many techniques have been proposed to study specific questions related to lung morphology, function or pathologies. Exhaustive review articles can be found in literature about the commonly used tools in pre-clinical and clinical lung studies [5–7, 9, 50, 85]. In this section only some of the most common MRI pulse sequences currently used in lung studies will be presented as a possible alternative to UTE MRI.

Spoiled gradient-echo sequences They are a class of sequences that enable the acquisition of a gradient echo after the RF excitation with a flip angle (FA) lower than 90°. The remaining transverse magnetization is destroyed after the data acquisition (*spoiling*). The distance between two different RF excitations is called *repetition time (TR)* while the interval between the RF excitation pulse and the refocusing of the spins (echo) is defined as TE [71]. The Fast Low-Angle Shot (FLASH) sequence (see Figure 1.11a) is a commonly used acquisition scheme belonging to this category of Cartesian acquisitions[2].

In FLASH sequence, a single row of k-space is acquired after one RF excitation, whereas for each TR a different row is acquired (see Figure 1.11b). Echo times in the order of the millisecond can be achieved even though, when imaging lung parenchyma, TE $\leq$ 1 ms have to be used [6]. The sequence can have a strong T_2^* weighting component (for long TEs) even though an additional T_1 or spin density contrast can be achieved, according to the chosen parameters (TE, TR and FA) [6, 71].

This kind of sequence has several applications in lung MRI for anatomical imaging, magnetic resonance angiography or contrast-enhanced studies [5–7, 85]. Beckmann *et al.* [59] have indeed shown that spoiled gradient echo sequences can lead to images with reduced motion artifacts by using averaging approaches. Since then, gradient echo imaging has been applied to detect and quantify mucus secretions, inflammation, vascular remodeling and parenchymal destruction in a number of animal models of lung diseases like COPDs [62, 63, 86, 87], pneumonia [88], or lung fibrosis [89, 90]. In clinical

[2]Other acronyms are used by different vendors to indicate the same pulse sequence scheme. In this work only the acronym FLASH will be used.

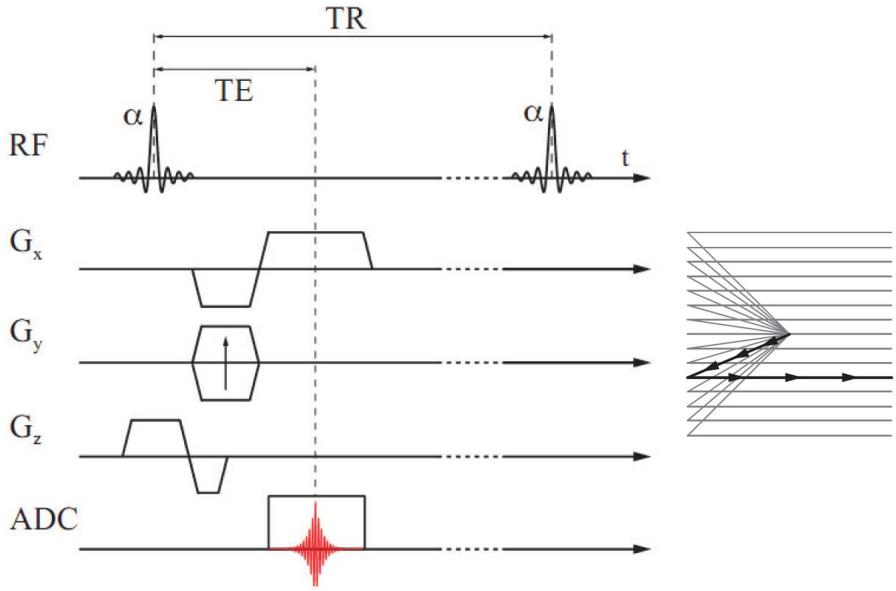

(a) FLASH pulse sequence (b) FLASH k-space

Figure 1.11: Schematic representation of (a) a generic FLASH sequence and (b) its respective sampling k-space trajectory. In the pulse sequence chronogram no gradient spoiler is represented at the end of sequence. Spoiling can indeed be achieved in different ways, including very long TRs, end-of-sequence RF gradient spoiling or (like in this case) RF spoiling by phase cycling the RF excitation pulse. Adapted from [64] and [75].

practice, two and three dimensional gradient echo sequences have shown to be useful in the detection of pulmonary nodules or perfusion disorders [5, 50, 85].

Some applications of this class of sequences, its advantages and its limitations will be sparsely presented in the next chapters, in relation to the lung disease models which will be discussed after on (i.e., asthma and lung cancer).

Balanced steady-state free precession sequences This class of sequences is similar to the previous one, except for the fact that the transverse magnetization is not spoiled at the end of each TR. Indeed, in this type of sequences a steady-state free precession is reached, refocusing the transverse magnetization at the end of each repetition time interval. To do so, within each TR all gradients are balanced (i.e., the gradient dephasing is refocused). For short TR, this kind of sequences are characterized by a contrast T_2/T_1 [6]. Balanced steady-state free precession sequences are extremely sensitive to off-resonance and field inhomogeneities, which causes banding artifacts. A possible solution to this common problem consists in the acquisition of several images in which these bands are spatially shifted by RF phase-cycling, and the subsequent

combination of them into an image with reduced banding artifacts [71].

Their similarity with spoiled gradient-echo sequences allows to reach short TEs and TRs, which makes them interesting tool for rapid lung imaging. Their inherent contrast makes them effective for imaging blood and mucus (long T_2 compared to lung tissue). In clinical practice, balanced steady-state free precession sequences have shown to be effective in the detection of pulmonary embolism and in the study of respiration mechanics [5, 6, 70, 85].

Single-shot fast spin echo sequences It is a subclass of sequences that uses spin echoes instead of gradient echoes (i.e., the echo is collected after an RF excitation pulse with FA = 90° and a refocusing pulse with FA = 180°). In single-shot fast spin echo sequences a train of spin echoes is obtained by repeated refocusing of the first spin-echo. These sequences allow the acquisition of all the lines of the k-space in a single echo train, making them suitable for rapid imaging [5, 6, 85]. This kind of sequences is characterized by a T_2 contrast and is starting to be employed in lung imaging studies [6]. In clinical practice, single-shot fast spin echo sequences have shown to be effective in the detection of lung infiltrates and nodules [5]. These sequences, with or without motion compensation techniques, have shown to be extremely useful when imaging pediatric patients because of the rapid imaging they allow [5].

1.3 MRI contrast agents for lung imaging

As described in section 1.2.1, a number of challenges have to be faced when imaging lung with MRI. Several solutions have been described for minimizing motion artifacts (see 1.2.1.3 and 1.2.2.3). Similarly, the fast dephasing caused by susceptibility gradients can be minimized using short TEs or low magnetic fields, as described in sections 1.2.1.2 and 1.2.2.3. Nonetheless, the weak NMR lung signal, due to the low proton density of this organ, remains a strong limitation [91].

Among the solutions which have been proposed in the last decades, the use of exogenous contrast agents is a very promising one and it is in continuous development. A number of techniques have been advanced to improve lung imaging. The application and advantages of these contrast media go beyond the simple increase in the SNR per unit time. Indeed, it has been shown that these exogenous agents can have multiple diagnostic or therapeutic applications [91]. Hereafter a short overview of the main categories of exogenous contrast agents for lung imaging and their working principles will be presented, with special attention to the class of paramagnetic contrast media which will be extensively used in the next chapters.

1.3.1 MR contrast agents applied to lung imaging

Paramagnetic contrast agents Elements or compounds are called *paramagnetic* if they possess a permanent magnetic moment due to the presence of one or more unpaired electrons. These substances have a small, positive susceptibility to magnetic fields ($\chi > 0$) and in presence of an external magnetic field they show a magnetization which is proportional to the applied magnetic field and inversely proportional to the temperature [92].

Metal ions like gadolinium (Gd^{3+}) or manganese (Mn^{2+}) cations are paramagnetic. In aqueous solutions, their electronic magnetic moment can have a dipolar magnetic interaction with the small magnetic moments of water protons. The fluctuations in the dipolar magnetic interaction, resulting from random molecular motion, reduce both the longitudinal and transverse relaxation times of water proton. These changes in the relaxation properties of water protons can be efficiently used in MRI to alter specific tissues contrast [92, 93]. Due to their toxicity and unfavorable biodistribution, metal ions cannot generally be used in their ionic form. Binding to specific ligands is therefore generally used in order to obtain more desirable biodistributions and safety profiles. The resulting metal-ion complex is called *chelate* [92].The final size of these contrast media, which strongly influence their pharma-

cokinetics and excretion, varies from 1-2 nanometers to several hundreds of nanometers.

This class of contrast agents has been used in lung imaging to study ventilation and perfusion [5, 6, 93–98]. The theory behind the mechanisms responsible for the contrast produced by this type of exogenous contrast media is presented in section 1.3.3.

Superparamagnetic contrast agents Superparamagnetic substances are most typically iron oxide particles which, in presence of an external magnetic field, tend to align with the field, resulting in a large net positive magnetization. This behaviour is similar to paramagnetism but the permanent magnetic moment and susceptibility of superparamagnetic particles are larger compared to the ones of paramagnetic substances. Such a behaviour is produced by the union of several paramagnetic ions along with an effect of *cooperativity*, i.e. the capability of the single spins to align to build up a *superspin* [92].

Superparamagnetic particles are generally made of a core of one or more iron crystals embedded in a coating which prevents agglomeration and tailors their targeting properties. They are conventionally divided in two categories [92]: the ultra-small superparamagnetic iron oxide (USPIO) particles and the superparamagnetic iron oxide (SPIO) particles. The former are characterized by a diameter inferior of 50 nm while the latter include all the superparamagnetic nanoparticles with a diameter larger than 50 nm.

This kind of nanoparticles has shown several applications in multiple organs (especially in the reticuloendothelial system (RES) organs [93, 99]) for MRI diagnostic applications as negative contrasts (see section 1.3.3) [93]. These nanoparticles have also shown a strong capacity to label specific cell, opening the possibility of studying for instance stem cell migration and immune cell trafficking [100]. Furthermore, superparamagnetic nanoparticles have been used as therapeutic agent exploiting the possibility of inducing localized hyperthermia in tumor cells through the use of high-frequency electromagnetic waves [101]. However, only few applications of superparamagnetic particles have concerned MRI lung imaging because of the already weak NMR signal of this organ and its strong susceptibility effects that make their T_2^* effect negligible. Nonetheless, Strobel *et al.* [102] have recently shown that the use of T_1-weighted UTE sequences can minimize the T_2^* relaxation, making the SPIO T_1-effects of detectable and exploitable to identify iron loaded immune cells in inflamed lungs.

Hyperpolarized gases Compared to conventional proton imaging, gas MRI is limited because of the intrinsic low spin density (typically three orders of magnitude lower spin density compared to water). To encompass this limitation, polarization techniques have been developed [103]. These techniques permit to obtain polarization levels above the thermal equilibrium, with values typically superior to the Boltzmann polarization level by 5 orders of magnitude [104]. They have been principally applied in order to obtain hyperpolarized (HP) ^3He or ^{129}Xe. Once polarized, HP gases return to their thermal equilibrium following a decay time constant equal to the longitudinal relaxation time T_1 of the polarized nuclei. Being chemically inert atoms, ^3He and ^{129}Xe present a T_1 long enough to allow biomedical MR applications [91].

HP gases MRI has been successfully applied in animals and humans to study ventilation defects, diffusion and perfusion changes in a number of pathologies like COPDs [105–107] and asthma [108–113]. Nonetheless, the complexity of the protocols, their considerable costs, and the increasing paucity of ^3He are somehow limiting the diffusion of this imaging technique in clinical practice.

Fluorinated gases ^{19}F is an inexpensive natural element with 100% abundance. This nucleus presents a resonance frequency equal to 94% of the proton and spin 1/2. These similarities of ^{19}F with ^1H are of advantage when dealing with MRI since the same or similar RF coils and pulse sequences can be used to perform measurements, without expensive updates of the scanner. Mobile fluorine is present in human and rodents body tissues at very low concentrations (under MRI detectable threshold) whereas higher concentrations of this element are immobilized in solid matrices in teeth or bones, presenting extremely short spin-spin relaxation times. As a result, the endogenous NMR fluorine signal is negligible with standard MRI sequences. On the other hand, the absence of a relevant background is a favorable condition for obtaining high-specificity and contrast-to-noise ratios, if fluorinated compounds can be introduced in living being [91].

The first MRI application of fluorinated gases was proposed in early 80's [114]. However, only with the development of HP gases MRI applications the interest in this technique was rediscovered. Fluorinated gases such as sulfur hexafluoride (SF_6), hexafluoroethane (C_2F_6) or tetrafluoromethane (CF_4) have been administered to the lungs in humans and animals to study several functional pulmonary parameters (e.g., airways ventilation distribution, ventilation/perfusion ratios, airspace size, ...) [115–119]. No significant adverse

effects has been recorded in humans for the fluorinated gases, even at high concentrations (e.g., 80% for SF_6) [91].

These kind of contrast agents present two main advantages compared to HP gases: their low cost (up to two order of magnitude lower for fluorinated gases) and the simpler protocols (no need of polarization apparatus or preparation times). On the other hand, the SNR of fluorinated gases is significantly lower than the HP one and time-consuming signal averaging techniques are often required. In addition, the short relaxation times of these fluorinated gaseous molecules can result in significant signal loss, even at short echo times [91].

Oxygen-enhanced proton MRI The underlying principle of oxygen-enhanced (OE) MRI is related to the fact that molecular oxygen is weakly paramagnetic because of its two unpaired electrons in the outer shell. When the subject inhale room air (21% oxygen) and subsequently 100% oxygen, a change in signal intensity can be observed due to the reduction of T_1 in oxygenated tissues (in a similar way to gadolinium compounds but with a smaller magnitude). Oxygen enhancement is the result of the transfer of oxygen to blood and tissues by direct diffusion of molecular oxygen from the alveoli. This mechanism was firstly exploited by Edelman *et al.* [120] for ventilation imaging in the lungs and it was shown to permit the detection of altered lung oxygen uptake.

Since then, OE proton MRI has been successfully applied to study oxygen defects in a number of pathologies, including asthma [121], COPDs [122] and fibrosis [123]. The good correlation between signal intensity changes and standard pulmonary function tests has increased the interest in this contrast agent technique [91]. However two main limitations have to be pointed out. First of all, the measurements obtained with OE MRI are indirect (the gas in the alveoli is not directly observed as in other ventilation techniques like HP gases MRI [91]). As a consequence, further studies are needed to understand the mechanisms responsible for the observed changes in signal intensity and to which extent possible pathological changes are related to ventilation, to diffusion or to perfusion. Similarly, lung relaxation times measurements are especially delicate and influenced by the pulse sequence choice, which introduces a further element of variability in this technique. Secondly, prolonged hyperoxia has shown to produce adverse effects [124] or discomfort in patients [125], especially in COPD patients [91, 124].

1.3.2 Contrast agent requirements

The approval of contrast agents by regulatory agencies and the subsequent commercialization follow strict rules similar to the ones that are applied to any medical drug. As a consequence, contrast media must comply with a number of requirements that have to be assessed starting from pre-clinical studies [93].

First of all, contrast agents have to show the capability of altering the parameters responsible for the image contrast in order to provide a useful information which could not be obtained otherwise. As mentioned above, in MRI the parameters that can be altered are multiple and include (but are not limited to) the relaxation times of the tissues. In this sense, the contrast agent should be able to be enough specific to reach the desired tissue/organ (i.e., tumor tissues) and remain localized for a reasonable period of time that permits to perform imaging (or treatment, in cause of therapeutic applications). In the light of these considerations, it is clear that the administration route strongly affects the capability of a given contrast medium to reach the desired organ as well as its pharmacokinetics, biodistribution and excretion.

Secondly, the contrast agent must have a favorable pharmacokinetics and elimination. In particular, it has to be cleared from the targeted tissue or organ in a reasonable amount of time after imaging. The contrast medium must also be excreted from the body, through the kidneys or the RES.

Thirdly, the contrast agent must have low toxicity and be stable in vivo. The contrast mechanism should be effective at concentrations as low as possible, in order to minimize any toxicological effect. Acute and subacute effects systemic tolerance, potential mutagenicity, teratogenicity, and carcinogenicity are only some of the toxicological aspects which has to be assessed before any application to human can be envisaged.

Finally, the contrast agent has to be stable *in vitro* for a reasonable period of time in order to allow its storage and commercialization.

Factors affecting clinical safety When chelating species are involved in the final molecule or nanoparticle, the clinical safety of the contrast agent is strongly dependent on the stability of the chelate *in vivo* [92].

In this case, important features determining the safety of a contrast medium include thermodynamics, solubility, selectivity, and kinetics [92, 93]. The chelating species must indeed have a strong affinity for the metal ion, which is reflected by the *thermodynamic binding constant* (or *complexation constant*) of the complex (bigger constants imply higher stabilities). In addition, the agent has to be sufficiently soluble to avoid the precipitation of the

metal ion, which is potentially toxic. Moreover, the chelate must have high selectivity for the specific metal ion of interest (e.g., Gd^{3+}) to minimize the metal exchange with endogenous ions (*transmetallation*) like zinc, copper or calcium. Finally, the compound must have a slow kinetics of dissociation, i.e. the release of the metal ion of interest (e.g., Gd^{3+}) should be minimal in order to facilitate the (almost) complete excretion of the complex.

1.3.3 Paramagnetic contrast agents relaxivity theory

The mechanism that describes the modification of the nuclear relaxation properties of a solvent in presence of a paramagnetic substance is known as Solomon-Bloembergen-Morgan theory, and it will be shortly reviewed here. Such a theory can be applied to all the main paramagnetic contrast agents like Gd^{3+}- or Mn^{2+}-based compounds. Hereafter only the case of Gd^{3+} will be considered. An exhaustive general description can be found in reference [92].

When a Gd^{3+}-complex is introduced in an environment (e.g., lung tissue), the observed enhanced relaxation rate R_i^{obs} is given by:

$$R_i^{obs} = R_i^{dia} + R_i^{para}, \quad i = 1,2 \tag{1.8}$$

In equation 1.8, R_i^{dia} indicates the relaxation rate of the hydrogen nuclei of the specific tissue in the absence of the paramagnetic contrast whereas R_i^{para} is the relaxation enhancement caused by the paramagnetic substance. The latter is linearly proportional to the concentration of the paramagnetic substance $[Gd]$:

$$\frac{1}{T_i^{obs}} = \frac{1}{T_i^{dia}} + r_i \cdot [Gd], \quad i = 1,2 \tag{1.9}$$

In equation 1.9, $[Gd]$ is generally expressed in millimoles per liter $mmol/L$ (mM) whereas r_i is called *relaxivity* and it is commonly expressed in units of $mM^{-1}s^{-1}$. In section 4.2 the term $1/T_i^{dia}$ (with $i = 1,2$) will be referred as $1/T_i(0)$ (with $i = 1,2$), assuming $t = 0$ to be the instant right before the contrast agent administration. From a practical point of view, the relaxivity defines the efficacy of a paramagnetic substance to enhance the relaxation rate of water protons, and thus its efficacy as MRI contrast medium.

Unpaired electrons of the paramagnetic substance cause rapid fluctuation of the local magnetic field. The increase in relaxation rate is originated by the interactions between this field and the water proton nuclear spins, and its origin is commonly divided in two components: the *inner sphere* (IS) and the

outer sphere (OS) interactions.

$$R_i^{para} = R_i^{IS} + R_i^{OS} \quad \text{or} \quad r_i = r_i^{IS} + r_i^{OS}, \quad i = 1, 2 \tag{1.10}$$

Inner sphere relaxation The IS relaxation is the result of the direct interaction between the paramagnetic center and the inner sphere water molecules. These molecules are directly coordinated by the paramagnetic ion. By means of chemical exchange between the coordinated water protons and the bulk water protons, this effect is transmitted to the bulk.

The interested reader is referred to reference [92] for a detailed summary of Solomon-Bloembergen-Morgan equations describing the IS interactions. Basically, these equations show that the relaxation rate enhancement is directly proportional to the number of bound water nuclei per paramagnetic ion (generally only one) and to the water exchange rate in the inner sphere (as long as the residence time of the water molecule is long enough to ensure the coordination by the paramagnetic center). In addition, since the dominating interaction is of the type dipole-dipole (proportional to r^{-6}), the distance between the paramagnetic center and the water molecules is a key point and inversely proportional to the relaxation rate enhancement. Finally, the relaxivity generated by the IS interactions can be enhanced by increasing the rotational correlation time, which increases the electronic-nuclear dipolar interactions. It has indeed been shown that, for small Gd^{3+} chelates, the fast rotation is the limiting factor for proton relaxivity at magnetic fields relevant to MRI [92, 93].

Outer sphere relaxation The OS relaxation is the result of two different mechanisms: (i) the binding of water molecules to the inner sphere water or the contrast agent protective ligand (the so-called 'second sphere interactions') and (ii) the interaction between the randomly translating water protons and the paramagnetic center (the properly said 'outer sphere interactions').

The second sphere term is related to the fact that strong binding of water molecules to the functional groups of the chelating ligand (i.e., COO^- group) can take place (hydrogen bonding interactions). In this case, rotational diffusion theory has to be used to describe the phenomenon, in a way similar to the IS interactions.

The outer sphere term describes the interaction between the bulk water molecules coming in contact with the paramagnetic chelate as a result of translational motion of the complex and the water molecules. These exchangeable water molecules are responsible for the transfer of the effect of the paramag-

netic ion magnetic moment to the surrounding water protons.

For a detailed summary of the equations describing these phenomena, the interested reader is referred to reference [92].

1.3.3.1 General considerations

Contrast agent design Solomon-Bloembergen-Morgan equations well describe the relation between the observed paramagnetic relaxation rate enhancement and the microscopic properties of the contrast. However their complexity and dependence on several parameters (that in addition vary with the temperature and the applied magnetic field) are the major drawbacks of the theory. As a consequence, complicated multi-parameter simulations are required to infer the microscopic properties of the paramagnetic complex, starting from the measured relaxivity.

On the other hand, this theory enables to understand the most relevant features in the design of an effective paramagnetic contrast agent. For instance, Solomon-Bloembergen-Morgan equations clearly show that, in order to obtain a significant enhancement of the relaxation rate, the paramagnetic atom should have a high spin quantum number S [3] and long electronic relaxation time[4].

Among the paramagnetic atoms, Gd^{3+} is often the preferred choice. This atom has seven unpaired electrons ($S = 7/2$) and a significant magnetic moment of 7.9 Bohr magnetons [126], compared for example with the five unpaired electrons of Mn^{2+} or Eu^{3+} ($S = 5/2$). In addition, the electronic relaxation time for Gd^{3+} is much longer ($\approx 10^{-9}s$) than for the other lanthanides such as Dy^{3+}, Eu^{3+} and Ho^{3+} ($\approx 10^{-13}s$). The combination of these two properties has made gadolinium the paramagnetic atom most used for MRI contrast agents development. Lanthanides such as Dy^{3+} and Ho^{3+} have magnetic moments higher than gadolinium (approximately 10.6 Bohr magnetons for both the ions [126, 127]) due to their greater orbital angular momentum contribution. However, because of their relatively short electronic relaxation time, they are rarely used as paramagnetic centres for MRI contrast agents.

[3] Both IS and OS relaxations are proportional to $S(S+1)$ [92].

[4] The relationship between electronic relaxation times and relaxation rate enhancements is nontrivial both for IS and OS interactions. A detailed discussion on the subject can be found in reference [92].

Once the paramagnetic atom has been chosen, the choice of the chelating species is critical since it affects the MRI properties of the contrast agent. Indeed, the ligand influences the rotation and translation of the contrast agent in space, governs the average distance between water molecules and paramagnetic center, and has effects on the water exchange rate in the inner sphere. Ligands have to fulfill the requirements stated in the previous section but should also maximize the relaxation rate enhancement properties of the contrast agent. Up to now, the most effective approach to increase the proton relaxivity of a contrast agent is related to the slowdown of the ligand-metal ion complex. The reader is referred to reference [92] for a description of the existing chelating species and their properties.

T_2^* effect Contrast agents are commonly defined *positive* if they generate an increase of the signal in the images, as compared to the baseline acquisition before the administration. Similarly, they are defined *negative* if a decrease of the signal is observed. These definitions are not intrinsic and depend on extrinsic factors like, among others, the chosen pulse sequence and parameters.

Commonly, paramagnetic contrast agents generate positive enhancements in T_1-weighted images (for low and homogeneous concentrations) whereas superparamagnetic nanoparticles are often responsible for susceptibility effects that lead to a loss of signal in T_2-weighted images (negative contrast). Nonetheless, it has been shown that T_1 changes can be detected as an increased signal when superparamagnetic nanoparticles accumulate in the mouse lung, if a T_1-weighted UTE sequence is used (i.e., a positive contrast obtained with iron oxide nanoparticles) [102]. Similarly, paramagnetic contrast agents can be responsible for a loss of signal when high-concentrations are used (see section 4.1).

As shown in equations 1.8-1.10, a generic paramagnetic contrast agent affects both the longitudinal and transverse relaxation rates. However, this class of contrast media is commonly used to see positive enhancements in T_1-weighted images. This is due to the fact that the longitudinal relaxation time T_1 is always longer than T_2. As a consequence, being the relaxivity values very close (generally $r_1 \approx r_2$), the change in the signal (and therefore in the contrast) is more important in T_1-weighted images rather than in T_2-weighted ones.

On the other hand, the shortening of T_2 generated by a paramagnetic contrast (due to the effect of r_2) can limit the signal enhancement originated by r_1 in T_1-weighted images. In addition, if the contrast agent concentration is

too high[5], a significant T_2^*-shortening effect can be observed along with the T_2-shortening [92]. Such a phenomenon is due to the strong difference between the magnetic susceptibilities of the highly concentrated paramagnetic ions and the tissue (generally diamagnetic). The resulting strong field inhomogeneities generate a significant loss of signal (see section 4.1).

[5] A similar effect may be observed if the contrast agent is distributed inhomogenously in the tissue producing voxels that contain a high concentration of paramagnetic atoms

2

Material and methods

This chapter will provide a description of two tools which will be extensively used in the next studies: the UTE pulse sequence reconstruction program and the USRPs. These instruments will be partially described in the articles presented in the following chapters. Nonetheless, this section will provide the reader with a precise summary of the technical details relative to the aforementioned tools. An exhaustive description of the 'material and methods' section, in the strict sense of the expression, will be provided for each study which composes this thesis work. Likewise, the reasons why these tools have been chosen will be discussed in the subsequent chapters.

2.1 UTE sequence and image reconstruction

As mentioned in section 1.2.2.2, UTE radial sequences acquire radial spokes in the k-space, subsequently incrementing the polar angle of a constant amount $\Delta\Phi$. Filtered backprojection or regridding algorithms can be used to reconstruct the image [71].

This kind of acquisition scheme was the first one employed by Lauterbur [76, 128] but was largely replaced by Cartesian trajectories soon after to minimize the artifacts caused by static field inhomogeneities and gradients non-linearities. Over the last decades, improvements in the static field homogeneity and gradients linearity, along with a renovated interest in the advantages of PR acquisitions (see section 1.2.2.2), have led to a renewed interest in this kind of sequence [71].

2.1.1 UTE sequence acquisition scheme

In Figure 2.1, the pulse sequence of the UTE radial acquisition used in the subsequent studies is shown. An FID acquisition mode has been preferred to a full echo acquisition to ensure minimal echo times [1]. The radial spokes are

[1] The scheme for a full-echo acquisition can be found in reference [129]

thus acquired in the k-space always starting from the centre over an angle Φ that varies between 0 and 2π.

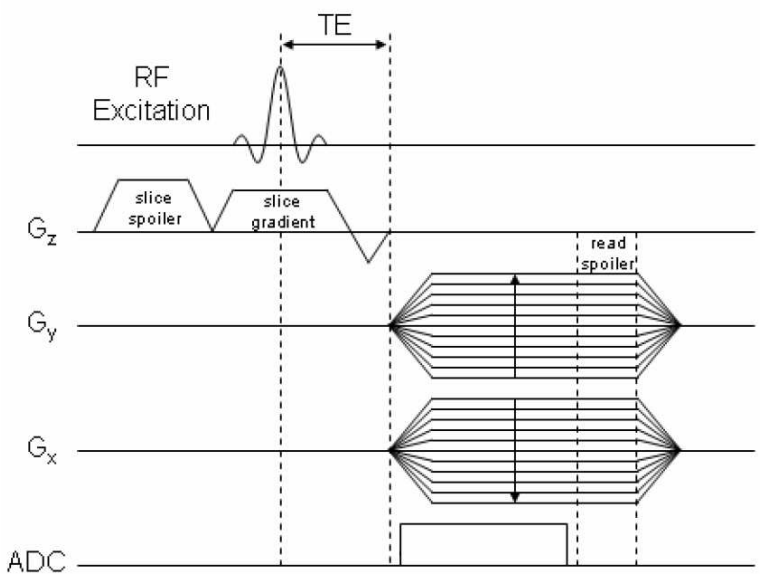

Figure 2.1: Pulse sequence for a radial UTE trajectory with FID acquisition. Adapted from [129].

The pulse sequence consists of a conventional slice excitation (with a chosen FA which can be varied to accentuate a specific image contrast), followed by a fast refocusing gradient (used to refocus slice dispersion). The two gradients G_x and G_y in the physical XY plane are turned on simultaneously with amplitudes:

$$G_X = G_0 \cdot cos\Phi \quad \text{and} \quad G_Y = G_0 \cdot sin\Phi,$$

where G_0 is the maximum readout waveform amplitude. The signal induced by transverse magnetization is sampled by the analog to digital converter (ADC) at constant time intervals, resulting in a set of data points along each projection. The sampling is started right after the refocusing gradient or after a short delay (gradient delay). Each radial projection is acquired after each RF excitation pulse every TR.

Even though a half-pulse RF excitation can be employed in UTE radial acquisitions to further reduce the minimum TE achievable, the conventional excitation scheme was chosen and has been used throughout all the experiments described in the next chapters. The rationale behind this choice is connected to the shorter total acquisition times (two-fold longer for the half-pulse acquisitions) and to the lower sensitivity to gradient imperfections [71].

2.1.2 UTE sequence reconstruction

Once the k-space has been acquired using the aforementioned UTE radial sequence, specific algorithms are needed to reconstruct the image. Two techniques can be employed: the filtered backprojection [128] and the regridding [130]. Both the methods have been shown to work well to reconstruct PR data and to produce equivalent images if the convolution kernel (regridding) and the backprojection filter are properly chosen [71]. Nonetheless, regridding is generally the technique of choice since it is faster than backprojection (regridding can be an order of magnitude faster than backprojection), it can be easily applied to three dimensional acquisitions, extended to reconstruct any non-Cartesian trajectory and it fits onto irregular sampling acquisitions [71].

The reconstruction program developed in IDL (RSI, Boulder, CO) that has been used to reconstruct the UTE radial images presented in this thesis[2] employs the regridding algorithm.

2.1.2.1 Regridding algorithm

As mentioned in section 1.2.2.2, when the k-space is sampled following a non-uniform grid, the inverse FFT cannot be directly applied to the data. Even though a non-uniform discrete Fourier transform could be used on non-Cartesian sampled data, such an algorithm requires a considerably longer computation time [131]. The reconstruction procedure thus generally passes through the *regridding* (or *gridding*) procedure, i.e. the application of an interpolation procedure that allows to resample the data on a uniform grid (Fig. 2.2). As a consequence, the reconstruction procedure for radial trajectories follows four main subsequent steps: density compensation, convolution with a gridding kernel, inverse FFT and deapodization.

Density compensation The density of the non-Cartesian sampled data is not constant in the k-space, leading to overrepresented spatial frequencies [132]. For instance, for radial trajectories, the low frequencies close to the center of the k-space are clearly oversampled compared to high frequencies (Fig. 2.2). Different solutions of density compensation have been proposed to solve this problem that can lead to artifacts if not corrected for.

One commonly used method estimates the density compensation function (or *weighting function*) by computing a Voronoi diagram of the trajectory, where the size of the individual Voronoi cells is inversely proportional to the

[2] Even when a standard reconstruction with the Bruker software ParaVision 5.1 was performed, the regridding algorithm was preferred to the backprojection reconstruction.

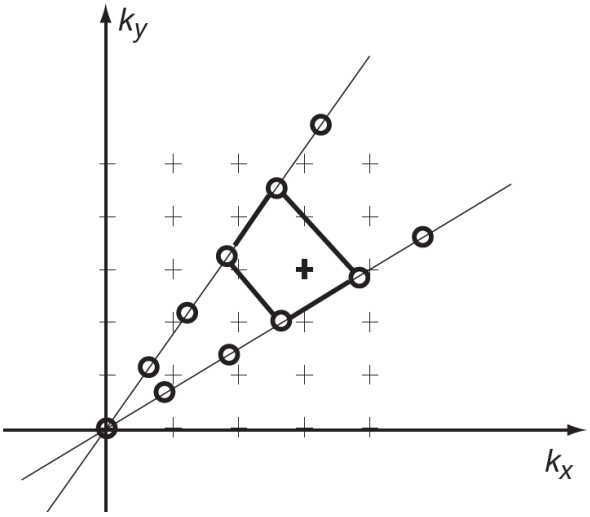

Figure 2.2: Schematic drawing showing the basic problem of regridding for two radial spokes. The aim of regridding techniques is to determine the value of the Cartesian samples from the adjacent samples obtained with the radial acquisition. Reprinted from [132].

local sample density [133, 134]. However, for radial trajectories an analytical density compensation function can be derived, which leads to the ramp-like filter known as Ram-Lak filter [135, 136]:

$$F(\vec{k}) = \begin{cases} |\vec{k}|/N_s & \text{if } |k| \neq 0 \\ 1/(2 \cdot N_s) & \text{if } |k| = 0, \end{cases}$$

with N_s indicating the number of acquired spokes.

Convolution with a gridding kernel and inverse FFT Once the weighting function has been applied, the interpolation of sampled data is performed by convolving the measured k-space points with a radial interpolation kernel, as schematically shown in Figure 2.3a. To avoid distortion of the signal (*apodization*), the interpolations in the frequency space should be performed using a convolution with a *sinc* function (corresponding to a multiplication of the signal by a *rect* function). However, this ideal kernel is infinite in extent and in practice cannot be applied. Among the kernels that best approximate the *sinc* function properties, a radial Kaiser-Bessel function was shown to be a good choice in term of interpolation quality and computational time [137]. This kernel can be written as:

$$K_{KB}(k) = \begin{cases} \frac{1}{L} I_0\left(\beta\sqrt{1-(2k/L)^2}\right) & \text{if } |k| \leq L/2 \\ 0 & \text{elsewhere,} \end{cases}$$

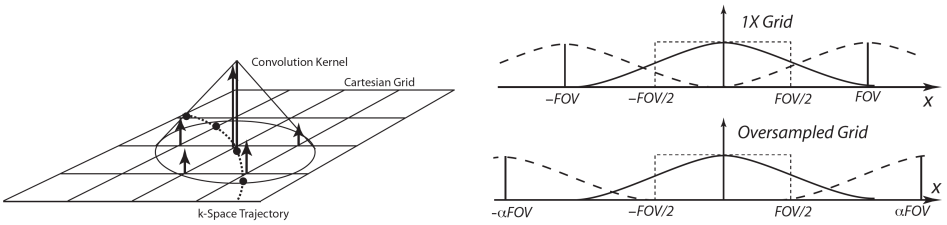

(a) Gridding kernel convolution (b) Oversampling correction

Figure 2.3: Schematic representation of (a) the gridding kernel convolution procedure and (b) the use of oversampling in order to correct for aliasing artifact generated by the finite gridding kernel. Adapted from [132].

where L is the kernel width, $I_0(k)$ indicates the zero-order modified Bessel function, and β is a shape factor. Optimized values of β for a chosen value of L can be computed according to the equations reported in references [134, 138].

Because the exact position of the samples is lost after the interpolation onto the grid, the density compensation function has to be applied as an initial step, before the gridding kernel convolution [132]. Once the density compensation function has been applied and the convolution with the gridding kernel has been performed, an inverse FFT can be applied to the resampled data to obtain the image like for Cartesian acquisitions.

Deapodization and oversampling Convolving the k-space with a kernel function has necessarily side effects on the image. First of all, the apodization has to be corrected for in order to avoid shading in the image (*deapodization*). To do so, the image has to be divided by the apodization function, i.e. by the FT of the gridding kernel [130, 137]. This transform can be computed numerically or, like for radial acquisitions, an analytical expression can be derived. The Fourier transform of the Kaiser-Bessel function can be written as [130]:

$$FT\,(K_{KB})\,(x) = \frac{sin\sqrt{(\pi Lx)^2 - \beta^2}}{\sqrt{(\pi Lx)^2 - \beta^2}} \tag{2.1}$$

Thus, the image (rows and columns) has to be divided by the expression above to obtain a deapodized image.

A second side effect is produced because of the finite kernel used for the interpolation. This operation causes side lobes in the frequency domain and, because of the properties of the FT (see section 1.2.2.2), the side lobes are aliased back into the image plane as neighboring object copies [132]. As shown in Figure 2.3b, a possible solution consists in oversampling the

gridding matrix of a factor α ($1 < \alpha \leq 2$). This permits to increase the distance between the copies, shifting the aliased side lobes away from the object. The extended FOV can be cropped at the end of the reconstruction procedure so that the aliasing artifacts are cut out from the image plane [130, 132].

2.2 Ultra-small rigid platforms

Each imaging modality has advantages and limitations. For instance, MRI can provide good spatial resolution and soft tissue contrast without using ionizing radiation. In addition, it can provide multiple information (relaxation times, proton density, diffusion, ...), according to the aim of the study. On the other hand, compared to CT, its spatial resolution is still inferior; compared to PET or optical imaging techniques, its sensitivity is much lower [4, 139, 140].

As a consequence, multimodality can be a strong figure of merit when developing contrast agents for any application since the advantages of different imaging techniques can be gathered together. Furthermore, as mentioned in section 1.3.2, the contrast agent should have a favourable pharmacokinetics and being excreted from the body in a reasonable amount of time. In this sense, ensuring an exclusively renal filtration and excretion is an effective way to increase the probability of having a fast elimination and a low toxicity [141].

Combining multimodality and negligible hepatic clearance is rather difficult. The former often implies coatings that are too prohibitive in size (for instance, this is the case of quantum dots [142] or gold clusters [143]) whereas the latter is ensured only when the total size of the contrast agent is < 5.5 nm [144].

In this context, silica- or polymeric-based nanostructures are among the most promising strategies. The contrast agents described in this section are called 'Ultra-Small Rigid Platforms' (USRPs) or AGuIX[3] and have been developed by the 'Institut Lumière Matière' of the University of Lyon in collaboration with the start-up Nano-H. These nanoparticles will be used in the research works presented in chapters 4 and 5, and their interest for lung proton MRI will be discussed througout the whole thesis. A further summary of their potential applications to lung imaging and lung pathologies treatment is provided in the patent publication described in appendix A.

The nanoparticles were freeze-dried for storage (using a lyophilizer) as described in appendix D, and sent to the University of Bordeaux for the *in*

[3] In the body of this thesis only the term USRP will be used. The commercial name, AGuIX, will be used only in the manuscripts presented in the appendices.

vivo tests described in the next chapters. The freeze-dried nanoparticles, stable for months without alterations, were dissolved in a NaCl solution (0.9%) to reach the desired concentrations before animal handlings.

The following paragraphs describe the basic synthesis process of these nanoparticles and the properties of the USRPs that were known before the beginning of this work. A detailed description of the synthesis and properties of these nanoparticles can be found in references [145–147]. The description of the chemical details of the synthesis of these nanoparticles goes beyond the aims of this thesis. Such an information can be found in appendices A and D or in reference [145].

2.2.1 Synthesis

The USRPs are obtained using a top-down method proposed in reference [145], consisting in the fragmentation of small nanoparticles (size < 10 nm) that already present the desired functions, except for the sub-5 nm hydrodynamic diameter (HD) [148]. The synthesis process consists of four steps. First of all,

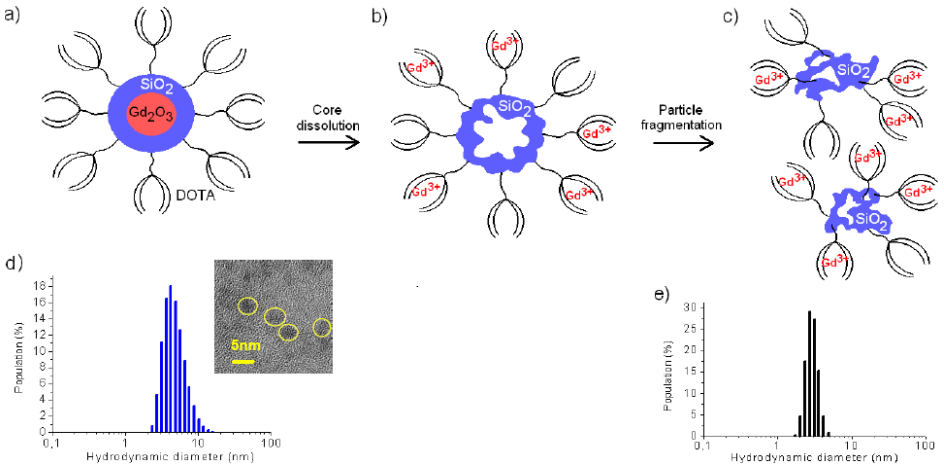

Figure 2.4: (a) Starting small nanoparticle before the top-down method, with Gd_2O_3 core and SiO_2 shell; (b) dissolution in water of the core and chelation of the resulting free Gd^{3+} by DOTA (1,4,7,10-tetraazacyclododecane-1,4,7,10-tetraacetic acid) ligands grafted on the surface of the particle; (c) collapse and fragmentation of the shell into ultra-small rigid platforms (USRPs); (d) size measurement of the particles before the fragmentation process and transmission electron microscopy image of starting core-shell nanoparticles; (e) size measurement of the USRP HDs. Reprinted from [145].

the core of gadolinium oxide (Gd_2O_3) is formed; secondly, the growth of a polysiloxane shell is obtained around the core. Thirdly, the chelating species are grafted on the free amino functions of the inorganic matrix. Finally, the

nanoparticles are purified and transferred to water. During the purification in water, the top-down process occurs, with the dissolution of the core, the trapping of the gadolinium cations by the chelates and the formation of a hollow polysiloxane sphere. This latter collapses and fragments forming the so-called USRPs, made of a polysiloxane network and surrounded by gadolinium chelates covalently grafted to the nanoparticles. During this process, the nanoparticles pass from the original HD of 5.7 ± 1.0 nm to a smaller one, entirely under 5.5 nm (4.1 ± 1.0 nm). The top-down process is schematically shown in Figure 2.4.

Among the paramagnetic atoms, gadolinium was chosen by the inventors because of its slowly relaxing electrons and highest spin quantum number, key factors that determine the ion high relaxation rate (see section 1.3.3) [92, 93]. DOTA was chosen as chelating species because of its higher complexation constant (e.g., compared to acyclic chelating species), its lower kinetics that limits transmetallation with endogen cations such as Ca^{2+} and its reduced toxicity for patients with severe renal dysfunction (see section 1.3.2) [145].

2.2.2 Properties

The obtained USRPs have a total mass of about 10 kDa and are described by the average chemical formula $Gd_{10}Si_{40}C_{200}N_{50}O_{150}H_x$. They are schematically represented in Figure 2.5a. The particles have rather a neutral charge at physiological pH (zeta potential of -0.2 mV at pH = 7.4) and their complexation constant was shown to be very close to the one of the commercial agent Dotarem (24.78 and 25.58, respectively) determined in the same conditions. On average each nanoparticle presents on its surface ten DOTA ligands which chelate core gadolinium ions. Measurements showed that generally between 30 and 40% of these DOTA ligands are free and can be used for scintigraphic applications (e.g., immobilizing radioactive isotopes onto the USRPs). However, when purely MRI applications are envisaged, supplementary paramagnetic atoms can be provided (e.g., by adding a solution containing $GdCl_3$) to increase the total relaxivity of the nanoassemblies. In this case, less than 5% of the DOTA ligands are left free.

The longitudinal relaxivities r_1 *per atom of gadolinium* were measured at 310 K for different magnetic fields after dispersing the USRPs in aqueous solutions of NaCl (0.9%). The nuclear magnetic resonance dispersion (NMRD) profile of the USRPs is shown in Figure 2.5b for proton Larmor frequencies ranging between 0.1 and 60 MHz and it is compared to a NMRD profile of a standard commercially available DOTA(Gd) contrast agent. For instance, the r_1 of the USRPs at 1.4 T was found to be 11.4 $s^{-1}mM^{-1}$ per atom of

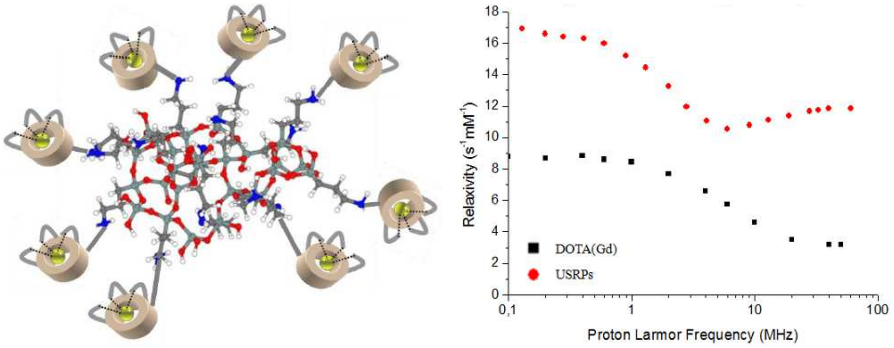

(a) USRP scheme (b) Relaxivity of USRPs

Figure 2.5: (a) Schematic representation of a typical USRP with a polysiloxane bone and DOTA(Gd) species grafted through amide functions (Si grey, O red, N blue, Gd yellow, H white). (b) Proton nuclear magnetic resonance dispersion profiles for the USRPs in aqueous solutions of NaCl (0.9%) and for a standard commercially available DOTA(Gd) contrast agent. The relaxivity is expressed in $s^{-1}mM^{-1}$ per atom of gadolinium. Adapted from [145] and appendix C.

gadolinium (i.e., 114 $s^{-1}mM^{-1}$ per nanoparticle) whereas at 7 T was found to be 6.0 $s^{-1}mM^{-1}$ per atom of gadolinium. The longitudinal relaxivity for the commercially available DOTA(Gd) contrast medium was found to be 3.8 $s^{-1}mM^{-1}$ at 1.4 T and 3.0 $s^{-1}mM^{-1}$ at 7 T. The two- to three-fold higher relaxivity per gadolinium atom of the USRPs compared to standard DOTA(Gd) is related to greater inertia of the rigid structure supporting the gadolinium ions. These structures have indeed shown to be able to slow down the rotation rate of the relaxing species, increasing the relaxivity of the nanoparticles even at higher frequencies (see section 1.3.3) [92, 145]. Finally, the ratio between the transverse and the longitudinal relaxivity of the USRPs was found to be 1.31 at 1.4 T.

When needed to perform Fluorescence Imaging (FRI), cyanine 5.5 (Cy 5.5) near-infrared dye can be covalently grafted onto the nanoparticles (USRPs-Cy 5.5). For the fluorescence nanoparticles USRPs-Cy 5.5 used in the works described in the next chapters, on average, one Cy 5.5 molecule was grafted for every 550 atoms of gadolinium.

Even though only MRI and FRI imaging techniques were used throughout the investigations of this thesis, the USRPs have shown to be easily modifiable in order to perform Single-Photon Emission Computed Tomography (SPECT) imaging (e.g., by adding a solution containing $^{111}InCl_3$ with a high radiochemical purity). Further functionalizations of these nanoassemblies are possible

in order to perform PET imaging[4]. Similarly, specific peptides or therapeutic drugs can be grafted on the nanocarriers to add active targeting or therapeutic properties to the basic USRPs (see chapter 6 for further details).

When administered intravenously in healthy mice, the USRPs showed no undesirable accumulation in lung and liver whereas a fast renal filtration was observed. The results were confirmed by FRI, MRI and SPECT, as shown in Figure 2.6.

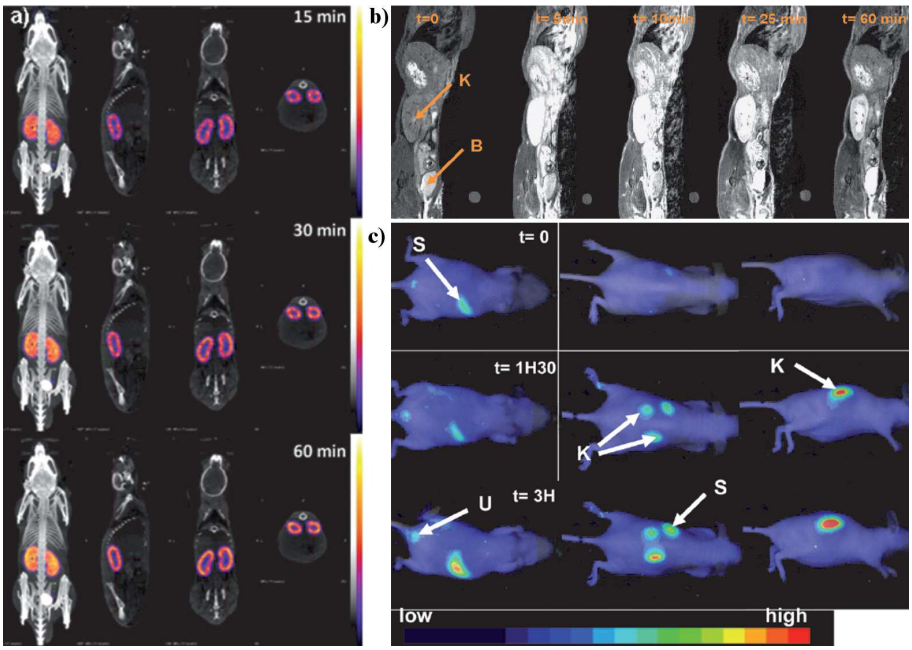

Figure 2.6: (a) SPECT, (b) MRI and (c) FRI biodistribution study after intravenous administration in healthy mice at different times (K = kidneys, S = stomach, U = urine, B = bladder). Adapted from [145].

In particular, SPECT imaging showed a strong accumulation of the USRPs in the kidneys and bladder 3 hours after intravenous administration (approximately 29.8% of injected dose (ID) and 57.9% of ID, respectively). For the other analyzed tissues, the uptake was lower than 0.2% ID, with no hepatic clearance observed, as shown in Figure 2.7. The half-life of the particles in blood was shown to be equal to 9.1 minutes, compared to the 4.7 minutes of Dotarem. Contrarily to Gd-chelates, USRPs were still found in the kidneys 24 hours after administration, supporting the hypothesis that they are cleared

[4]PET imaging using functionalized USRPs with ^{68}Ga and ^{64}Cu has recently been performed (data not yet published).

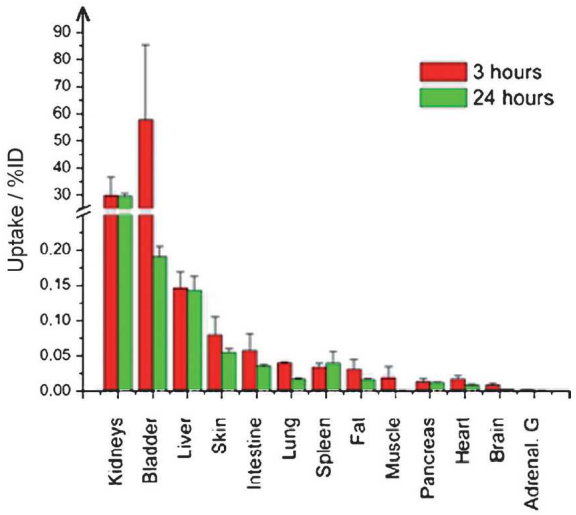

Figure 2.7: SPECT biodistribution of ^{111}In-USRPs 3 and 24 hours after intravenous administration. Reprinted from [145].

from the kidneys according to a multi-exponential law (with a slow clearing component for larger particles and a fast one for the smaller ones) [145].

Finally, the USRPs have shown a capability to passively accumulate *in vivo* in different type of tumors after intravenous administration. In particular, a significant accumulation of these nanoparticles was observed in rats bearing gliomas or hepatic colorectal cancer metastases. The interested reader is referred to appendix C for more details.

The accumulation of the nanoparticles in the tumors is commonly attributed to the so-called Enhanced Permeability and Retention (EPR) effect [149, 150]. This phenomenon tends to explain the superior accumulation of certain nanocarriers in tumors rather than in healthy tissues because of two concurrent factors: (a) the increase in the extravasation from leaky vessels close to the tumor[5] (enhanced permeability) and (b) the lack of effective lymphatic drainage in tumors (enhanced retention).

No application of the USRPs to lung MR imaging and pulmonary pathologies detection had been proposed before this thesis.

[5]This phenomenon is connected to the formation of new vessels close to the tumor (*angiogenesis*), which generally are abnormal in architecture and form. These new vessels are responsible to supply the tumor with oxygen and nutriment.

3

UTE MRI applications on lung diseases

In this chapter, two different applications of radial UTE proton MRI will be proposed to investigate specific lung pathologies, namely asthma and lung cancer. In particular, it will be shown that UTE sequences can be effective tools in the longitudinal noninvasive monitoring of lung diseases and can encompass the limitations of standard gradient-echo sequences. The possibility of using ultrashort-TE radial acquisitions in the drug-discovery process of asthma will be presented. One of the main limitations of MRI compared to other imaging techniques, i.e. its low sensitivity, will be pointed out and discussed in the contest of lung cancer detection.

3.1 A chronic model of asthma in mice

As described in section 1.1.2.1, asthma is a frequent and complex chronic disease, characterized by bronchial inflammation, airway hyperesponsiveness and bronchial remodeling. A number of mechanisms about asthma physiopathology are still unclear and require in-depth studies. In addition, current therapies for this disease mainly rely on inflammation and bronchoconstriction treatment, without an effective action on bronchial remodeling features.

In this context, it is clear that animal studies on realistic murine asthma models assume a central role in the investigation of pathologic mechanisms underlying this disease and in the process of new drug discovery and test. Pre-clinical studies are indeed fundamental in order to provide evidence of a drug efficacy and its potential non-toxicity, key points before any translational application.

Imaging techniques like micro-CT have already provided important information on the pathophysiology of asthma. Its noninvasiveness, compared to terminal procedures (e.g., histology), allows the longitudinal assessment of structural and physiological changes with high resolution, limiting the total number of animals required in the studies and simplifying the protocols. Nonetheless, as pointed out in section 1.2.1, MRI has several advantages over CT, including the absence of ionizing radiation and the good soft tissue con-

trast. While hyperpolarized gases MRI has proven to be a valuable instrument in studying asthma regional ventilation obstructions, its increasingly high costs and complex protocols/instrumentation have limited its application in clinical settings.

In accordance with this thesis aims, a study finalized at demonstrating the potential application of high-resolution proton MRI for the longitudinal and noninvasive assessment of peribronchial inflammation and bronchial remodeling was proposed. In this investigation, UTE MRI was preferred to standard gradient-echo sequences since the investigation required at the same time *either* high spatial resolution for the visualization of the bronchi *and* good signal to noise ratio in the lung parenchyma in order to identify the changes induced by asthma at bronchial level.

The work reported in this section confirmed the results presented in a number of papers according to which UTE MRI is an effective tool for monitoring lung inflammation. In addition, for the first time, it was shown that UTE MRI can be a reliable tool to monitor noninvasively the evolution of bronchial remodeling and may be used in a therapeutic drug delivery preclinical study.

The work presented hereafter has been published on *NMR in Biomedicine*, 26: 1451-1459 (2013), and its copyright belongs to John Wiley & Sons, Ltd.

Ultrashort-TE MRI longitudinal study and characterization of a chronic model of asthma in mice: inflammation and bronchial remodeling assessment.

A. Bianchi, A. Ozier, G. Raffard, O. Ousova, Y. Crémillieux.

Abstract:

Asthma is a chronic disease characterized by bronchial hyperresponsiveness (BHR), bronchial inflammation and remodeling. The great improvements in ^{1}H MRI ultrashort-TE (UTE) sequences in the last decade have allowed lung images with high-resolution and good signal-to-noise ratio to be obtained in parenchymal tissues. In this article, we present a UTE ^{1}H MRI high-resolution study of a chronic model of asthma in mice with the aim to longitudinally assess the main features of asthma using a fully noninvasive approach. Balb/c mice ($n = 6$) were sensitized with ovalbumin over a period of 75 days. The control group ($n = 3$) received normal saline on the same days. MRI acquisitions were performed on days 0, 38 and 78 to study the inflammatory volumes and bronchial remodeling (peribronchial signal intensity index, PBSI). Plethysmographic studies were performed on days 0, 39 and 79 to assess BHR to methacholine using the enhanced pause (Penh) ratio. The average inflammatory volume measured by MRI in the ovalbumin group (15.6 ± 2.4 μL) was increased significantly relative to control mice (-0.3 ± 0.7 μL) on day 38. The inflammatory volume was larger (34.2 ± 3.1 μL) on day 78 in the ovalbumin group. PBSI was significantly higher in the ovalbumin group on day 78 (1.53 ± 0.08) relative to the control group (1.16 ± 0.10), but not on day 38. After sensitization, asthmatic mice presented BHR to methacholine on days 39 and 79. Penh ratios correlated significantly with the inflammatory volume on day 39 and with the PBSI on day 79. This study shows, for the first time, that high-resolution UTE ^{1}H MRI of the lungs may allow the noninvasive quantification of peribronchial eosinophilic inflammation with airways occlusion by mucus and of bronchial remodeling in a murine asthma model that correlates with functional parameters.

Keywords:

Lung ^{1}H MRI; UTE; asthma; bronchial remodeling; inflammation

3.2 An orthotopic model of lung cancer in mice

As described in section 1.1.2.2, lung cancer is one of the most frequent and lethal cancers. One of the main reasons for lung cancer poor prognosis is strongly related to the difficulty in diagnosing this pathology in its early stages. Imaging techniques are of paramount importance since they are responsible for the detection, localization and monitoring of the evolution of neoplastic lesions.

X-ray of the chest and CT imaging have already shown a certain potential in the identification of some types of lung cancer and pulmonary nodules. Nonetheless, the ionizing radiation typical of these imaging techniques limits their use, especially in newborns and old patients. Similarly, the continue monitoring of a suspected neoplastic lesion or its follow-up after a therapy remain critical and matter of debate, since secondary radiation-induced pathologies may arise in the patient.

Also in this case, lung MRI presents a strong potential because of its good resolution, absence of ionizing radiation, and good soft tissue contrast. For instance, respiratory-gated Cartesian spin-echo acquisitions were shown to be useful in the detection and follow-up of lung carcinomas in mice.

In the following work, optimized lung MRI techniques (gated- and non-gated-FLASH sequences and an UTE sequence) are compared to investigate their potential as noninvasive approaches for NSCLC MRI *in vivo* detection and follow-up in a mouse model of lung adenocarcinoma. The advantages and the limitations of free-breathing UTE MRI will be discussed in the light of the obtained results.

Pages 65-73 have been removed from this *diffusion version* of the Ph.D. thesis since they contained an article protected by editor copyright. Only the abstract will be reported hereafter.

The removed article is:

In vivo Magnetic Resonance Imaging for effective non-invasive detection and follow-up of an orthotopic mouse model of lung cancer

A. Bianchi, S. Dufort, P.-Y. Fortin, F. Lux, G. Raffard, N. Tassali, O. Tillement, J.-L. Coll, Y. Crémillieux

NMR in Biomedicine, in press

The full article can be downloaded at:

http://onlinelibrary.wiley.com/doi/10.1002/nbm.3142/abstract

A copy of the *reference version* of this Ph.D. thesis can be accessed at the Library of the University of Bordeaux. For further details please contact the author of this work (bian.drea@libero.it).

In vivo Magnetic Resonance Imaging for effective non-invasive detection and follow-up of an orthotopic mouse model of lung cancer

A. Bianchi, S. Dufort, P.-Y. Fortin, F. Lux, G. Raffard, N. Tassali,
O. Tillement, J.-L. Coll, Y. Crémillieux

Abstract:

One of the main reasons for the dismal prognosis of lung cancer is related to the late diagnosis of this pathology. In this study, we evaluated the potential of optimized lung MRI techniques as a completely non-invasive approach for non-small-cell lung cancer (NSCLC) MRI *in vivo* detection and follow-up in a mouse model of lung adenocarcinoma expressing the luciferase gene.

Bioluminescent lung tumour cells were orthotopically implanted in immuno-deficient mice. Ultra-short echo-time (UTE) MRI free-breathing acquisitions were compared with standard gradient-echo lung MRI (FLASH) using both respiratory-gated and free-breathing protocols. The MRI findings were validated against bioluminescence imaging (BLI) and gold-standard histopathology analysis.

Adenocarcinoma-like pathological tissue was successfully identified in all the mice with gated-FLASH and non-gated UTE MRI, and good tumour co-localization was found between MRI, BLI and histological analyses. An excellent or good correlation was found between the measured bioluminescent signal and the total tumour volumes quantified with UTE MRI or gated-FLASH MRI, respectively. No significant correlation was found when the tumours were segmented on non-gated MR FLASH images.

MRI was shown to be a powerful imaging tool able to detect, quantify and longitudinally monitor the development of sub-millimetric NSCLCs. To our knowledge, this is the first study which proves the feasibility of a completely non-invasive MRI quantitative detection of lung adenocarcinoma in *freely breathing* mice. The absence of ionizing radiation and the high-resolution of MRI, along with the complete non-invasiveness and good reproducibility of the proposed non-gated protocol, make this imaging tool ideal for direct translational applications.

Keywords:

Lung cancer; MRI; lung MRI; bioluminescence imaging; orthotopic adenocarcinoma model

4

UTE MRI and intratracheally administered contrast agents

In this chapter, the feasibility of using UTE proton MRI to monitor the biodistribution and study the elimination pathways of intratracheally administered gadolinium-based nanoparticles will be shown. A protocol for the quantification of the absolute concentration of a T_1-shortening contrast agent in the lungs using a radial UTE sequence will be proposed. As a result, quantitative pharmacokinetic models will be implemented in lungs and validated with the help of fluorescence imaging. A basic toxicological study to evaluate the short term negligible toxicity of the investigated nanoparticles and of the proposed protocol will be presented.

4.1 Proof-of-concept

The investigations presented in chapter 3 clearly showed the strong potential of UTE MRI in the detection of pathological changes occurring in lung tissue. In particular, the investigation on the asthma model in section 3.1 proved that UTE MRI can allow the quantification of bronchial remodeling in a group of allergen-sensitized mice. Likewise, the study in section 3.2 showed the possibility of detecting submillimetric neoplastic lesions in tumor-bearing rodents. On the other hand, the MR changes involved in the asthma study were shown to be relatively small if considering that strong remodeling features were implicated in the study. Similarly, the need for improving the early detection of small lung cancerogenic formations and for establishing an observer-independent segmentation protocol arose from the study on the NSCLC model.

In a more general way, the studies presented in the previous chapter made clear that UTE MRI is a valuable instrument in the noninvasive detection and monitoring of lung diseases. At the same time they confirmed one of well-known flaw of such an imaging technique, i.e., its limited sensitivity.

As described in section 1.3, the use of properly chosen contrast agents can help to encompass the detection limits of MRI. Among the vast range of contrast media available for magnetic resonance imaging, the category

of T_1-shortening agents was selected for investigation. This choice was connected to a number of theoretical and practical considerations. For instance, one of the aims of this thesis was to implement noninvasive, low-cost and easily-implementable protocols for proton MRI, which excluded the use of hyperpolarized media. In addition, the need to enhance the weak signal changes which take place in diseased lung tissue advocated the use of positive contrast agents, ruling out the employment of iron oxide-based nanostructures. Since the morphological changes of lung parenchyma were of concern, paramagnetic contrast agents were preferred to fluorinated gases or OE MRI, mainly used for ventilation and perfusion studies.

The USRPs were selected for the investigations reported in the next pages. Such nanostructures, compared to commercially available molecular compounds, present several advantages like multimodality, multivalency, and original nanoscale properties which will be demonstrated and discussed in detail in the next sections. At the time of the choice, these nanoassemblies had been already proven to present a negligible hepatic clearance when injected intravenously. This property, discussed *inter alia* in the following article, made the USRPs especially attractive.

Intratracheal instillation appeared to be an attractive route to test these nanoassemblies in healthy mice in combination with the UTE sequence. Indeed, this administration modality allowed the delivery of a known dose of contrast agent directly into the lungs, permitting to easily evaluate the NMR properties of the USRPs and to find the optimal dose range for possible subsequent applications.

The work presented hereafter has been accepted for publication on *Magnetic Resonance in Medicine*, 70:1419–1426 (2013), and its copyright belongs to Wiley Periodicals, Inc.

Pages 77-84 have been removed from this *diffusion version* of the Ph.D. thesis since they contained an article protected by editor copyright. Only the abstract will be reported hereafter.

The removed article is:

Contrast enhanced lung MRI in mice using ultra-short echo time radial imaging and intratracheally administrated Gd-DOTA-based nanoparticles

A. Bianchi, F. Lux, O. Tillement, Y. Crémillieux

Magn Reson Med 70:1419–1426 (2013)

The full article can be downloaded at:

http://onlinelibrary.wiley.com/doi/10.1002/mrm.24580/pdf

A copy of the *reference version* of this Ph.D. thesis can be accessed at the Library of the University of Bordeaux. For further details please contact the author of this work (bian.drea@libero.it).

Contrast enhanced lung MRI in mice using ultra-short echo time radial imaging and intratracheally administrated Gd-DOTA-based nanoparticles

A. Bianchi, F. Lux, O. Tillement, Y. Crémillieux

Abstract:

Purpose: To investigate the in vivo T_1-enhancement of the lung parenchyma in free-breathing healthy mice following intratracheal administration of Gd-DOTA-based nanoparticles, to assess the enhancement kinetics of the instilled contrast medium and to identify its elimination pathways.

Methods: Ultrashort Echo Time (276 μs) proton MRI of the lung was performed (N = 14) at 4.7 T after the intratracheal instillation of 50 μL of seven different concentrations of contrast agent solution (from 2 to 100 mM of Gd^{3+}). The signal enhancement (SE) in lungs, blood, liver, kidneys, and bladder was assessed (N = 3) for a 50 mM concentration solution at different time points.

Results: The largest SE in lungs (266 ± 14%) was observed for a 50 mM solution of Gd^{3+}. In lungs, the SE was observed to decay exponentially with a time constant of 149 ± 51 min. The passage of the nanoparticles from lung tissue to blood and kidneys, and ultimately to the bladder, was observed. No significant hepatic enhancement was measured.

Conclusion: This study demonstrates the feasibility of large SEs of lung tissue using intratracheally administrated solutions of Gd-based contrast agents. In future applications, the SE in lungs could be used to image the biodistribution of coadministrated drug aerosols or to selectively enhance lung diseased tissues.

Keywords:

Lung proton MRI; UTE; gadolinium; contrast agent; nanoparticles

4.2 Biodistribution and pharmacokinetics

The results presented in the previous study were undoubtedly encouraging. The use of a T_1-weighted UTE MR pulse sequence allowed the detection of large signal changes in lung parenchyma. The good temporal resolution enabled by the chosen sequence allowed the study of the evolution of the signal enhancements and having thus a first insight into the biodistribution of the nanoparticles in the lungs. Similarly, a basic study of the elimination pathways of the nanoparticles could be carried out, underlining the favourable pharmacokinetics of the USRPs entirely eliminated through renal filtration.

The study presented in the previous section (see Fig. 2 in the previous article) underlined also an important key property of the employed UTE MR sequence, i.e., the negligibility of the T_2^* effect when working with short TEs and moderately low concentrations of contrast agents. The presence of a strongly dominant image contrast was immediately perceived as a clear advantage of the UTE MR pulse sequence. Nonetheless, a deeper investigation of the NMR theory behind this fact was still missing. Such an insight, presented in the work proposed in this section, was needed to fully exploit the wealth of information that MRI can provide.

In addition, a number of issues and concerns arose from the investigation presented in section 4.1. First of all, the signal changes measured for the USRPs were extremely high but the protocol had not been applied to standard contrast agents. As a consequence, no comparison was available neither in terms of signal enhancements for a given concentration nor in terms of elimination times. Secondly, the described protocol employed a technique (i.e., intratracheal instillation) rather new for contrast agent delivery (compared for example to standard intravenous injections). Considering the potential interest of this promising delivery route and these nanoassemblies in future applications, concerns about the safety of the proposed protocol may be common in the reader. Similarly, the use of nanoparticles arose concerns about the potential acute toxicity of the USRPs.

In the following study, all these concerns and issues were investigated and discussed. When possible, results were validated with the help of a complementary imaging modality, i.e. FRI.

The work presented hereafter has been accepted for publication on *Magnetic Resonance Materials in Physics, Biology and Medicine* (doi:10.1007/s10334-013-0412-5) and its copyright belongs to the European Society of Magnetic Resonance in Medicine and Biology (ESMRMB). The *Supplementary Material* is presented in appendix D for the interested readers.

Pages 86-99 have been removed from this *diffusion version* of the Ph.D. thesis since they contained an article protected by editor copyright. Only the abstract will be reported hereafter.

The removed article is:

Quantitative biodistribution and pharmacokinetics of theranostic multimodal gadolinium-based nanoparticles for lungs using Ultrashort-TE MRI

A. Bianchi, S. Dufort, F. Lux, A. Courtois, O. Tillement, J.-L. Coll, Y. Crémillieux

Magnetic Resonance Materials in Physics, Biology and Medicine, doi:10.1007/s10334-013-0412-5, in press.

The full article can be downloaded at:

http://link.springer.com/article/10.1007%2Fs10334-013-0412-5

A copy of the *reference version* of this Ph.D. thesis can be accessed at the Library of the University of Bordeaux. For further details please contact the author of this work (bian.drea@libero.it).

Quantitative biodistribution and pharmacokinetics of theranostic multimodal gadolinium-based nanoparticles for lungs using Ultrashort-TE MRI

A. Bianchi, S. Dufort, F. Lux, A. Courtois, O. Tillement,
J.-L. Coll, Y. Crémillieux

Abstract:

Objective: To study the biodistribution and lung pharmacokinetics of tracheally administered gadolinium-based contrast agents [gadoteric acid and multimodal ultra-small rigid platforms (USRPs)], to validate their pharmacokinetics against optical imaging of fluorescent USRPs, and to test their short-term toxicity.

Materials and methods: Ultrashort echo-time (UTE) lung proton magnetic resonance imaging (MRI) was performed at 4.7-Tesla (T) after the intratracheal instillation of different concentrations of contrast agent solutions in mice. Pharmacokinetic models were implemented on the absolute concentration calculated from the MRI signal enhancement measurements. Fluorescent USRPs were used to obtain optical images with the same protocol. Bronchoalveolar lavage inflammatory cell count and serum creatinine measurement were performed on four groups of instilled mice (sham, saline, USRPs, lipopolysaccharide).

Results: MR and optical imaging showed similar kinetics of the USRPs, passing from the airways to the lung tissue and to the kidneys, with negligible hepatic clearance. No significant increase of lung and renal inflammation markers were observed in USRP-instilled animals.

Conclusion: A T_1-weighted radial UTE sequence was found to be valuable in quantitatively monitoring the biodistribution and pharmacokinetics of nanoparticles in the lungs of mice. The observed favorable pharmacokinetics, which was validated by fluorescence imaging, ensures the negligible toxicity of the nanoprobes, making the USRPs and the developed protocol good candidates for applications on selected lung diseases.

Keywords:

Lung ; UTE MRI ; Gadolinium-based nanoparticles; Fluorescence imaging; Pharmacokinetics; Multimodal nanoparticles

5

A new protocol for lung tumor detection

In section 3.2, free-breathing proton MRI was shown to be an efficient tool in the detection of lung cancer. UTE MRI, in particular, was shown to be very accurate in the detection of submillimetric lung neoplastic lesions, thanks to its negligible motion artifacts and its sensitivity to lung parenchyma signal changes (as also demonstrated in section 3.2).

Nonetheless, MR imaging techniques present a lower sensitivity compared to standard nuclear medicine imaging modalities. To encompass this intrinsic limitation and to further improve the detection efficiency for lung cancer, the use of positive contrast agents can be sought. In this sense, as shown in chapter 4, T_1-weighted UTE MRI sequences are good candidates to accurately study the signal changes induced by the presence of paramagnetic atoms in lungs.

In this chapter, the oral administration of gadolinium-based nanoparticles, proposed and discussed in sections 4.1 and 4.2, will be applied to the study of the lung cancer model previously described (see section 3.2). A quantitative comparison between such administration modality and a more conventional one (i.e., intravenous injection) will be proposed. The sensitivity, specificity, contrast enhancement and pharmacokinetics of this intrapulmonary administration route will be evaluated. Complementary imaging modalities will be used in order to validate the results observed with proton UTE MRI.

The work presented hereafter has been published on *Proceedings of National Academy of Sciences USA*, 111(25):9247-9252 (2014), and its copyright belongs to the National Academy of Sciences USA.

Pages 102-110 have been removed from this *diffusion version* of the Ph.D. thesis since they contained an article protected by editor copyright. Only the abstract will be reported hereafter.

The removed article is:

Targeting and in vivo imaging of non-small-cell lung cancer using nebulized multimodal contrast agents

A. Bianchi, S. Dufort, P.-Y. Fortin, F. Lux,
N. Tassali, O. Tillement, J.-L. Coll, Y. Crémillieux.

Proceedings of National Academy of Sciences USA,
111(25):9247-9252 (2014)

The full article can be downloaded at:

http://www.pnas.org/content/early/2014/06/04/1402196111.abstract

A copy of the *reference version* of this Ph.D. thesis can be accessed at the Library of the University of Bordeaux. For further details please contact the author of this work (bian.drea@libero.it).

Targeting and in vivo imaging of non-small-cell lung cancer using nebulized multimodal contrast agents

A. Bianchi, S. Dufort, P.-Y. Fortin, F. Lux, N. Tassali, O. Tillement, J.-L. Coll, Y. Crémillieux

Abstract:

One of the main reasons for the dismal prognosis of lung cancer is related to the late diagnosis of this pathology. In this work, we evaluated the potential of optimized lung MRI techniques and nebulized ultrasmall multimodal gadolinium-based contrast agents [ultrasmall rigid platforms (USRPs)] as a completely noninvasive approach for non-small–cell lung cancer (NSCLC) in vivo detection. A mouse model of NSCLC expressing the luciferase gene was developed. Ultrashort echo-time free-breathing MRI acquisitions were performed before and after i.v. or intrapulmonary administration of the nanoparticles to identify and segment the tumor. After orotracheal or i.v. administration of USRPs, an excellent colocalization of the position the tumor with MRI, bioluminescence and fluorescence reflectance imaging, and histology was observed in all mice. Significantly higher signal enhancements and contrast-to-noise ratios were observed with orotracheal administration using lower doses, reducing the toxicity issues and the interobserver variability in tumor detection. The observations suggested the existence of an unknown original mechanism (different from the enhanced permeability and retention effect) responsible for this phenomenon. MRI and USRPs were shown to be powerful imaging tools able to detect, quantify, and longitudinally monitor the development of submillimetric NSCLCs. The absence of ionizing radiation and high resolution MRI, along with the complete noninvasiveness and good reproducibility of the proposed protocol, make this technique potentially translatable to humans. To our knowledge this is the first time that the advantages of an orotracheal administration route are demonstrated for the investigation of the pathomorphological changes due to NSCLCs.

Keywords:

Lung tumor; magnetic resonance imaging; bioluminescence imaging; gadolinium-based nanoparticles

6

Discussion and perspectives

In this chapter, a short discussion about the advantages and limitations of the protocols developed, implemented and validated will be proposed for each published or submitted article. The short- and long- term perspectives of each work will be analyzed, with a special attention to the on-going experiments. Finally, some side applications originated from the work presented in this thesis will be briefly presented.

6.1 UTE MRI applications on lung diseases

The pathologies investigated in chapter 3, namely asthma and lung cancer, are both frequent and responsible for several millions of deaths each year worldwide. Even when not lethal, these diseases can severely hamper the quality of life of patients. In addition, the cost of medications and hospitalizations along with the indirect non-medical costs (i.e., absence from work) related to these diseases represent a social burden under the economic point of view.

Understanding the mechanisms behind these pathologies is fundamental in order to develop new therapeutic approaches. Similarly, noninvasive and effective diagnostic instruments are required to detect the diseases in their early stages, which very often results in a positive prognosis, increased life expectancy or improved quality of life of the patient. In this context, imaging techniques have a role of paramount importance since they allow for early detection of pathologies, they help preparing and guiding surgery, they allow for noninvasive longitudinal follow-ups of the patients, and they permit to study the effects of new therapeutic drugs.

In chapter 3, UTE MRI has been chosen to study the noninvasive detection, investigation and follow-up of these lung diseases in two animal models. The rationale behind this choice has been widely illustrated in the introduction of the manuscripts, in the Preface and in chapter 1.

6.1.1 Asthma

Among the vast number of asthma models existing in scientific literature [151–154], the OVA-sensitization protocol proposed by Henderson *et al.* [155] was chosen for the study. The reasons of such a choice are mainly due to the fact that this model well represents the slow development of allergen-induced asthma in humans. In addition, the murine model investigated in the study presents all the main hallmarks of such pathology, developed at different stages and time points. A further advantage of the OVA-sensitization model is related to the fact that it had been extensively characterized under the biological point of view before the beginning of the study reported in section 3.1.

When the study on the OVA-sensitization model was started, Lederlin *et al.* [156] had shown that an index defined similarly to the Peribronchial Signal Index (PBSI), measured with micro-CT, correlates well with the bronchial smooth muscle size measured on histological slices[1]. The group was able to find a significant difference between the OVA-sensitized mice and the controls at day 76, studying the same asthma model. Only the baseline time point and the endpoint at day 76 was studied by the group, due to the terminal procedures employed to perform histological analyses.

In a successive article, Lederlin *et al.* [157] extended the OVA model characterization to three different time points, as shown in Figure 6.1. They clearly showed an increasing cell infiltration in the peribronchial space during the first two time points (days 35-37 and 75-77) in OVA-sensitized mice. A strong decrease in the inflammation was observed at the third time point, roughly one month after the last administration of ovalbumin. As for the bronchial remodeling, strong remodeling features were observed in allergen-sensitized mice at the second time point (days 75-77) but not at the first time point (days 35-37). Significant remodeling features were observed also at the third time point, but not as intense as at the second time point.

The work presented in section 3.1 has been limited to the study of the first two time points (days 35-37 and 75-77) of the same asthma model, as a proof-of-concept[2]. The obtained results go on the same direction of Lederlin's ones, showing the feasibility of monitoring peribronchial changes after allergen-sensitization in order to distinguish between mice that underwent bronchial remodeling features and controls [156, 157]. In this sense, the work

[1] The index defined by Lederlin *et al.* was called peribronchial density index (PBDI) and was computed in the same way as the PBSI, using the Hounsfield unit scale instead of the SNR in the peribronchial measurements [156].

[2] The data presented in the second article of Lederlin *et al.* [157] were published when the work in section 3.1 was already under peer-review.

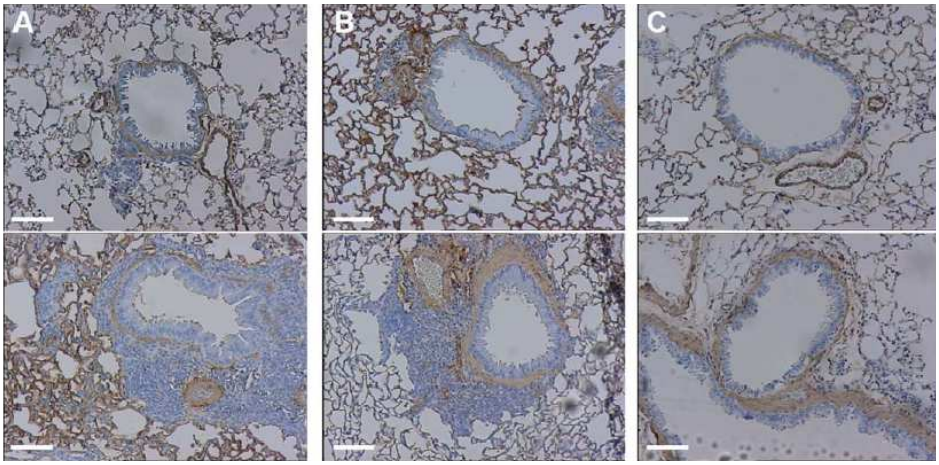

Figure 6.1: Typical optic microscopic images (100X) from bronchial sections from control (top) and OVA-sensitized mice (bottom). Bars represent 85 μm. α-smooth muscle actin staining (in brown) underlines bronchial remodeling features (smooth muscle mass increase) while nuclei are stained in dark blue to study cell infiltration. Reprinted from [157]

presented in this thesis on the asthma model can be considered the nontrivial transposition of micro-CT results to MRI with respect to the bronchial remodeling studies.

Such a result could be accomplished because of the simultaneous high resolution and significant SNR achieved in lung parenchyma, obtained thanks to the properties of UTE MRI. The resolution obtained in MRI images was still inferior to the one of Lederlin *et al.* in their micro-CT studies. As a consequence, the identification of bronchi in MRI images was performed by two independent users and only the bronchi identified by both of them were used for subsequent analysis[3]. Nonetheless, the images obtained with MRI, contrarily to the micro-CT ones by Lederlin *et al.*, were acquired using a noninvasive free-breathing protocol. The absence of ionizing radiations is a further advantage of the proposed protocol compared to micro-CT. Furthermore, the possibility of accurately identifying and quantifying inflammatory volumes using UTE MRI was confirmed in the work presented in section 3.1.

Perspectives Before being able to exploit this protocol in pre-clinical studies to evaluate the potential of selected lead compounds for bronchial remodeling treatment, a further investigation of the PBSI index should be sought. In particular, it would be important to understand if (and, in case, to what extent) this index is affected by the peribronchial inflammation. As discussed

[3]The identification of bronchi with micro-CT was performed using multiplanar reformation by a single user [156].

in the publication of section 3.1, data seem to suggest that inflammation has low or no influence on PBSI. Nonetheless, extending the model to a time point characterized by bronchial remodeling in absence of inflammation would shed light on this matter.

Preliminary studies have been conducted on the third time point described by Lederlin *et al.* [157]. As shown in Figure 6.2, no significant difference was observed between controls and OVA-sensitized mice with respect to inflammation. On the other hand, an increase in the PBSI index was observed between the two groups, even though the Wilcoxon's signed-rank test resulted in a non-significant difference. The reasons for this finding may be related to the fact that the remodeling features developed by the OVA-sensitized mice at day 110-112 are less strong than the ones at days 75-77.

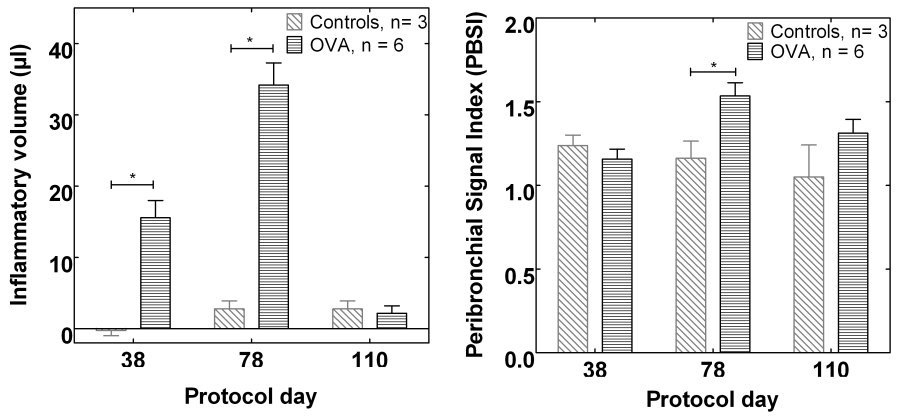

(a) Inflammation (b) PBSI

Figure 6.2: Bar plots showing (a) the MRI inflammatory volumes and (b) the PBSI at the different time points, calculated using the protocol described in section 3.1. The data relative to the first and second time point (days 38 and 78) are the one reported in the published article. The data obtained at day 110 belong to the preliminary test performed on the third time point of Lederlin's asthma model. The bar plot in figure (a) shows that, at day 110, no difference exists between the OVA-sensitized mice and the controls. The increase in the PBSI in allergen-sensitized mice at day 110 is not significant, probably due to the small number of animals employed in the preliminary study. Reprinted from [158]

An increase in the number of animals would therefore be required to identify these smaller changes. Since in this animal model the bronchial remodeling features are spontaneously regressive (in a slow but progressive way) after the end of the sensitization protocol, a time point with purely bronchial remodeling features may be obtained treating mice with glucocorticoid steroids close to day 75. Budesonide, for example, was shown to be

able to significantly accelerate inflammation resolution if given 24 hours post allergen challenge [58]. This protocol would in principle allow to have a time point with strong remodeling features (like the second time point of Lederlin's model) but negligible inflammation (like the third time point of Lederlin's model).

Finally, it has to be noted here that, for a systematic applicability of this protocol to generalized pre-clinical studies of drug tests, an automated process for the data analysis should be implemented. The analysis performed in the work is indeed effective and well reproducible but rather time-consuming. The implementation of an automatic segmentation procedure should therefore be sought and tested.

6.1.2 Lung cancer

In section 3.2, the advantages and limitations of UTE MRI compared to optimized gradient-echo sequences have been discussed. The protocol used has permitted to effectively detect lung cancer in a model of adenocarcinoma, as confirmed by BLI and histology. The encouraging results could be easily applied to other models of lung cancer in order to identify which forms of lung neoplasm can be detected in their early stages using this advantageous imaging techniques. The protocol could be applied to the preclinical study of the therapeutic effects of selected lead compounds for cancer treatment.

The investigation left open two main issues: (i) the possibility of using contrast agents to improve the sensitivity of the imaging technique employed and (ii) the applicability of the protocols in humans. The former issue has been answered in chapter 5 whereas the latter is still pending. Noninvasive UTE MRI techniques have indeed been applied in volunteers at the University of Bordeaux with satisfactory results in terms of SNR measured in lung parenchyma [83]. Testing these sequences in lung cancer-bearing patients could be one of the next steps.

6.2 UTE MRI and intratracheally administered contrast agents

The interest of contrast agents for MR imaging dates back to the early 80's [76, 126]. Since then, several exogenous contrast agents have been developed for different purposes. Nonetheless, only few of them are currently in use in clinical practice and only for rather specific applications, partially because of the strict requirements on contrast media imposed by regulatory agencies.

In the field of MRI lung imaging, several techniques have been experimentally used to study pulmonary ventilation, perfusion and diffusion in a number of pathologies [91]. In chapter 4, a protocol for the visualization and the quantitative study of the signal changes of lung parenchyma after the administration of a paramagnetic contrast agent has been proposed. The protocol has several advantages related to the use of a radial UTE MRI sequence. In particular, the constant TR, enabled by the free-breathing radial acquisitions, permits to maintain a stable image contrast. As a consequence, data acquired at different times can be accurately compared (which wouldn't be possible, for instance, using perspective gating techniques). Furthermore, the T_1-weighting contrast of UTE sequences allows to reduce to the minimum the T_2^* effects.

As a result, quantitative PK models have been implemented and applied to the study of contrast agents biodistribution and elimination pathways. The protocol is applicable to a generic paramagnetic contrast (e.g., Dotarem) and not only to the specific nanoparticles used throughout the thesis (see section 6.5). Nonetheless, the protocol is based on the negligibility of the T_2^* effect, which depends mainly on the contrast agent properties (mainly its r_2^*), on the used concentration and on the chosen sequence parameters (mainly TE). Such negligibility has to be assessed prior to the implementation of the PK models. Unfortunately, the relationship intercurring between these parameters is not easy and the quantification of the transverse relaxivity of the contrast agent is complicated by the fact that its value depends on the spin-spin transverse relaxation but also on the tissue, MR sequence parameters and magnetic field inhomogeneities. This means that the r_2^* cannot be easily measured, imposing an empirical approach to verify if the T_2^* effect is negligible and thus if the PK models can be effectively applied to the data. In the case of the USRPs, this assessment was conducted in section 4.1 and served as basis for the work in section 4.2.

Perspectives The UTE MRI protocols implemented in chapter 4 have been extensively used in chapter 5. Furthermore, several on-going studies employ these techniques in the study of the pathological changes that take place in the lungs or in other organs. A description of the general perspectives and applications of these protocols is proposed in the next sections. The limitations and perspectives of the chosen administration modality are briefly discussed in section 6.4.4.

Strictly speaking about the PK models and the contrast agent protocol implemented in section 4.2, a validation of the absolute concentration mea-

surement is still pending. As discussed in the relative manuscript, the use of SPECT imaging with USRPs-^{111}In could be an effective way to validate the absolute values obtained with MRI. Even though the presented results are valid independently of this pending assessment, the accurate knowledge of the absolute concentration of the contrast agent in the healthy and diseased tissues would permit to best exploit the therapeutic properties of the USRPs nanoparticles (see appendix B). It would indeed permit to tailor the radiation therapy according to the accumulation effect measurable with MRI, optimizing the theranostic efficacy of these nanoassemblies. Obviously, the possibility of quantifying the absolute concentration of a contrast agent in a tissue using UTE MRI would have many applications for different organs and fields, and it's therefore a short-term study that has to be undertaken.

Finally, to further improve the precision of the implemented PK models and with a view to the absolute concentration quantification, further studies are needed to evaluate the best values for the *in vivo* longitudinal relaxivity of the nanoparticles and for the longitudinal relaxation time of the lungs $T_1(0)$. Knowing this information would enable to exploit all the information that the PK models may offer like, for example, the clearance rate and bioavailability of the contrast medium in the various compartments.

6.3 A new protocol for lung tumor detection

In chapter 5, the protocol developed in chapter 4 was successfully applied to the lung cancer model studied in section 3.2. The investigation clearly showed that improvements in terms of SNR and CNR can be obtained using gadolinium-based nanoparticles in conjunction with T_1-weighted UTE MRI sequences, with straightforward advantages in the detection and segmentation of small lung cancer lesions.

In addition, the work showed for the first time that the oral administration can be an advantageous delivery route for the detection of pathomorphological changes due to lung cancer. The breadth of this finding is not limited to the simple administration of MRI contrast agents for NSCLCs detection. The potential application of this result may indeed be extended to other imaging modalities, may include the establishment of effective innovative protocols for the detection of other lung pathologies (different from lung cancer) but also for the study of the efficacy of specific drugs for lung diseases therapy.

Some of the perspectives of these results and of this promising protocol will be discussed in the next section.

6.4 General perspectives

The article presented in chapter 5 contains the last validated results which will be shown in this thesis. The work has left open a number of possible perspectives that are currently under study. First of all, only the passive targeting mechanisms have been tested even though the USRPs allow grafting compounds for active targeting on their surface or coating. Secondly, the USRPs and the intratracheal administration have been tested only on one model of pulmonary disease but they can be exploited to study other pathologies, in lungs or in other organs (e.g., brain).

Hereafter these aspects will be explored in more detail and preliminary results about the on-going studies will be described. Some long-term future potential applications of the USRPs and the developed MRI protocols will be proposed.

6.4.1 Oral administration and active targeting USRPs

As mentioned in section 2.2.2, after the top-down process that leads to the formation of the nanoparticles, 30 to 40% of DOTA ligands are free. For the USRPs used in this work, supplementary paramagnetic atoms were provided to increase the total relaxivity of the nanoassemblies. Similarly, Cy 5.5 was covalently grafted on them when needed to perform FRI studies.

As detailed explained in the patent referenced in appendix A, the free DOTA and the available carboxylic functional groups (COO^-) can be exploited also in different ways. Among these, grafting specific targeting molecules or peptides on the nanoassemblies is the one that will be considered here and that is currently under study. This possibility, enabled by the flexible structure of the USRPs, can be exploited to actively target specific diseases, instead of relying solely on the EPR effect or generic passive targeting mechanisms.

In this context, the idea is to use as targeting compound of choice the RGD (arginine-glycine-aspartic acid), a tripeptide which was shown to be able to recognize and target the integrin $\alpha_v\beta_3$ [159], transmembrane receptors that play a fundamental role in angiogenesis and cancer development [160, 161].

Integrin targeting and oral administration Integrin $\alpha_v\beta_3$ has a particular pattern of expression in lung cancer [162, 163]. In normal tissues, this integrin is expressed on the basal face of a few types of cells, where it mediates adhesion between cells and the extracellular matrix. While its level of expression is undetectable in normal quiescent endothelial cells, it is expressed at 10^5 or 10^6 copies/cells on the endothelial cells of growing or remodeling capillaries

during angiogenesis, typical feature of asthma bronchial remodeling and growing tumors.

Accessibility to an RGD ligand coming from the bloodstream is questionable since most of these $\alpha_v\beta_3$ integrin receptors are located on the 'hidden' side of the endothelial cells and are engaged in an interaction with the extracellular matrix. This is also true to a certain extent for cancer cells. Actively growing and/or migrating metastatic tumor cells on the periphery of a tumor will present increased levels of $\alpha_v\beta_3$ integrin than those present in the center of the tumor. In addition, the presence of a tumor induces a remodeling of the normal surrounding stromal tissues, and a cross talk exists between the stroma and the tumor. This is accompanied by an overexpression of the $\alpha_v\beta_3$ integrin on the surface of normally negative cells of the stroma, but also by an abnormal presence of this integrin on the apical and lateral sides of these cells.

It thus becomes reasonable to hypothesize that approaching these cells by the airway may be more effective than via the bloodstream.

On-going studies: active targeting USRPs for lung cancer The USRP-RGD nanoparticles have been already synthesized and characterized by the 'Institut Lumière Matière' of the University of Lyon. In particular, among the vast number of RGD motifs, the class of cyclic arginine-glycine-aspartic acid (cRGD) paptides was selected. These cyclic compounds have indeed shown a much higher stability compared to the linear RGD peptides, better pharmacokinetics (renal clearance) with negligible toxicity and an improved receptor specificity and affinity for tumor targeting [159, 164, 165]. Proper control nanoparticles were synthesized using cRAD (cyclic arginine-alanine-aspartic acid) tripeptides, which differ from cRGD in only one amino acid. On average, 2.5 cRGD (or cRAD) per nanoparticle were observed. Covalent grafting of Cy 5.5 for FRI studies is still possible when cRGD is grafted on the nanoparticles.

These nanoparticles have already been tested at the University of Grenoble in a subcutaneous xenografted tumor in immunodeficient mice. As shown in Figure 6.3, a significant increase in tumor targeting was observed when the USRP-cRGD nanoparticles were administered intravenously, compared to USRPs-cRAD or USRPs-Cy.

In the light of these considerations, the USRPs-cRGD will be applied in the next month(s) to the NSCLC model developed in section 3.2, comparing both the intratracheal and the intravenous administration routes as described in chapter 5.

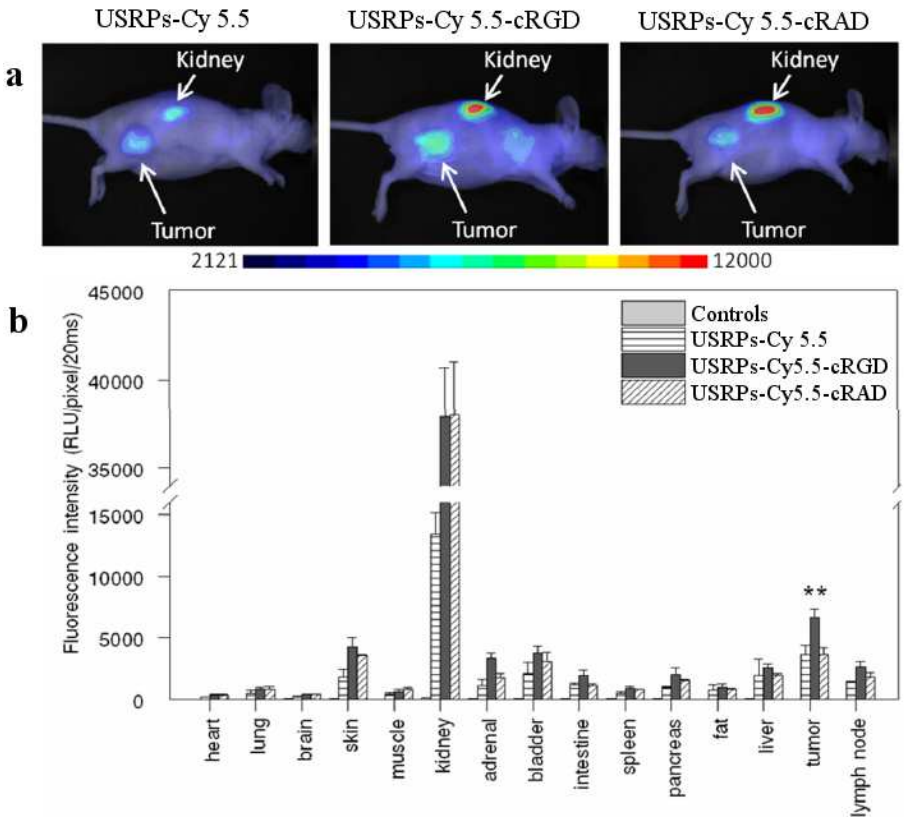

Figure 6.3: (a) FRI images showing the accumulation of USRPs-Cy, USRPs-cRGD or USRPs-cRAD in a xenografted subcutaneous tumor 24 hours after intravenous administration. (b) Biodistribution in organs after administration of the three different type of nanoparticles 24 hours after the administration. A significant increase in tumor targeting was observed when the USRP-cRGD nanoparticles were administered intravenously, because of the active targeting potential of cRGD. Adapted from [166].

Future studies: active targeting USRPs for asthma In section 3.1 it was shown that bronchial remodeling features can be noninvasively detected using optimized UTE MRI protocols. Nonetheless, the study showed that the employed imaging technique has a spatial resolution that is still inferior compared to micro-CT, making the analysis of the bronchial remodeling features less simple. Even though a good reproducibility was observed, further improvements in the imaging protocol are desirable.

As described in section 1.1.2.1, angiogenesis is an important feature associated to bronchial remodeling in asthma patients. Considering that cRGD has been proven to be capable of targeting the integrin $\alpha_v\beta_3$ [159] regulating the angiogenesis process [160,161], USRPs-cRGD appear to be good candidates to

target and thus investigate bronchial remodeling. In this sense, the UTE MRI protocols implemented in this work are doubly advantageous since: (i) they allow to have high resolution along with significant SNR in lung parenchyma (see section 3.1) and (ii) they enable the detection of small signal changes in lungs after the administration of gadolinium-based nanoparticles (see section 4.1).

In principle, the use of USRPs-cRGD could enhance the changes that take place in the bronchial wall and enable a noninvasive investigation of the evolution of this disease in function of time. In particular, beside the diagnostic advantages, this would permit to study effectively the effect of therapeutic drugs for bronchial remodeling in pre-clinical studies. If the accumulation of the USRPs-cRGD in the remodeled bronchial walls was confirmed, grafting therapeutic lead compounds on these nanocarriers would therefore permit to delivery therapeutic drugs directly on-site.

6.4.2 Application of USRPs to other lung models

The UTE MRI protocols implemented in this thesis have been successfully applied to detect lung cancer. The sensitivity of the technique was notably improved using paramagnetic contrast agents and a favourable administration route. The advantages observed in the study of NSCLCs could be extended to various models of lung disease, different from the ones described in chapter 3. For instance, the application of the USRPs on an LPS model of severe inflammation and on a model of lung fibrosis in mice are currently on-going. In addition, the pioneering experiments proposed in references [94, 95] to study the ventilation and perfusion defects of murine models of pulmonary embolism or acute unilateral airway obstructions could be easily reproduced to study the improvements achievable with the optimized protocols described in this thesis.

Hereafter, the interesting preliminary results (to be confirmed) relative to the on-going study on a murine fibrosis model are briefly presented.

Lung fibrosis Pulmonary fibrosis is a restrictive disease of the lung (see section 1.1.2) characterized, among other things, by the thickening of the blood-air barrier. Being a progressive and lethal disease, early and sensitive diagnostic tools and follow-up imaging techniques are essential to increase the life expectancy of patients suffering from this lung pathology and to test new promising drugs.

The idea behind this on-going study is to investigate whether the use of the USRPs permits to increase the diagnostic sensitivity of this pathology, using a

UTE MRI protocol similar[4] to the one presented in chapter 5. Similarly, the possibility of evaluating the severity of lung fibrosis studying the diffusion and the elimination time constants of the USRPs (using PK models implemented in section 4.2) is under consideration.

The biological model used in this preliminary study is the one widely described by Egger *et al.* [79], which employs various oropharyngeal administrations of bleomycin in mice over a period of 6 days.

As already shown by Babin *et al.* [89, 90], the development of lung fibrosis in bleomycin-injured mice can be successfully monitored *in vivo* using standard gradient-echo sequences. Similarly, Egger *et al.* [79] were able to accurately follow the progression of lung fibrosis using UTE MRI.

As shown in Figure 6.4, the intratracheal instillation of 50 µL of a 50 mM solution of USRPs seems to result in large Signal Enhancements (SEs) (> 300%) in the area of bleomycin-induced lesions, which makes even easier the detection of the fibrotic lesion and of its contours in UTE MR images.

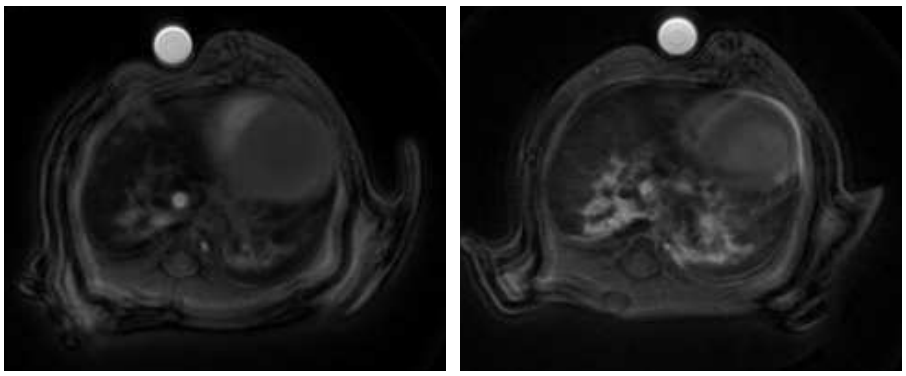

(a) Before USRPs (b) 33 min after USRPs

Figure 6.4: UTE MRI axial image of a bleomycin-sensitized mouse (a) before and (b) after the intratracheal instillation of the USRPs. The fibrotic lesions are enhanced after the administration of the contrast. Images were acquired 30 days after the end of the sensitization protocol to avoid the inflammation regime that follows the bleomycin administrations during the first 3 weeks. Courtesy of Dr. N. Tassali.

Longer elimination time constants have been observed in animal with fibrosis (≈ 245 min), compared to controls (≈ 185 min). This observation suggests a prolonged retention of the contrast agent within the diseased lung tissue, probably related to the hampered access of the nanoparticles to the capillary blood vessels and their subsequent renal elimination.

[4] The main difference is related to the fact that this study is currently performed on a 7 T Bruker spectrometer for technical reasons.

No significant difference has been observed in the diffusion times between bleomycin-sensitized mice and controls. This fact can be related to an effective absence of difference in the diffusion constants or to the need of increasing the number of animals to obtain more stable averages and smaller SEM (since the values of diffusion constants are rather small and the biological variability quite significant, a proper number of animals is needed to see possible small variations).

Further investigations, including *ex vivo* imaging techniques and a higher animal statistics, are needed to validate these observations and to further understand the behavior of the contrast agents within bleomycin-induced injured lung. However these preliminary results represent a first and clear demonstration of the potential of intratracheal administration of contrast agents and UTE lung MRI for imaging and characterizing the presence of fibrotic tissue in bleomycin-treated animal models.

6.4.3 Application of USRPs to other tumors: brain cancer study

When the USRPs are instilled intratracheally, because of their small HD, they have been shown to pass from the lung parenchyma to the bloodstream, with an elimination time constant of about 3 hours (see chapter 3). Once in the bloodstream, a fraction of the nanoparticles can then theoretically passively accumulate in any body tumor for EPR effect, in a similar way to intravenously administered nanoparticles. The nanoparticles will be later on filtered by the kidneys and eventually excreted via urine.

Preliminary studies conducted by the University of Grenoble using FRI and USRPs-Cy showed that this idea was implementable. They indeed observed that intratracheally administered USRPs-Cy tend to accumulate in a subcutaneous xenotransplanted tumor (U87-MG cells implantation). An *in vivo* MRI longitudinal study of brain cancer detection in tumor-bearing immunodeficient mice through intratracheally- and intravenously- administered USRPs has been started. The works exploits the protocols implemented in this thesis and the encouraging results will be object of a scientific publication submission in the close future.

Material and methods At day 0, an orthotopic implantation of U87-MG tumor cells ($5 \cdot 10^5$ cells/mouse) was performed in mice brain through an intracranial administration in immunodeficient mice. Animals (n=14) were repeatedly imaged with MRI between day 8 and day 15 (reproducibility and

follow-up study) according to a protocol similar[5] to the one described in section 4.1. After the acquisition of MR baseline images, the contrast agent solution was administered to the mice at different days and MR images were acquired at different times (from 5 minutes up to several hours after the administration). Between two different administrations on the same mouse, at least 2 days without any handling was foreseen in order to allow a complete elimination of the previously administered contrast agents. In detail, a subgroup (n=4) received an intravenous administration of USRPs 200µL 50mM Gd^{3+}. A subgroup (n=6) received an intratracheal administration of USRPs 50µL 200 mM Gd^{3+}. A subgroup (n=4) received an intratracheal administration of USRPs 50µL 200 mM Gd^{3+} and an intravenous administration of USRPs 50µL 200 mM Gd^{3+} 2 days after.

Results Before the administration of contrast agent, UTE MR images allowed the identification of the presence of brain tumor only in a small number of animals, generally only when the tumor was in its latest stages. Furthermore, the contours of the carcinogenic formations were not easily identifiable (Figure 6.5a). After intratracheal or intravenous administration of USRPs, a good localization of the position of the tumor with MRI was observed, as shown in Figures 6.5b and 6.5c. The comparison of SE and increase of CNR

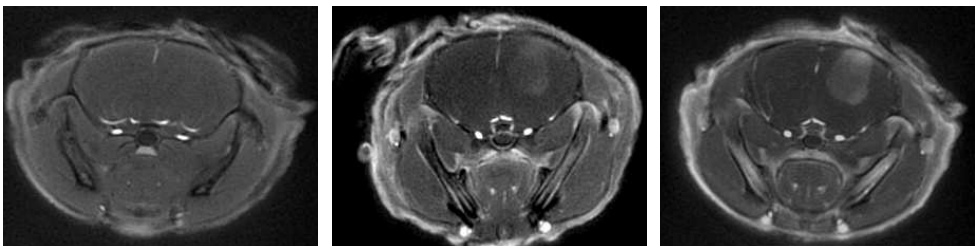

(a) Before contrast agent (b) Intracheal administration (c) Intravenous administration

Figure 6.5: UTE MR images (a) before and after the (b) intratracheal administration of 50µL 200mM USRPs or (c) intravenous injection of 200µL 50mM USRPs.

in the identified tumors (Figure 6.6) showed approximately two-fold higher values for the intravenous (200µL 50mM) administration with respect to the intratracheal one (50µL 200mM), using the same amount of Gd^{3+}. The SE of the tumor was slightly longer after intratracheal administration (elimination constant = 75 ± 12 min) compared to intravenous administration (elimination constant = 55 ± 16 min). The mice that received an intratracheal administra-

[5]The main difference is related to the fact that this study was performed on a 7 T Bruker spectrometer for technical reasons.

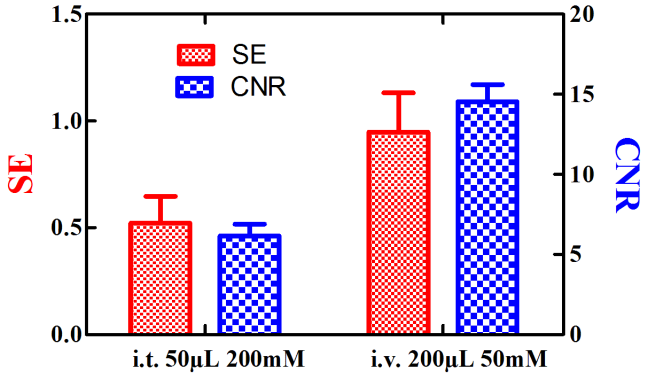

Figure 6.6: Bar plot of tumor SE (left scale) and CNR (right scale) after intravenous (i.v.) and intratracheal (i.t.) administrations.

tion of USRPs at a 2 days distance showed no significant differences in tumor size, position, SE and CNR, confirming the reproducibility of the protocol. Conversely, the comparison of the tumor size after intratracheal administration at 8 days distance showed a significant increase in the tumor volume as quantified with MRI.

Discussion In this study, the results show that the sensitivity of T_1-weighted UTE MRI for the detection of glioblastoma-like tumors can be increased using T_1-shortening contrast agents. Both the administration modalities investigated allow the visualization of tumor position and borders in all the mice, confirming the detection efficiency of UTE MR combined with contrast media. This observation indicates that both the administration routes can be effective for tumor visualization and follow-up.

The accumulation of the nanoparticles in the brain tumor after intravenous injection can be attributed to the disrupted blood-brain barrier, the enhanced permeability and retention effect, and passive targeting mechanism.

Although lower SE and CNR are observed in the tumor after intratracheal administration of USRPs compared to intravenous injection, the intratracheal administration presents several interesting properties. First of all, it is less invasive than a standard parenteral systemic administration. This intratracheal administration modality can be considered as a first step towards a completely noninvasive administration procedure like nebulization or aerosol which can be potentially repeated *ad libitum* in preclinical or clinical studies (see next section).

Secondly, the slow diffusion of the Gd-based contrast agents from the lungs to the bloodstream and then to the tumor tissue can be advantageously used

in combination with interventional or therapeutic procedures, for instance radiosensitization (see appendix B) or opening of the blood-brain-barrier.

In conclusion, the observed high reproducibility and efficacy of the protocol, altogether, make the intratracheal administration of these multimodal nanoassemblies a good candidate for early brain cancer detection and non-invasive follow-up of the diseases. In addition, the previously demonstrated negligible acute toxicity of the USRPs and favorable pharmacokinetics, and the possibility of lung administration with a simple aerosol, altogether, make the proposed protocol potentially translatable to human studies (see section 6.4.4). This is the first time that a study shows that the synergic employment of a T_1-weighted UTE MRI sequence and intratracheally-administered gadolinium-based nanoparticles allow the high-precision detection of brain tumor and of its contours.

Further studies are being performed to confirm the observed results and to better understand the accumulation mechanisms in the tumor after intratracheal administration, using fluorescent USRPs.

6.4.4 Translational considerations

To envisage translational applications, the imaging protocols must be noninvasive. Similarly, the contrast agent must comply with a number of requirements that ensure its negligible toxicity (see section 1.3.2) and minimal side effects.

The MR imaging protocols implemented in this thesis are indeed non-invasive and can be repeated several times, at different time points. In this respect, radial UTE MRI has been shown to be a promising sequence which can be applied in clinical studies of lung morphology, physiology and pathologies [6, 83, 84].

Nonetheless, when envisioning human applications, a limitation of the imaging protocols with contrast agents developed in this thesis can be found in the chosen administration modality, i.e. the intratracheal administration. Even though it was shown that this administration route is safe in mice (see section 4.2 and appendix B), this modality is rather invasive to be considered for translational applications.

As detailed explained in 4, such an administration route was primarily chosen in order to reach directly the lungs and investigate the NMR properties of the USRPs. However, as mentioned throughout the thesis, the advantages of reaching the lungs via the airways are multiples. In this sense, the results presented in chapter 5 strongly support this idea and underline the potential

interest of the oral route in the diagnostics and investigation of pulmonary pathologies.

Keeping these assets in mind, other noninvasive oral administration modalities can be considered as an alternative to the intratracheal administration. In particular, the oropharyngeal aspiration and the intranasal route are currently under consideration as intermediate steps before the investigation of the aerosol. Detailed descriptions of the advantages and limitations of all these administrations routes are reported in references [79, 90, 167–169]. It is noted here that, while less invasive than the intratracheal instillation, passing through the nose imply the addition of a first-pass filter in the pathway of the nanoparticles. This change may affect the final result and the toxicity outcome. More studies are needed to clarify the effective applicability of these techniques to the implemented protocols.

Finally, as clearly stated above and in section 4.2, detailed studies are needed (on two different animal species, one of which should be different from rodents [170]) to ensure the long-term non-toxicity of these nanoassemblies. This is a *conditio sine qua non* to envisage any possible application of the USRPs on humans. Further studies on the *in vivo* stability of the nanoparticles are also needed.

6.5 Other applications of the described protocols

As stated in the Preface, one of the objectives of this thesis was to implement MRI protocols flexible enough to be used to study a generic contrast agent. In this section, some of the contrast agents tested with the protocols developed in this thesis are briefly presented to demonstrate the wide interest of the developed protocols.

6.5.1 Application to upconverting nanoparticles

In this thesis, MRI results have often been validated by FRI observations (see section 4.2 and appendix B). The combination of these imaging modalities permits to put together high sensitivity and resolution and is of great interest in molecular imaging. To achieve this multimodality the design of new nanomaterials appears as one of the most promising options. A collaboration with the 'Centro de investigación en red de enfermedades respiratorias' of Madrid (in the framework of the European Marie Curie Network Π-net) was started to test some of the nanoparticles they synthesized for lung applications.

Among the tested nanocarriers, the *in vivo* multimodal study of the most promising ones will be briefly discussed here. These nanoparticles are based on albumin-coated upconverting nanophosphors [171] and present the unique feature of converting low energy near infrared light into higher visible light and/or near infrared emission. As a consequence, they allow to overcome some of the typical problems of fluorescent probes (auto-fluorescence, low penetration depth, high costs and toxicity).

The study, published in the Proceedings of International Society of Magnetic Resonance in Medicine in 2013 [172], showed that this new class of promising nanomaterials accumulates in healthy mice lungs after intravenous injection (SE≈35%), most probably due to the albumin-coating properties [173]. The results were confirmed by *ex vivo* fluorescence imaging and *in vivo* MRI, as shown in Figure 6.7. This study shows the feasibility of upconverting

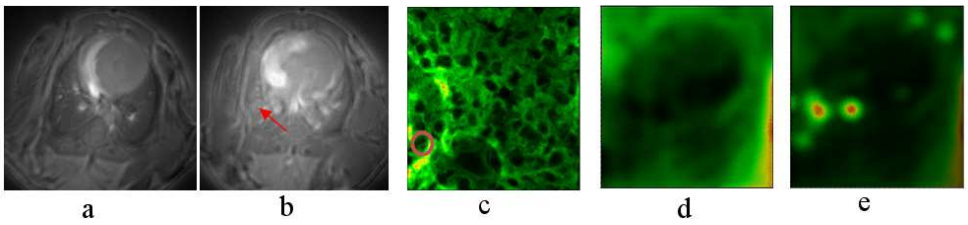

Figure 6.7: UTE MRI axial slice (a) before and (b) 33 min after the intravenous administration of the upconverting nanophosphors particles. The red arrow underlines the area of maximum SE of the lung. (c-e) Fluorescence images of the HES stained lung tissue with (c) large view of the alveolar structure (Filter 610/50 nm) and (d) zoom on the zone of interest (Filter 610/50 nm). (e) Fluorescence images of the upconverting nanophosphors particles (Filter 460/54) merged with (d). Reprinted from [172]

nanophosphors localization in the lung parenchyma using the UTE MRI protocols exploited in this thesis. The interested reader is referred to reference [172] for further details about the protocol and the description of possible applications of these nanoparticles.

6.5.2 Application to MEMRI

Among paramagnetic atoms, Mn is one of the most used (after Gd) in MRI. Manganese-enhanced MRI (MEMRI) has found several applications, especially in neuroscience [174]. As for gadolinium atoms, chelating forms of this element are often used to reduce toxicity issues. Mn toxicity has been indeed observed in relation with overexposure to this metal, particularly in brain regions where it can result in neurodegenerative pathologies and in heart [174–176].

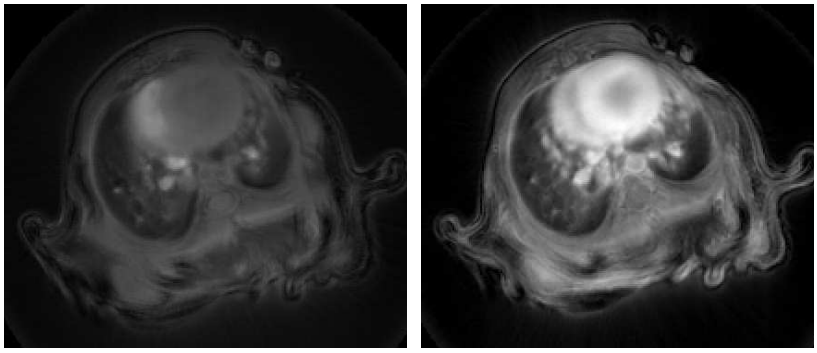

(a) Before contrast agent (b) Intravenous administration

Figure 6.8: UTE MR images (a) before and after the (b) intravenous administration of 150μL 20mM $MnCl_2$. The detection of the Mn compound is a proof-of-concept that shows the applicability of the protocols developed in this thesis for the efficient detection of a generic contrast agent. The intratracheal administration will be soon tested to investigate if similar results can be achieved with much lower concentrations, reducing the toxicological effects concerns. The experiment has been performed on a 7 T scanner for technical issues. Higher SEs are expected when the experiments will be performed on a 4.7 T spectrometer.

Compared with gadolinium chelates, Mn^{2+} is characterized by a small HD and high water solubility. As shown by Gobbo *et al.* [177], these properties make this metal ion attractive for aerosolized administration to the lungs since significant lung tissue enhancements can be obtained using low concentration solutions of $MnCl_2$ (1 mM). Considering that the main health concern associated with the use of manganese is the chronic exposure to excessive levels of this metal (>100 μM in primary astrocyte culture) [175], the possibility of using very low concentrations of $MnCl_2$ for various applications to the lung is especially interesting. It has to be indeed underlined that this compound is commonly available and extremely cheap.

The protocols described in this thesis can be easily applied to MEMRI, either on $MnCl_2$ molecules or on Mn-based nanoparticles. Preliminary proof-of-concept tests have indeed shown the accumulation of $MnCl_2$ solutions in lung cancer after intravenous administration. As shown in Figure 6.8, a significant accumulation has been observed right after the administration of the compound. The next step of this study will consist in administering this molecular solution through the oral route in the same cancer model (with a protocol similar to the one exposed in chapter 5). The idea is to investigate if the detection of NSCLC can be obtained using this inexpensive compound at very low concentrations, as it is reasonable to suppose in the light of the results presented in reference [177] and in this thesis. The PK and elimination pathways will be investigated as well. Comparisons with intravenous admin-

istration of $MnCl_2$ solutions and with orally- or intravenously-administered Mn-based nanoparticles will be finally carried out.

7
Conclusion

Lung pathologies represent a social and economic burden worldwide, being among the leading causes of death and disability. In the race to diagnose these diseases in their early stages and to develop new effective treatments, imaging techniques play a role of paramount importance.

Gold-standard imaging techniques like X-rays or computed tomography are currently used in clinical practice along with nuclear medicine imaging techniques for the diagnostics and the follow-up of lung diseases. Nonetheless, the concerns about cumulative dose coming from ionizing radiation limit their use. As a consequence, potentially beneficial systematic screening procedures of the population and regular follow-ups of the patients are often critical.

In the last decades, magnetic resonance imaging has shown to be able to reach high resolution and excellent soft tissue contrast comparable or superior to gold-standard imaging techniques, without employing ionizing radiation. These undeniable advantages have made MRI the imaging technique of choice when dealing with a number of heart, liver and brain pathologies. Nonetheless, the intrinsic properties of lung have hindered the diffusion of MRI in the diagnostics and follow-up of lung diseases.

Several experimental pre-clinical and clinical techniques have been proposed in recent years to overcome these obstacles, with various outcomes. However, the high costs or the complicate protocols required by some of these techniques have retarded their diffusion in clinical practice. An effective link between pre-clinical and clinical studies requires indeed noninvasive techniques which can be translated from animal models to human subjects with minimal changes and at reasonable costs.

In this thesis, special attention was given to the implementation of simple, reproducible, fast, effective, easily-implementable and noninvasive protocols for the diagnostics of frequent lung pathologies. For this reason, radial ultra-

short echo time proton MRI sequences have been chosen for investigation.

Throughout this work, radial UTE proton MRI was shown to be an effective tool in the quantitative characterization of different experimental animal models of lung diseases like asthma and lung cancer. Its capability of providing images with submillimetric resolution and significant signal-to-noise ratio in the lung parenchyma have indeed permitted to detect small changes in bronchial walls and submillimetric lung carcinogenic formations. The developed protocols could be used, for instance, in pre-clinical drug delivery studies to assess the efficacy of selected lead compounds for the treatment of these diseases or of some of their hallmarks. In addition, such results were obtained while working with freely-breathing animals.

In general, the work presented in this thesis supports the bulk of evidence which suggests that free-breathing acquisition techniques in mice can be used in conjunction with radial UTE MRI sequences with limited impact on image sharpness, signal-to-noise ratio and spatial resolution. The advantages of the technique employed in the present study are multiple and straightforward. The exclusion of respiratory-gated techniques from MRI acquisitions responds to the increasing need of testing lead compounds and new therapies while keeping the animal in its physiological conditions and ensuring the non-interference of the imaging protocol with the physiopathology of the disease under investigation. In addition, the shorter acquisition times enabled by the non respiratory-synchronous acquisitions allow a significant increase in the throughput in animal studies and are expected to considerably improve the patient management workflow in clinical practice. Finally, the easier protocol achievable when respiration-synchronous techniques are not used permits to translate the techniques developed on animals in clinical studies with minimal changes.

The possibility of further increasing the sensitivity of UTE MRI with the synergic use of contrast agents was demonstrated in this thesis. Robust protocols for the quantitative investigation of the biodistribution and of the elimination pathways of paramagnetic contrast agents have been proposed, implemented and validated using multimodal imaging techniques. The possibility of studying signal changes in lung parenchyma after intratracheal administration of contrast media has been widely studied thanks to the strong T_1 weighting of the chosen sequences. The negligible T_2^* effect of the paramagnetic contrast medium under identified conditions has allowed to implement quantitative pharmacokinetic models. A number of applications of this proto-

col have been discussed and are currently under experimentation. In addition, a protocol for the quantification of the absolute concentration of a generic paramagnetic contrast agent with MRI has been proposed. Pending on the validation of these results, many interesting applications of the proposed protocol can be envisaged, in the field of lung imaging as well as in other organs.

The use of ultra-small gadolinium-based multimodal nanoparticles has been shown to be especially promising. Their favourable pharmacokinetics, their biodistribution and the possibility of functionalizing these nanoassemblies on a as-needed basis make them an extremely flexible tool for several applications. The direct administration of these nanoassemblies via the airways has indeed shown to be very promising in the noninvasive detection of lung cancer. Pending on the confirmation of negligible toxicity of these nanoparticles, translational applications may be envisaged.

In conclusion, the work presented in this thesis has demonstrated that radial ultra-short echo time proton MRI has several possible applications in the field of pre-clinical lung imaging, pathology diagnostics and noninvasive follow-up. The simplicity, the cost effectiveness, the robustness, the rapidity, and the good reproducibility of these imaging protocols make them excellent candidates for translational applications. The use of properly selected contrast agents may compensate for the limited sensitivity that this imaging technique may have when compared to other imaging modalities.

A

Patent

The work relative to the USRPs has been object of a patent deposition.

The invention emphasises the originality and the wealth of applications potentially arising from the use of the USRPs administered in animals or humans through the airways. In particular, the interest of these nanoassemblies administered *via* the oral route for the diagnostics and therapeutics of lung diseases (e.g., cancer and asthma) are presented.

Because of the innovative properties of the USRPs and the multiple potential applications of the oral administration protocol proposed in this thesis, the French Patent request FR 12 53438 was submitted on 13 April 2012, before the submission of the work described in section 4.1 (filed to *Magnetic Resonance in Medicine* on 23 April 2012). The International Patent request PCT/EP2013/057677 was submitted one year after and eventually published in October 2013 (International publication WO 2013/153197 (A1)).

The link where the Patent publication (in French) can be found is reported hereafter. The work is the result of the collaboration with the University Claude Bernard of Lyon and the University Joseph Fourier of Grenoble. In detail, the former was in charge of the chemical synthesis and characterization of the nanoassemblies whereas the latter was responsible for the therapeutic studies. These subjects have been treated marginally in the body of this thesis work. On the other hand, the MRI and multimodal imaging applications of the intratracheally-administered USRPs described in the patent have been widely demonstrated or discussed in the previous chapters.

The interested reader can find the entire Patent publication at the following webpage:
http://worldwide.espacenet.com/publicationDetails/biblio?FT=D&date=20131017&DB=EPODOC&locale=en_EP&CC=WO&NR=2013153197A1&KC=A1&ND=4

(12) DEMANDE INTERNATIONALE PUBLIÉE EN VERTU DU TRAITÉ DE COOPÉRATION EN MATIÈRE DE BREVETS (PCT)

(19) Organisation Mondiale de la Propriété Intellectuelle
Bureau international

(43) Date de la publication internationale
17 octobre 2013 (17.10.2013)

WIPO | PCT

(10) Numéro de publication internationale
WO 2013/153197 A1

(51) Classification internationale des brevets :
A61K 47/48 (2006.01) *A61K 49/18* (2006.01)
A61K 49/00 (2006.01) *A61K 51/12* (2006.01)
A61K 49/10 (2006.01)

(21) Numéro de la demande internationale :
PCT/EP2013/057677

(22) Date de dépôt international :
12 avril 2013 (12.04.2013)

(25) Langue de dépôt : français

(26) Langue de publication : français

(30) Données relatives à la priorité :
12 53438 13 avril 2012 (13.04.2012) FR

(71) Déposants : **UNIVERSITE CLAUDE BERNARD LYON I** [FR/FR]; 43 Boulevard du 11 Novembre 1918, F-69622 Villeurbanne Cedex (FR). **NANO-H** [FR/FR]; 2 Place de l'Europe, Bâtiment A Parc d'activités GVIO, F-38070 Saint-Quentin-Fallavier (FR). **CENTRE NATIONAL DE LA RECHERCHE SCIENTIFIQUE - CNRS** [FR/FR]; 3 rue Michel Ange, F-75794 Paris Cedex 16 (FR). **UNIVERSITE JOSEPH FOURIER** [FR/FR]; Domaine Universitaire Saint Martin d'Hères, F-38041 Grenoble (FR).

(72) Inventeurs : **CREMILLIEUX, Yannick**; 8 rue Jérôme Mauvigney, F-33200 Bordeaux (FR). **BIANCHI, Andrea**; 3 rue Maurice Lanoire, F-33000 Bordeaux (FR). **DUFORT, Sandrine**; 23 rue Lorenzaccio, F-38100 Grenoble (FR). **COLL, Jean-Luc**; 6 rue Canal du Drac, F-38800 Le Pont de Claix (FR). **LUX, François**; 272 Cours Lafayette, F-69003 Lyon (FR). **TILLEMENT, Olivier**; 305 rue des Fours, F-69270 Fontaines Saint Martin (FR).

(74) Mandataire : **BOURGAREL, Denis**; Cabinet Plasseraud, 235 cours Lafayette, F-69006 Lyon (FR).

(81) États désignés *(sauf indication contraire, pour tout titre de protection nationale disponible)* : AE, AG, AL, AM, AO, AT, AU, AZ, BA, BB, BG, BH, BN, BR, BW, BY, BZ, CA, CH, CL, CN, CO, CR, CU, CZ, DE, DK, DM, DO, DZ, EC, EE, EG, ES, FI, GB, GD, GE, GH, GM, GT, HN, HR, HU, ID, IL, IN, IS, JP, KE, KG, KM, KN, KP, KR, KZ, LA, LC, LK, LR, LS, LT, LU, LY, MA, MD, ME, MG, MK, MN, MW, MX, MY, MZ, NA, NG, NI, NO, NZ, OM, PA, PE, PG, PH, PL, PT, QA, RO, RS, RU, RW, SC, SD, SE, SG, SK, SL, SM, ST, SV, SY, TH, TJ, TM, TN, TR, TT, TZ, UA, UG, US, UZ, VC, VN, ZA, ZM, ZW.

(84) États désignés *(sauf indication contraire, pour tout titre de protection régionale disponible)* : ARIPO (BW, GH, GM, KE, LR, LS, MW, MZ, NA, RW, SD, SL, SZ, TZ, UG, ZM, ZW), eurasien (AM, AZ, BY, KG, KZ, RU, TJ, TM), européen (AL, AT, BE, BG, CH, CY, CZ, DE, DK, EE, ES, FI, FR, GB, GR, HR, HU, IE, IS, IT, LT, LU, LV, MC, MK, MT, NL, NO, PL, PT, RO, RS, SE, SI, SK, SM, TR), OAPI (BF, BJ, CF, CG, CI, CM, GA, GN, GQ, GW, ML, MR, NE, SN, TD, TG).

Publiée :

— *avec rapport de recherche internationale (Art. 21(3))*

WO 2013/153197 A1

(54) Title : ULTRAFINE NANOPARTICLES AS MULTIMODAL CONTRAST AGENT

(54) Titre : NANOPARTICULES ULTRAFINES COMME AGENT DE CONTRASTE MULTIMODAL

(57) Abstract : The invention relates to a novel use of ultrafine nanoparticles, which are of use as a diagnostic, therapeutic or theranostic agent, characterized by the mode of administration thereof via the airways. The invention is also directed towards the uses which follow from this new mode of administration, in particular for imaging the lungs, and the diagnosis or prognosis of lung diseases. In the therapeutic field, the uses envisaged are those of radiosensitizing or radioactive agents for radiotherapy (and optionally curietherapy), for neutron therapy, and of agents for PDT (photodynamic therapy), in particular for treating lung tumours.

(57) Abrégé : L'invention concerne une nouvelle utilisation de nanoparticules ultrafines, utiles comme agent diagnostic, thérapeutique ou théranostic, caractérisée par leur mode d'administration par les voies aériennes. L'invention vise également les applications découlant de ce nouveau mode d'administration, notamment pour l'imagerie des poumons, et le diagnostic ou pronostic des pathologies pulmonaires. Dans le domaine thérapeutique, les applications envisagées sont celles d'agents radio-sensibilisants ou radioactifs pour la radiothérapie (et éventuellement la curiethérapie), pour la neutronthérapie, d'agents pour la PDT (photodynamic therapy), notamment pour le traitement des tumeurs du poumon.

B

Lung tumor treatment with USRPs

In this thesis (see chapter 5), it was clearly shown that USRPs can be efficiently used to improve the sensitivity of the UTE MRI for early cancer detection. The accumulation of the nanoparticles after intravenous or intratracheal administration was proved using MRI, BLI, 2D FRI, and conventional histological analysis.

In the following manuscript, the same result was confirmed by means of 3D FRI, *ex vivo* BLI, and *ex vivo* FRI. Such measurements were performed by the University of Grenoble but were partially repeated and confirmed at the University of Bordeaux, in the framework of this thesis. These data strengthen the observations made in chapters 5 and 6. At the same time, part of the MRI data presented in chapter 5 has contributed to the results presented in the following article.

In addition, the negligibility of the inflammation induced by intrapulmonary administration of the nanoparticles is proved here by means of a transgenic mouse model. The results clearly confirm the conclusions expressed in section 4.2 and chapter 6.

Finally, in the following manuscript, the radiosensitizing properties of the USRPs are discussed, and their therapeutic potential when combined with conventional X-rays is shown. This part of the work was carried out by the collaborators of the University of Grenoble and is reported here for sake of completeness.

The work presented hereafter has been submitted to *Small* and it is currently under review. Its copyright belongs to the authors listed in the title page of the manuscript.

Nebulized Gadolinium-Based Nanoparticles: a Theranostic Approach for Lung Tumor Imaging and Radiosensitization

Sandrine Dufort[1,2,3], Andrea Bianchi[4], Maxime Henry[1,2], François Lux[5], Géraldine Le Duc[6], Véronique Josserand[1,2], Cédric Louis[3], Pascal Perriat[7], Yannick Crémillieux[4], Olivier Tillement[5], Jean-Luc Coll[1,2 *].

[1] INSERM U823, Institut Albert Bonniot, 38706 Grenoble cedex, France
[2] Université Joseph Fourier, Institut Albert Bonniot, 38706 Grenoble cedex, France
[3] Nano-H S.A.S., 2 place de l'Europe, 38070 Saint Quentin – Fallavier, France
[4] Centre de Résonance Magnétique des Systèmes Biologiques, UMR 5536 CNRS, Université Bordeaux Segalen, 146 rue Léo Saignat, 33076 Bordeaux, France
[5] Institut Lumière Matière, UMR 5306 CNRS, Université Lyon 1-CNRS, Université de Lyon, 69622 Villeurbanne cedex, France
[6] Biomedical Beamline, European Synchrotron Radiation Facility, 6 rue Jules Horowitz, 38043 Grenoble cedex, France
[7] Matériaux Ingénierie et Science, INSA Lyon, UMR 5510 CNRS, Université de Lyon, 69621 Villeurbanne cedex, France

*** Corresponding Author**

Dr Jean-Luc Coll
INSERM U823, Equipe 5
Institut Albert Bonniot BP170
38 042 Grenoble cedex 9, France
Phone: 33[0]4 76 54 95 53/fax: 33[0]476 54 94 13
Email: Jean-luc.coll@ujf-grenoble.fr

Keywords
Lung cancer
Theranostic nanoparticles
Intrapulmonary administration
Multimodal imaging
Radiosensitization

Author Contributions

All authors contributed to the writing of the manuscript and have approved the final version.

Abstract

Lung cancer is the most common and death-related cancer worldwide. Thus, improving early diagnosis and therapy is necessary. Previously, we developed gadolinium-based Ultra-Small Rigid Platforms (USRPs) that can serve as multimodal imaging probes and as radiosensitizing agents. In addition, we recently demonstrated that USRPs can be detected in the lungs using Ultrashort echo-time Magnetic Resonance Imaging (UTE-MRI) and fluorescence imaging after intrapulmonary administration in healthy animals. The goal of the present study was to evaluate their theranostic properties in mice with bioluminescent orthotopic lung cancer, after intrapulmonary nebulization or conventional intravenous administration. We found that lung tumors can be detected non-invasively using fluorescence tomography or UTE-MRI after nebulization of USRPs, and this was confirmed by histological analysis of the lung sections. The deposition of USRPs around the tumor nodules was sufficient to generate a radiosensitizing effect when the mice were submitted to a single dose of 10 Gy conventional radiation one day after inhalation (mean survival time of 112 days versus 77 days for irradiated mice without USRPs treatment). No apparent systemic toxicity or induction of inflammation was observed. These results demonstrate the theranostic properties of USRPs for the multimodal detection of lung tumors and improved radiotherapy after nebulization.

Lung cancer (including both Non-Small Cell Lung Cancer (NSCLC) and Small Cell Lung Cancer (SCLC)) is a major health problem and is the leading cause of cancer-related adult deaths worldwide.[1] Despite current technological and medical advances, the majority of patients are diagnosed with locally advanced or metastatic disease, that is inoperable in most cases.[1, 2] In these instances, concomitant chemo-radiation therapy remains the most effective therapy [3] but the 5-year survival rate is only 15%.[4]

The reasons for therapeutic failure are diverse and are partially due to the inability to achieve adequate concentrations of drugs at the tumor site after systemic administration.[5] To increase exposure of the tumor to therapeutic agents while minimizing systemic side-effects, regional chemotherapy is a promising method and has already been successfully applied for the treatment of ovarian [6], brain [7] and bladder tumors [8] and liver metastasis.[9]

Inhalation of anti-tumor agents may be an alternative administration route to improve lung cancer outcomes. Indeed, the lungs present a large surface area for drug absorption and an extensive vasculature with a weak anatomical barrier that does not limit access to the body.[10, 11] The first trial, performed by Shevchanko and Resnik in 1968, established the feasibility and the efficacy of administering chemotherapy by inhalation in combination with radiotherapy.[12] Since then, a large number of drugs have been investigated for intrapulmonary administration in animal models and in human trials. [11, 13-15] In recent years, the pulmonary administration of nanoparticles has become an attractive strategy for the local delivery of therapeutic or diagnostic compounds [16]; however, to the best of our knowledge, only one work discusses the pulmonary administration of iodinated nanoparticles for diagnostic purposes. [17] This exemplifies the necessity of additional studies on this topic.

On the other hand, radiotherapeutic failure can be attributed to the resistance of tumors located in the lung, a highly radio-sensitive organ. This intrinsic property of the lung prevents the use of elevated doses of radiation during radiotherapy because of the resulting major side

effects. The local deposition of nanoparticles containing high Z-elements, such as gold, platinum or gadolinium, on the tumor site could enhance the effects of X-rays.[18-21] This should maximize the radiotherapeutic efficacy *via* the increase of toxicity on the tumor tissues and result in only minor side effects in normal tissues.

In this context, we developed "theranostic" Ultra-Small Rigid Particles, USRPs, obtained *via* an original top-down process. These particles are composed of a polysiloxane matrix and chelating species, e.g., DOTA (1,4,7,10-tetraazacyclododecane-1,4,7,10-tetraacetic acid), which is covalently grafted on the inorganic surface. In previous studies, the particles were validated as promising multimodal contrast agents for complementary imaging techniques, i.e., Magnetic Resonance Imaging (MRI), Single-Photon Emission Computed Tomography (SPECT), Computed Tomography (CT) and fluorescence imaging. [22] Despite rapid blood and renal clearance due to their small size (<6 nm),[23] the significant accumulation of these multifunctional particles in tumors occurs after intravenous injection, as a result of a passive targeting mechanism related to the Enhanced Permeability and Retention (EPR) effect [24] and of a specific active tumor-targeting mechanism after the grafting of cRGD peptides on their surface.[25] Finally, these gadolinium-based nanoparticles exhibited high radiosensitizing properties *in vitro* and *in vivo*.[21, 26]

In a recent study, the biodistribution and pharmacokinetics of USRPs were investigated by Ultrashort echo-time MRI (UTE-MRI) and fluorescence imaging after intrapulmonary administration in healthy mice.[27] The two imaging techniques showed similar kinetics for USRPs, with the occurrence of renal clearance after rapid passage from the airways to the bloodstream (elimination time of 187 ± 40 minutes).

We undertook the present study to evaluate deep lung tumor detection by fluorescence imaging and MRI *in vivo* and the radiosensitizing effect of USRPs administered directly in the airways of mice bearing orthotopic human lung tumors (H358-Luc). We also evaluated the

potential inflammation induced by intrapulmonary administration of the nanoparticles in a NF-κB-RE-Luc transgenic mouse model.

Results and Discussion

In vivo lung tumor detection

An orthotopic mouse model of human NSCLC was developed. Orthotopic models take into account the microenvironment of tumors. Thus, they are more relevant than the widely used subcutaneous xenografts to evaluate the diagnostic and/or therapeutic properties of novel agents.[29] In this model, lung tumors develop after the intrapulmonary inoculation of luciferase-modified human NSCLC H358 cells (H358-Luc cells). The use of bioluminescence *in vivo* is convenient for the non-invasive monitoring of the implantation and growth of these orthotopic tumors over five weeks.[30] At this time point, tumors are well-developed with a strong bioluminescent signal, but this is before the appearance of obvious symptoms (e.g., body weight loss and breathing difficulties). Mice bearing H358-Luc lung tumors can thus be used for subsequent imaging and/or therapy studies before the lung tumors induce breathing distress that could interfere with their health.

The ability of USRPs labeled with Cyanine 5.5 (USRPs-Cy5.5) to improve the *in vivo* detection of lung tumors was first evaluated after intrapulmonary or intravenous administration of equal quantities of nanoparticles using 3D-fluorescence tomography imaging. This was performed at multiple time points after intrapulmonary administration of 50 μL of a solution containing ~ 40 mmol/L [Gd^{3+}] or after intravenous injection of 200 μL of ~ 10 mmol/L [Gd^{3+}]. Representative images are shown in Figure 1A.

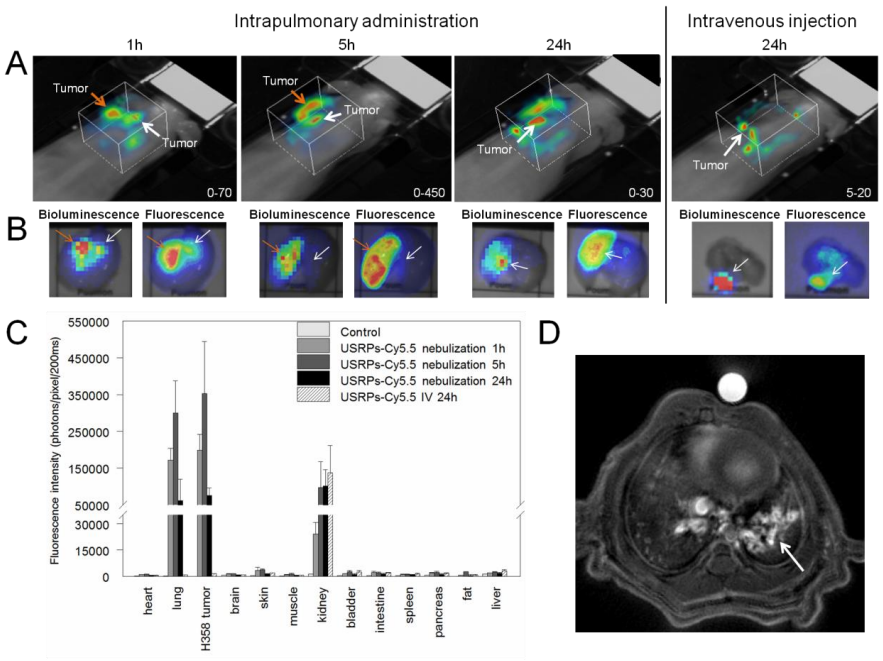

Figure 1: *In vivo* H358-Luc orthotopic lung tumors imaging.

(A) *In vivo* fluorescence tomography imaging after intrapulmonary or intravenous injection of USRPs-Cy5.5 (50 µL at $[Gd^{3+}]$ ~ 40 mM, n=3). (B) Bioluminescence and fluorescence imaging were then performed on isolated lungs, and showed a colocalization between the H358-Luc tumors (bioluminescence) and the fluorescent nanoparticles (fluorescence) (arrows). (C) Biodistribution of the fluorescent nanoparticles at different time points after intrapulmonary administration or 24h after intravenous injection, was evaluated by defining ROIs on fluorescent images of extracted organs. (D) USRPs also permitted the detection of lung tumors by MRI after intrapulmonary instillation (50 µL at $[Gd^{3+}]$ ~ 50 mM).

At the end of the experiment, the mice were euthanized, and the extracted organs were subjected to *ex vivo* bioluminescence and fluorescence imaging (Figure 1B) for semi-quantification (Figure 1C). In both cases, *in vivo* and *ex vivo*, bioluminescence or fluorescence

imaging showed similar profiles. USRPs-Cy5.5 were homogeneously distributed into the lungs immediately after intrapulmonary administration. Highly fluorescent spots could be observed on both the 3D-fluorescence images and *ex vivo* fluorescence images of the lungs. These high-intensity zones corresponded to the tumor nodules, as established by bioluminescence imaging (arrows on Figure 1A and 1B). This was associated with the augmented, but not significantly different, uptake of USRPs-Cy5.5 in lungs bearing tumors compared to "normal" lungs. Regarding intravenous injection, USRPs-Cy5.5 were barely detectable in the tumor, with an augmented signal two times that of the normal lungs (P=0.0209). Nonetheless, at 24 hours, the fluorescent signal was 52-times lower in the tumors when the particles were injected intravenously compared to intrapulmonary administration of the same quantity of injected nanoparticles. Interestingly, the two different administration routes resulted in similar levels of non-specific accumulation of the fluorescent USRPs in all of the other organs assessed (especially in the spleen and in the liver) with a similar mode of elimination *via* the kidneys, thus showing agreement with our previous data.[22, 27] These results confirmed that direct administration *via* the airways can increase the amount of locally delivered molecules or nanoparticles in lung tumor models, which could be of great interest for the treatment of lung diseases.[5, 16, 31]

Moreover, the intrapulmonary administration of USRPs permitted the detection of lung tumors using the specific UTE-MRI sequence (Figure 1D). This result sustained and validated the multimodal properties of these nanoparticles [21, 22, 27] and their potential as multimodal contrast agents for the detection of lung tumors.

Lung distribution of USRPs-Cy5.5 after intrapulmonary administration

Fluorescence microscopy was then performed on frozen lung sections to obtain more precise information about the distribution of USRPs-Cy5.5 within the lung tissues after

intrapulmonary administration (Figure 2). A large proportion of instilled fluorescent nanoparticles was found in the alveoli 1 hour after administration, together with a delineation of the lung tumors. Similar patterns were still observable 5 hours and 24 hours after administration, although a decrease of the fluorescent signal in the alveoli was noted. This reduction of the fluorescent signal can most likely be attributed to the passage of the nanoparticles from the airways to the blood, owing to the small size of the nanoparticles (<6 nm),[23] as described in a previous study.[27] A very weak fluorescence signal was detected by fluorescence microscopy on lung sections obtained from mice intravenously injected with USRPs-Cy5.5.

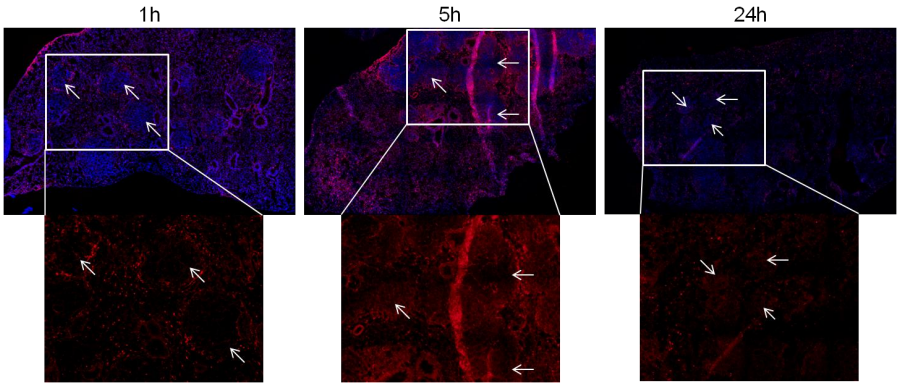

Figure 2: Distribution of fluorescent nanoparticles on the frozen lung sections of H358-Luc tumor-bearing mice at different time points after intrapulmonary administration of USRPs-Cy5.5 (50 µL of ~ 40 mM [Gd^{3+}]). Lung sections were observed by fluorescence microscopy (in blue: Hoechst staining of the nuclei; in red: Cy5.5 signals). The upper panel presents the superimposed images of the Hoechst and Cy5.5 signals. The bottom panel corresponds to Cy5.5-only signals. The Cy5.5 signal was primarily localized close to the tumor nodules (arrows).

Radiosensitizing therapeutic study

The significant and specific accumulation/retention of USRPs-Cy5.5 around the tumors in the nebulized lungs suggested that a radiosensitizing effect could be expected. H358-Luc lung tumor-bearing mice were therefore exposed to conventional irradiation of 10 Gy after intrapulmonary administration of USRPs (50 µL of ~ 20 mM [Gd^{3+}]). Prior to treatment, *in vivo* bioluminescence imaging was performed for all mice, and the bioluminescent signal in the lungs was quantified to randomize the mice into three homogenous groups: (i) a group of mice treated with irradiation after intrapulmonary administration of USRPs (n=11); (ii) a control group (n=6; no nanoparticle administration, no irradiation) and (iii) an irradiated-only group (n=11; no nanoparticle administration, irradiation) (Figure 3). The control and irradiated-only mice groups exhibited similar median survival times (MeST) of 83 days and 77 days (no significant difference; P=0.926). In contrast, the MeST was extended to 112 days in the group irradiated in the presence of USRPs. This corresponded to a 45% increase in lifespan (ILS) compared to the irradiated-only group (P=0.028). The improvement was attributed to the radiosensitizing properties of USRPs (containing high-Z gadolinium atoms), which were primarily present at the tumor level during irradiation, as shown by *in vivo* fluorescence imaging, UTE-MRI, and the analysis of the lung sections. This therapeutic protocol represents an attractive strategy for the treatment of lung tumors in radio-sensitive organs such as the lung.

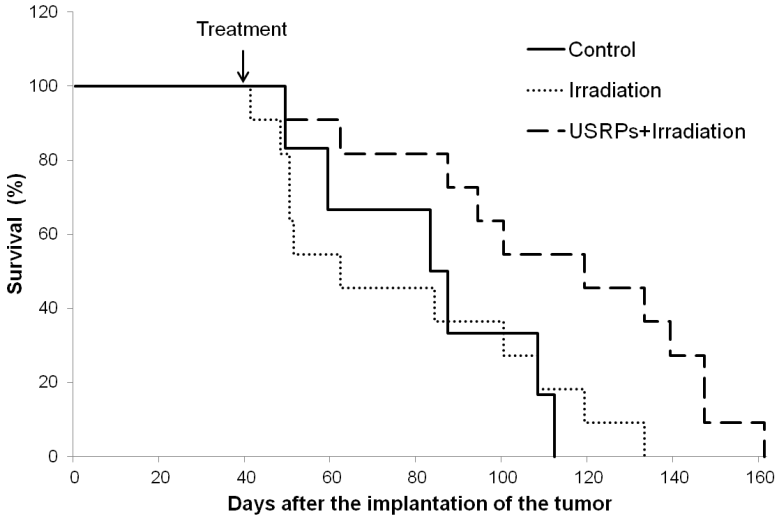

Figure 3: Survival curve comparison obtained on H358-Luc lung tumor-bearing mice without treatment (n=6), only treated by one irradiation (n=11), and treated by one irradiation (n=11) 24h after the intrapulmonary administration of nanoparticles, 161 days after tumor implantation. The irradiation was performed at 10 Gy, 37 days after tumor implantation.

These results have completed and continued the previous works in which it was initially demonstrated that despite rapid renal elimination after intravenous injection or intrapulmonary administration, USRPs can improve the effect of radiotherapy [21] independent of the location and type of tumor (subcutaneous, brain, etc.).

Pulmonary inflammatory potential of USRPs

Finally, demonstrating the safety of these nanoparticles after intrapulmonary administration was important. In particular, several publications have reported inflammation of the lungs and particle-induced activation of the redox-responsive NF-κB signaling pathway after *in vitro*

exposure [32-34] and after the inhalation or pulmonary delivery [35, 36] of nanoparticles. Therefore, the effect of USRPs nebulization in NF-κB-RE-Luc transgenic mice was investigated. We evaluated the potential induction of inflammation that depends on the NF-κB pathway in this strain of transgenic mice, 2, 5, 24, 48, 72 and 96 hours after the intrapulmonary administration of USRPs (50µL of ~ 20 mM [Gd^{3+}]) (Figure 4). Evaluation of the induced inflammation was performed using an *ex vivo* luciferase enzymatic activity assay on the protein extracts of all representative organs including the lungs, kidneys, spleen, liver and muscle (as a negative control) to generate highly sensitive and quantitative measurements. No significant variation was observed when the luciferase activities in the organs of the treated *versus* non-treated mice (control) were compared. Furthermore, no morphological changes and no edema were detected in the lungs of these mice. In contrast, animals that received an intrapulmonary administration of lipopolysaccharide (LPS, 2 mg/kg), which was used as a positive control for lung injury,[37] showed a 8-fold significant increase in luciferase activity in the lungs 24h after administration compared to the control. This observation are in agreement with the results of previous studies.[38, 39] These results are also consistent with the broncho-alveolar lavage analyses performed in a previous study [27] that showed no increase in the number of immune cells after intrapulmonary administration of USRPs.

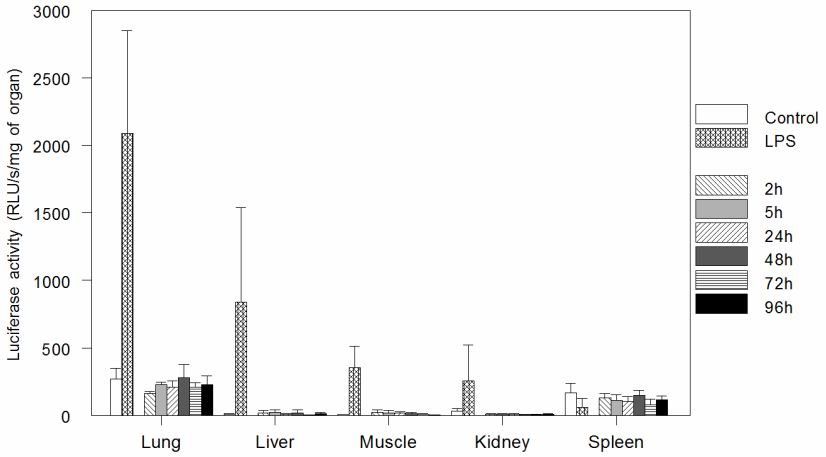

Figure 4: Evaluation of the inflammatory potential of USRPs after intrapulmonary administration. The luciferase enzymatic activity was quantified in organs of NF-κB-RE-Luc mice at different times after the intrapulmonary administration of USRPs (50 µL of ~ 20 mM [Gd^{3+}]) (n=5, means ± SD). As positive control, the mice received an intrapulmonary administration of lipopolysaccharide (LPS, 2 mg/kg) and were sacrificed at 24 h.

These results confirmed that the intrapulmonary nebulization of USRPs is a safe and efficient mode of administration of these nanoparticles to the lungs without inducing an inflammatory reaction. These findings corroborate the interest in the intrapulmonary administration modality, which presents several advantages compared to inhalation or intravenous injection for the monitoring of lung tumors.[40-42]

Conclusions

This study demonstrates the advantages of using gadolinium-based theranostic nanoparticles (USRPs) in an orthotopic lung cancer mouse model. USRPs enabled the multimodal detection, by fluorescence imaging and MRI, of lung tumors after both intravenous and

intrapulmonary administration. Their direct administration into the airways significantly increased their pulmonary delivery and uptake by the tumors, allowing improved detection of the tumor using imaging. In addition, the proposed protocol improved the use of conventional X-ray radiation due to the radiosensitizing properties of USRPs. Moreover, the intrapulmonary administration of nanoparticles did not induce inflammation. Based on these preclinical results, USRPs is anticipated to have potential applications as a simultaneous imaging and therapy modality for clinical lung cancer in the near future. The next step toward personalized therapy is the use of these nanoparticles for image-guided therapy.

Experimental Section

Nanoparticles synthesis and characterization

The Gd-DOTA-based nanoparticles (USRPs) were synthesized and characterized according to the previously described protocol.[22, 27, 28] To perform the fluorescence imaging, Cyanine 5.5 (Cy5.5) near infrared dye was covalently grafted on the nanoparticles (USRPs-Cy5.5), as described in reference 25.

Lung tumor animal model

Animal experiments were conducted in accordance with protocols approved by the Ethical Committee of Grenoble. H358-Luc cells (Optimal, Grenoble, France), cultured in RPMI medium supplemented with 10% of heat-inactivated fetal bovine serum, were harvested, washed and resuspended in 1X PBS at 10^7 cells/50 µL. Female NMRI *nude* mice (6 weeks old) were anesthetized with an intraperitoneal (i.p.) injection of Medetomidin (0.2 µg/g)/Ketamine (0.1 mg/g), and the tumor cells were inoculated in the lungs with a catheter after orotracheal intubation. The monitoring of tumor development was followed by *in vivo* bioluminescence imaging after the i.p. injection of 150 mg/kg of Luciferin (Promega,

Charbonnières, France), as previously described.[43] The quantification of bioluminescent signals allowed for the randomization of animals before each experiment. Lung tumors developed over a period of five weeks.

Intrapulmonary spray administration

Intrapulmonary administration was performed using a nebulizing IA-1C Microsprayer™ (Penn-Century, Inc., PA, USA) connected to a FMJ-250-high-pressure syringe (Penn-Century, Inc.) containing 50 µL of nanoparticles labeled with or without Cy5.5. After i.p. anesthesia with Medetomidin/Ketamine, the tip of the microsprayer was introduced into the trachea of the animals using adedicated laryngoscope.

Tumor imaging study

Bioluminescence, 2D- and 3D-fluorescence imaging, fluorescence quantifications (Optimal, Grenoble, France) and Ultrashort echo-time Magnetic Resonance Imaging (UTE-MRI) were performed as described in previous studies.[27, 44]

Fluorescence microscopy of the frozen lung sections (9 µm) was carried out using an AxioImager microscope with the AxioVision® software (Carl Zeiss, Jena, Germany) with a 10x objective. Nuclei were labeled by 1 µg/mL of Hoechst 33342 in 1X PBS for 5 min at room temperature.

Therapeutic efficacy study

Bioluminescence imaging was performed 35 days after tumor implantation, and animals were randomized into three groups: control (n=6), irradiation (n=11) and USRPs + irradiation (n=11). Irradiation consisted in a single 10 Gy dose delivered with a radiation source operating at 200 keV with a 2 mm Al-filter. Irradiation, restricted to the chest region, was

performed at day 37, 24 h after intrapulmonary administration of USRPs (50 µL of ~ 20 mM [Gd^{3+}]). The mice were followed at the animal facility after irradiation. At a later tumor stage, mice were euthanized when presenting clinical signs and/or 20% weight loss.

Pulmonary inflammatory potential of USRPs

At different time points (2, 5, 24, 48, 72 and 96 h) after the intrapulmonary administration of USRPs (50 µL of ~ 40 mM [Gd^{3+}]), NF-κB-RE-Luc mice (Taconic, USA) were sacrificed (n=5 for each time point), and the organs were collected and mashed for the *in vitro* luciferase enzymatic activity assay (Promega, Charbonnières, France), as previously described.[45]

The lipopolysaccharide (LPS) (Sigma-Aldrich, USA) was used as positive control. The mice were sacrificed 24 h after the intrapulmonary administration of LPS (2 mg/kg).

Statistical analyses

Statistical analyses were performed using the two-tail non-parametric Mann-Whitney t-test. All results are expressed as the means ± standard deviation. To compare survival among different treatment groups, the Kaplan-Meier survival data were plotted *versus* time after tumor implantation. These data were subsequently analyzed using a log-rank test. In both cases, statistical significance was considered when $P < 0.05$.

Acknowledgments

The authors acknowledge the funding support of the National Research Agency for the ANR project Gd-Lung (ANR-12-P2N-0009) and of INSERM. In addition, the authors are grateful to the team of the OPTIMAL Grenoble small animal optical imaging facility for their help and

technical assistance. A.B. acknowledges a fellowship from the European Network PINET (FP7-PEOPLE-2010-ITN-264864).

References

[1] A. Jemal, M. J. Thun, L. A. Ries, H. L. Howe, H. K. Weir, M. M. Center, E. Ward, X. C. Wu, C. Eheman, R. Anderson, U. A. Ajani, B. Kohler and B. K. Edwards, *J. Natl. Cancer Inst.* **2008**, *100*, 1672-1694.

[2] D. Morgensztern, S. H. Ng, F. Gao and R. Govindan, *J. Thorac. Oncol.* **2010**, *5*, 29-33.

[3] J. Jassem, *Radiother. Oncol.* **2007**, *83*, 203-213.

[4] K. M. Pisters, W. K. Evans, C. G. Azzoli, M. G. Kris, C. A. Smith, C. E. Desch, M. R. Somerfield, M. C. Brouwers, G. Darling, P. M. Ellis, L. E. Gaspar, H. I. Pass, D. R. Spigel, J. R. Strawn, Y. C. Ung and F. A. Shepherd, *J. Clin. Oncol.* **2007**, *25*, 5506-5518.

[5] F. Gagnadoux, J. Hureaux, L. Vecellio, T. Urban, A. Le Pape, I. Valo, J. Montharu, V. Leblond, M. Boisdron-Celle, S. Lerondel, C. Majoral, P. Diot, J. L. Racineux and E. Lemarie, *J. Aerosol Med. Pulm. Drug Deliv.* **2008**, *21*, 61-70.

[6] W. R. Robinson, C. Coberly, J. Beyer, A. Lewis and C. Ballard, *J. Oncol. Pract.* **2008**, *4*, 225-228.

[7] C. Guerin, A. Olivi, J. D. Weingart, H. C. Lawson and H. Brem, *Invest. New Drugs* **2004**, *22*, 27-37.

[8] M. Wirth, V. E. Plattner and F. Gabor, *Expert Opin. Drug Deliv.* **2009**, *6*, 727-744.

[9] N. E. Kemeny, D. Niedzwiecki, D. R. Hollis, H. J. Lenz, R. S. Warren, M. J. Naughton, J. C. Weeks, E. R. Sigurdson, J. E. Herndon, 2nd, C. Zhang and R. J. Mayer, *J. Clin. Oncol.* **2006**, *24*, 1395-1403.

[10] N. R. Labiris and M. B. Dolovich, *Br. J. Clin. Pharmacol.* **2003**, *56*, 588-599.

[11] P. Zarogoulidis, E. Chatzaki, K. Porpodis, K. Domvri, W. Hohenforst-Schmidt, E. P. Goldberg, N. Karamanos and K. Zarogoulidis, *Int. J. Nanomedicine* **2012**, *7*, 1551-1572.

[12] A. A. Shvedova, E. Kisin, A. R. Murray, V. J. Johnson, O. Gorelik, S. Arepalli, A. F. Hubbs, R. R. Mercer, P. Keohavong, N. Sussman, J. Jin, J. Yin, S. Stone, B. T. Chen, G. Deye, A. Maynard, V. Castranova, P. A. Baron and V. E. Kagan, *Am. J. Physiol. Lung Cell Mol. Physiol.* **2008**, *295*, L552-565.

[13] J. Hureaux, F. Lagarce, F. Gagnadoux, L. Vecellio, A. Clavreul, E. Roger, M. Kempf, J. L. Racineux, P. Diot, J. P. Benoit and T. Urban, *Eur. J. Pharm. Biopharm.* **2009**, *73*, 239-246.

[14] P. Chao, M. Deshmukh, H. L. Kutscher, D. Gao, S. S. Rajan, P. Hu, D. L. Laskin, S. Stein and P. J. Sinko, *Anticancer Drugs* **2010**, *21*, 65-76.

[15] G. A. Otterson, M. A. Villalona-Calero, W. Hicks, X. Pan, J. A. Ellerton, S. N. Gettinger and J. R. Murren, *Clin. Cancer Res.* **2010**, *16*, 2466-2473.

[16] S. Azarmi, W. H. Roa and R. Lobenberg, *Adv. Drug Deliv. Rev.* **2008**, *60*, 863-875.

[17] G. L. McIntire, E. R. Bacon, J. L. Toner, J. B. Cornacoff, P. E. Losco, K. J. Illig, K. J. Nikula, B. A. Muggenburg and L. Ketai, *J. Pharm. Sci.* **1998**, *87*, 1466-1470.

[18] J. F. Hainfeld, F. A. Dilmanian, D. N. Slatkin and H. M. Smilowitz, *J. Pharm. Pharmacol.* **2008**, *60*, 977-985.

[19] M. Y. Chang, A. L. Shiau, Y. H. Chen, C. J. Chang, H. H. Chen and C. L. Wu, *Cancer Sci.* **2008**, *99*, 1479-1484.

[20] E. Porcel, S. Liehn, H. Remita, N. Usami, K. Kobayashi, Y. Furusawa, C. Le Sech and S. Lacombe, *Nanotechnology* **2010**, *21*, 85103.

[21] G. Le Duc, I. Miladi, C. Alric, P. Mowat, E. Brauer-Krisch, A. Bouchet, E. Khalil, C. Billotey, M. Janier, F. Lux, T. Epicier, P. Perriat, S. Roux and O. Tillement, *ACS Nano* **2011**, *5*, 9566-9574.

[22] F. Lux, A. Mignot, P. Mowat, C. Louis, S. Dufort, C. Bernhard, F. Denat, F. Boschetti, C. Brunet, R. Antoine, P. Dugourd, S. Laurent, L. Vander Elst, R. Muller, L. Sancey, V. Josserand, J. L. Coll, V. Stupar, E. Barbier, C. Remy, A. Broisat, C. Ghezzi, G. Le Duc, S. Roux, P. Perriat and O. Tillement, *Angew. Chem. Int. Ed. Engl.* **2011**, *50*, 12299-12303.

[23] H. S. Choi, W. Liu, F. Liu, K. Nasr, P. Misra, M. G. Bawendi and J. V. Frangioni, *Nat. Nanotechnol.* **2010**, *5*, 42-47.

[24] Y. Matsumura and H. Maeda, *Cancer Res.* **1986**, *46*, 6387-6392.

[25] J. Morlieras, S. Dufort, L. Sancey, C. Truillet, A. Mignot, F. Rossetti, M. Dentamaro, S. Laurent, L. Vander Elst, R. N. Muller, R. Antoine, P. Dugourd, S. Roux, P. Perriat, F. Lux, J. L. Coll and O. Tillement, *Bioconjug. Chem.* **2013**, *24*, 1584-1597.

[26] P. Mowat, A. Mignot, W. Rima, F. Lux, O. Tillement, C. Roulin, M. Dutreix, D. Bechet, S. Huger, L. Humbert, M. Barberi-Heyob, M. T. Aloy, E. Armandy, C. Rodriguez-Lafrasse, G. Le Duc, S. Roux and P. Perriat, *J. Nanosci. Nanotechnol.* **2011**, *11*, 7833-7839.

[27] A. Bianchi, S. Dufort, F. Lux, A. Courtois, O. Tillement, J. L. Coll and Y. Cremillieux, *MAGMA* **2013**.

[28] A. Mignot, C. Truillet, F. Lux, L. Sancey, C. Louis, F. Denat, F. Boschetti, L. Bocher, A. Gloter, O. Stephan, R. Antoine, P. Dugourd, D. Luneau, G. Novitchi, L. C. Figueiredo, P. C. de Morais, L. Bonneviot, B. Albela, F. Ribot, L. Van Lokeren, I. Dechamps-Olivier, F. Chuburu, G. Lemercier, C. Villiers, P. N. Marche, G. Le Duc, S. Roux, O. Tillement and P. Perriat, *Chemistry* **2013**, *19*, 6122-6136.

[29] T. H. Kuo, T. Kubota, M. Watanabe, T. Furukawa, S. Kase, H. Tanino, Y. Saikawa, K. Ishibiki, M. Kitajima and R. M. Hoffman, *Anticancer Res.* **1993**, *13*, 627-630.

[30] R. A. Madero-Visbal, J. F. Colon, I. C. Hernandez, A. Limaye, J. Smith, C. M. Lee, P. A. Arlen, L. Herrera and C. H. Baker, *Surg. Oncol.* **2012**, *21*, 23-29.

[31] C. T. Badea, K. K. Athreya, G. Espinosa, D. Clark, A. P. Ghafoori, Y. Li, D. G. Kirsch, G. A. Johnson, A. Annapragada and K. B. Ghaghada, *PLoS One* **2012**, *7*, e34496.

[32] R. P. Nishanth, R. G. Jyotsna, J. J. Schlager, S. M. Hussain and P. Reddanna, *Nanotoxicology* **2011**, *5*, 502-516.

[33] I. Pujalte, I. Passagne, B. Brouillaud, M. Treguer, E. Durand, C. Ohayon-Courtes and B. L'Azou, *Part Fibre Toxicol.* **2011**, *8*, 10.

[34] S. G. Han, B. Newsome and B. Hennig, *Toxicology* **2013**, *306*, 1-8.

[35] I. T. Shevchenko and G. E. Resnik, *Neoplasma* **1968**, *15*, 419-426.

[36] W. S. Cho, R. Duffin, C. A. Poland, A. Duschl, G. J. Oostingh, W. Macnee, M. Bradley, I. L. Megson and K. Donaldson, *Nanotoxicology* **2012**, *6*, 22-35.

[37] S. Hadina, C. L. Wohlford-Lenane and P. S. Thorne, *Toxicology* **2012**, *291*, 133-138.

[38] T. Okamoto, K. Gohil, E. I. Finkelstein, P. Bove, T. Akaike and A. van der Vliet, *Am. J. Physiol. Lung Cell. Mol. Physiol.* **2004**, *286*, L198-209.

[39] Y. Duan, J. Learoyd, A. Y. Meliton, A. R. Leff and X. Zhu, *Respir Res* **2012**, *13*, 4.

[40] K. E. Driscoll, D. L. Costa, G. Hatch, R. Henderson, G. Oberdorster, H. Salem and R. B. Schlesinger, *Toxicol. Sci.* **2000**, *55*, 24-35.

[41] D. L. Costa, J. R. Lehmann, D. Winsett, J. Richards, A. D. Ledbetter and K. L. Dreher, *Toxicol. Sci.* **2006**, *91*, 237-246.

[42] S. A. Shoyele and S. Cawthorne, *Adv. Drug. Deliv. Rev.* **2006**, *58*, 1009-1029.

[43] M. Keramidas, V. Josserand, C. A. Righini, C. Wenk, C. Faure and J. L. Coll, *Br. J. Surg.* **2010**, *97*, 737-743.

[44] M. Keramidas, F. de Fraipont, A. Karageorgis, A. Moisan, V. Persoons, M. J. Richard, J. L. Coll and C. Rome, *Stem Cell Res. Ther.* **2013**, *4*, 41.

[45] M. Morille, C. Passirani, S. Dufort, G. Bastiat, B. Pitard, J. L. Coll and J. P. Benoit, *Biomaterials* **2011**, *32*, 2327-2333.

C

A review about USRPs

In this thesis, the NMR properties and pharmacokinetics of intratracheally administered USRPs have been studied in chapter 4 and a possible application of these nanoassemblies as diagnostic tools for lung cancer has been presented in chapter 5.

As anticipated in the patent request presented in appendix A and discussed in chapter 6, a large variety of applications may be implemented thanks to the advantages rising from the direct application of the USRPs to the airways. In appendix B, a possible therapeutic application coming from the radiosensitizing properties of intratracheally administered USRPs has been shown.

The negligible toxicity of these nanoparticles, their favourable pharmacokinetics, their diagnostic properties when combined with proper imaging techniques, and their potential therapeutic application after intratracheal administration have been partially described in this thesis. However, the USRPs have been applied to other heterotopic or orthotopic tumor models (i.e., gliosarcoma of the brain) as well.

In the work presented hereafter, a review of the theranostic properties of the USRPs investigated up to now is proposed. The work described in this thesis has contributed to the results presented in the following article.

The manuscript has been accepted for publication on *British Journal of Radiology* as an invited review paper (doi:10.1259/bjr.20140134).

Pages 160-194 have been removed from this *diffusion version* of the Ph.D. thesis since they contained an article protected by editor copyright. Only the abstract will be reported hereafter.

The removed article is:

The use of theranostic gadolinium-based nanoprobes to improve radiotherapy efficacy

L. Sancey, F. Lux, S. Kotb, S. Roux, S. Dufort,
A. Bianchi, Y. Crémillieux, *et al.*

The British Journal of Radiology, doi:10.1259/bjr.20140134, in press.

The full article can be downloaded at:

http://www.birpublications.org/doi/abs/10.1259/bjr.20140134

A copy of the *reference version* of this Ph.D. thesis can be accessed at the Library of the University of Bordeaux. For further details please contact the author of this work (bian.drea@libero.it).

The use of theranostic gadolinium-based nanoprobes to improve radiotherapy efficacy

L. Sancey, F. Lux, S. Kotb, S. Roux, S. Dufort,
A. Bianchi, Y. Crémillieux, *et al.*

Abstract:

A new efficient type of gadolinium-based theranostic agent (AGuIX) has recently been developed for magnetic resonance imaging (MRI)-guided radiotherapy. These new particles consist of a polysiloxane network surrounded by a number of gadolinium chelates, usually 10. Due to their small size (<5 nm), AGuIX typically exhibit biodistributions that are almost ideal for diagnostic and therapeutic purposes. For example, while a significant proportion of these particles accumulate in tumours, the remainder is rapidly eliminated by the renal route. In addition, these particles present no evidence of toxicity, in the absence of irradiation with up to 10 times the planned dose for clinical trials. AGuIX particles have been proven to act as efficient radiosensitizers in a large variety of experimental in vitro scenarios, including different radioresistant cell lines, irradiation energies, and radiation sources (sensitizing enhancement ratio ranging from 1.1 to 2.5). Preclinical studies have also demonstrated the impact of these particles on different heterotopic and orthotopic tumours, with both intra-tumoural or intravenous injection routes. A significant therapeutical effect has been observed in all contexts. Furthermore, MRI monitoring was proven to efficiently aid in determining a radiotherapy protocol and assessing tumour evolution following treatment. The usual theoretical models, based on energy attenuation and macroscopic dose enhancement, cannot account for all the results that have been obtained. Only theoretical models, which take into account the Auger electron cascades that occur between the different atoms constituting the particle and the related high radical concentrations in the vicinity of the particle, provide an explanation for the complex cell damage and death observed.

D

USRPs synthesis and characterization: Supplementary Material

In this appendix, the detailed description of the synthesis and characterization of the USRPs used in the works presented in sections 4.2 and 5 is proposed. The work presented hereafter has been carried out by the collaborators of the University of Lyon, co-authors in the manuscripts presented in the aforementioned sections. This information is reported here only for sake of completeness. The interested reader can find the description of the synthesis and characterization of the nanoparticles used in section 4.1 in reference [145] (slightly different from the one presented here).

Supplementary Material:

Nanoparticles synthesis and characterization

MATERIALS AND METHODS:

Chemicals:

Gadolinium chloride hexahydrate ([$GdCl_3.6H_2O$], 99%, Nano-H France), sodium hydroxide (NaOH, 99.99%, Sigma Aldrich), diethylene glycol (DEG, >99%, SDS), tetraethylorthosilicate ($Si(OC_2H_5)_4$, TEOS, 98%, Sigma Aldrich), (3-aminopropyl)triethoxysilane ($H_2N(CH_2)_3$-$Si(OC_2H_5)_3$, APTES, 99%, Sigma Aldrich), 1,4,7,10-tetraazacyclododecane-1-glutaric anhydride-4,7,10-triacetic acid (DOTAGA, CheMatech®), triethylamine (TEA, 99%, Sigma Aldrich), anhydrous dimethylsulfoxyde (DMSO, Sigma Aldrich), Pre-activated Cyanine 5.5(Cy5.5-NHS, GE Healthcare®).

Size measurements and surface potential:

Hydrodynamic diameters (HD) and ξ-potentials of our samples were determined with a ZetasizerNanoS PCS (Photon Correlation Spectroscopy, Laser He-Ne 633 nm) from Malvern Instruments®.

Fluorescence measurements:

Fluorescence measurements were carried out at room temperature using a Varian Carry Eclipse fluorescence spectrophotometer.

High Performance Liquid Chromatography:

Gradient HPLC analysis was carried out using the Shimadzu® Prominence series UFLC system equipped with a CBM-20a controller bus module, an LC-20AD liquid chromatograph, a CTO-20A column oven and SPD-20AUV-visible detector. Sample UV-visible absorption was measured at 295 nm. Sample aliquots of 20 µL were loaded in 95% solvent A – 5 % solvent B (A =Milli-Q water/TFA 99.9:0.1 v/v; B = CH3CN/Milli Q water/TFA 90:9.9:0.1 v/v/v) onto a Jupiter C4 column (150 x 4.60 mm, 5 µm, 300 Å, Phenomenex®) at a flow rate of 1 mL/min over 5 min. In a second step, samples were eluted by a gradient developed from 5 to 90 % of solvent B in solvent A over 30 min. The concentration of solvent B was maintained over 10 min. Then, the concentration of solvent B was decreased to 5 % over a period of 10 min to re-equilibrate the system, followed by additional 10 min at this final concentration. Before each sample measurement, a baseline was performed following the same conditions byloading Milli-Q water into the injection loop.

Nanoparticles synthesis:

The synthesis of the gadolinium based nanoparticles is a four step synthesis. The first step is the synthesis of a gadolinium oxide core by addition of soda on gadolinium chloride salts in DEG [a]. The second step is the growth of a polysiloxane shell by addition of adapted

amounts of TEOS and APTES in DEG. Then DOTAGA anhydride is covalently grafted on the free amino functions of APTES and during the transfer from DEG to water of the particles a top down process is observed with a dissolution of the gadolinium oxide core due to the chelation by DOTAGA. This lead to the ultrasmall gadolinium based nanoparticles made of a polysiloxane matrix surrounded by gadolinium chelates [b, c].

Preparation of gadolinium oxide cores:

Gadolinium chloride salt (167.3g, $GdCl_3.6H_2O$) was placed in 3 L of diethylene glycol (DEG) at room temperature under vigorous stirring. The suspension was heated at 140°C until the total dissolution of gadolinium chloride salt (about 1 h). When the solution is clear, sodium hydroxide solution (120 mL, 3.38 M) was added drop by drop under vigorous stirring. Afterwards, the solution was heated and stirred at 180°C for 3h. A transparent colloid of gadolinium oxide (Gd_2O_3) nanoparticles (HD = 1.6±0.5 nm) was obtained ([Gd] = 30 mM)and can be stored at room temperature for weeks without alteration.

Coating of gadolinium oxide cores by a polysiloxane shell:

The previously obtained Gd_2O_3colloidal solution is diluted in DEG to obtain a final volume of 4.5 L ([Gd] = 30 mM). The silane precursors (APTES (75.8 mL)) and TEOS (48 mL)) and hydrolysis solution (aqueous Et_3N in DEG (0.75M of TEA, 75M of water) are continuously added to the precedent solution over a four day period under stirring at 40°C (HD= 3.5±0.7 nm). After the end of the addition, the final mixture was stirred for 48H at 40°C (HD = 5.7±1.0 nm).

Functionalization of the polysiloxane shell by DOTAGA:

To perform the functionalization of the core-shell nanoparticles (core: Gd_2O_3/ shell: polysiloxane) DOTAGA anhydride (108.9 g diluted in 500 mL of anhydrous DEG) is added to 3.25 L of the precedent solution during a period of three days under stirring.

Purification and dissolution of the gadolinium oxidecore:

The precedent solution is precipitated in 14L of acetone before filtration and washing by 2x2L of acetone. A white powder is obtained that is dispersed in water and purified by tangential filtration to a 1000 factor over a 5 kDa membrane (HD = 4.1±1.0 nm at pH 7.4). The nanoparticles are then freeze-dried for storage, using a Christ Alpha 1-2 lyophilizer. The freeze dried nanoparticles are stable for months without alterations.

Grafting of Cy 5.5 near infrared dye:

To perform optical imaging, Cy 5.5 near infrared dye was grafted on the nanoparticles.Cy5.5-NHS was diluted in anhydrous DMSO (2.5 mg/L) and added to an aqueous solution of freshly dispersed USPRs in water at pH 7-7.4 for 8 hours under stirring (molar ratio Cy5.5/Gd 0.044/1). Nanoparticles were then submitted to tangential filtration to a 1000 factor over a 5 kDa membrane before freeze-drying.

RESULTS

The USRPs are synthesized by a previously described protocol [b, c] slightly modified to obtain higher quantities of nanoparticles. It consists first in the synthesis of gadolinium oxide core by addition of soda on gadolinium trichloride previously dissolved in DEG. Then the growth of a polysiloxane shell is ensured by the addition of adapted amount of silane precursors (TEOS and APTES). Nanoparticles presenting a HD of 5.7 ±1.0 nm are obtained at this step. DOTAGA anhydride is then covalently grafted on the free amino functions issued from APTES. During the transfer to water of these nanoparticles, an original top down process occurs: the gadolinium issued from the core is chelated by the DOTAGA and then a collapse and a fragmentation of the polysiloxane shell into ultrasmall nanoparticles, made of polysiloxane and surrounded by about ten DOTA chelates, is observed as previously described. When needed for optical imaging experiments, Cy 5.5 was grafted on the USRPs as described in the experimental section.

The nanoparticles present a HD of about 4.1 ± 1.0 nm. The particles have rather a neutral charge at physiological pH, namely a value of zeta potential of -0.2 mV at pH = 7.4. The number of free DOTAGA on the nanoparticles has been determined by adding increasing amounts of europium chloride and by evaluating the fluorescence of the chelated europium ions [c]. Less than 5% of free DOTAGA are present on the nanoparticles maximizing the relaxivity of each nanoparticle. The r_1 per nanoparticle is equal to 8.22 $mM^{-1}s^{-1}$ per gadolinium ion at 4.7T. Finally, the purity of the nanoparticles has been evaluated more than 95% by HPLC.

REFERENCES

a. Le Duc G, Miladi I, Alric C, Mowat P, Bräuer-Krisch E, Bouchet A, Khalil E, Billotey C, Janier M, Lux F, Epicier T, Perriat P, Roux S, Tillement O (2011) Toward an Image-Guided Microbeam Radiation Therapy Using Gadolinium-Based Nanoparticles. ACS Nano 5: 9566-9574.

b. Lux F, Mignot A, Mowat P, Louis C, Dufort S, Bernhard C, Denat F, Boschetti F, Brunet C, Antoine R, Dugourd P, Laurent S, Elst LV, Muller R, Sancey L, Josserand V, Coll J-L, Stupar V, Barbier E, Rémy C, Broisat A, Ghezzi C, Le Duc G, Roux S, Perriat P, Tillement O (2011) Ultrasmall Rigid Particles as Multimodal Probes for Medical Applications. Angew Chem 123: 12507-12511.

c. Mignot A, Truillet C, Lux F, Sancey L, Louis C, Denat F, Boschetti F, Bocher L, Gloter A, Stephan O, Antoine R, Dugourd P, Luneau D, Novitchi G, Figueiredo LC, De Morais PC, Bonneviot L, Albela B, Ribot F, Van Lokeren L, Dechamps-Olivier I, Chuburu F, Lemercier G, Villiers C, Marche PN, Le Duc G, Roux S, Tillement O, Perriat P (2013) A top-down synthesis route to ultrasmall multifunctional Gd-based nanoparticles for theranostic applications. Chem Eur J 19: 6122-6136.

Bibliography

[1] The top 10 causes of death. Fact sheet N. 310. World Health Organization (WHO) 2011 (Updated on July 2013); Available from: http://who.int/mediacentre/factsheets/fs310/en/index.html.

[2] Lipson DA, Van Beek EJR. Functional lung imaging. Boca Raton: Taylor & Francis Group, LLC; 2005. 635 p.

[3] Brenner DJ, Hall EJ. Computed tomography: an increasing source of radiation exposure. N Engl J Med 2007; 357:2277–2284.

[4] Beckmann N, Kneuer R, Gremlich H-U, Quintana HK, Blé F-X, Müller M. In vivo mouse imaging and spectroscopy in drug discovery. NMR Biomed 2007; 20:154–185.

[5] Biederer J, Beer M, Hirsch W, Wild J, Fabel M, Puderbach M, Van Beek EJR. MRI of the lung (2/3). Why... when... how? Insights Imaging 2012; 3:355–371.

[6] Wild JM, Marshall H, Bock M, Schad LR, Jakob PM, Puderbach M, et al. MRI of the lung (1/3): methods. Insights Imaging 2012; 3: 345-353.

[7] Beckmann N, Cannet C, Karmouty-Quintana H, Tigani B, Zurbruegg S, Blé F-X, et al. Lung MRI for experimental drug research. Eur J Rad 2007; 64:381–396.

[8] Wielpütz M, Kauczor H-U. MRI of the lung: state of the art. Diagn Interv Radiol 2012; 18:344–353.

[9] Cutillo AG. Application of magnetic resonance to the study of lung. New York: Futura Publishing Company, Inc.; 1996. 607 p.

[10] Bergin CJ, Pauly JM, Macovski A. Lung parenchyma: projection reconstruction MR imaging. Radiology 1991; 179:777–781.

[11] Bergin CJ, Noll DC, Pauly JM, Glover GH, Macovski A. MRI imaging of lung parenchyma: a solution to susceptibility. Radiology 1992; 183:673–676.

[12] Glover GH, Pauly JM. Projection reconstruction techniques for reduction of motion effects in MRI. Magn Reson Med 1992; 28:275–289.

[13] Zurek M, Bessaad A, Cieslar K, Crémillieux Y. Validation of simple and robust protocols for high-resolution lung proton MRI in mice. Magn Reson Med 2010; 64:401–407.

[14] Zurek M, Crémillieux Y. MRI of the lung: non-invasive protocols and applications to small animal models of lung disease. Methods Mol Biol 2011; 771:459-474.

[15] West JB. Respiratory physiology: the essentials. Baltimore: Lippincott Williams & Wilkins; 2011. 208 p.

[16] Wallau BR, Schmitz A, Perry SF. Lung morphology in rodents (Mammalia, Rodentia) and its implications for systematics. J Morphol 2000; 246:228-248.

[17] Lindstedt SL, Schaeffer PJ. Use of allometry in predicting anatomical and physiological parameters of mammals. Lab Animal 2002; 36:1-19.

[18] Valerius K-P. Size-dependent morphology of the conductive bronchial tree in four species of myomorph rodents. J Morphol 1996; 230:291-297.

[19] Fraser RS. Histology and gross anatomy of the respiratory tract. In: Hamid Q, Martin J, Shannon J, editors. Physiological Basis of Respiratory Disease. Hamilton, Ontario: BC Decker Inc; 2005. pp. 1-14.

[20] Netter FH, Kaminsky D. The Netter collection of medical illustrations. Vol.3: the respiratory system. Philadelphia: W.B. Saunders; 2011. 344 p.

[21] Albertine KH, Williams MC, Hyde DM. Anatomy and development of the respiratory tract. In: Murray JF, Nadel JA, Mason RJ, Boushey HA, editors. Textbook of respiratory medicine. Philadelphia: W.B. Saunders; 2000. pp. 3-33.

[22] Caceci T. VM8054: Veterinary Histology. Virginia-Maryland regional college of veterinary medicine website. http://www.vetmed.vt.edu/education/curriculum/vm8054/Labs/Lab25/lab25.htm. Version 5.2, updated on August 2008.

[23] Lindsay DT. Functional human anatomy. Dubuque, Iowa: William C Brown Pub; 1995. 976 p.

[24] Nicod LP. Lung defences: an overview. Eur Respir Rev 2005; 14, 95:45-50

[25] Chitko-McKnown CG, Blecha F. Pulmonary intravascular macrophages: a review of immune properties and functions. Ann Rech Vet 1992; 23:201-214.

[26] Kittel B., Ruehl-Fehlert C., Morawietz, Klapwijk J, Elwell MR, Lenz B, et al. Revised guides for organ sampling and trimming in rats and mice - Part 2. Exp Toxic Pathol 2004; 55:413-431.

[27] Irvin CG, Bates HT. Measuring the lung function in the mouse: the challenge of size. Respir Res 2003; 4:4.

[28] Schulz H, Johner C, G. Eder, Ziesenis A, Reitmeier P, Heyder J, et al. Respiratory mechanics in mice: strain and sex specific differences. Acta Physiol Scand 2002; 174:367-375.

[29] Thiesse J, Namati E, Sieren JC, Smith AR, Reinhardt JM, Hoffman EA, et al. Lung structure phenotype variation in inbred mouse strains revealed through in vivo micro-CT imaging. J Appl Physiol 2010; 109:1960-1968.

[30] Soutiere SE, Tankersley CG, Mitzner W. Differences in alveolar size in inbred mouse strains. Resp Physiol Neurobi 2004; 140:283-291.

[31] West JB. Pulmonary pathophysiology: the essentials. Baltimore: Lippincott Williams & Wilkins; 2013. 183 p.

[32] International statistical classification of diseases and related health problems, 10th revision (ICD-10). World Health Organization (WHO) 2012; Available from: http://apps.who.int/classifications/icd10/browse/2010/en#/X

[33] Busse WW, Lemanske RF. Asthma. N Engl J Med 2001; 344:350-362.

[34] Global strategy for asthma menagement and prevention. Global Initiative for Asthma (GINA) 2012; Available from: http://www.ginasthma.org.

[35] Ozier A, Allard B, Bara I, Girodet P-O, Trian T, Marthan R, et al. The Pivotal Role of Airway Smooth Muscle in Asthma Pathophysiology. J Allergy 2011; 2011:1-20.

[36] Barnes PJ. New drugs for asthma. Nat Rev Drug Discov 2004; 3:831-44.

[37] Bousquet J, Jeffery PK, Busse WW, Johnson M, Vignola AM. Asthma. From Bronchoconstriction to Airways Inflammation and Remodeling. Am J Respir Crit Care Med 2000; 161:1720-1745.

[38] McParland BE, Macklem PT, Paré PD. Airway wall remodeling: friend or foe? J Appl Physiol 2003; 95:426-434.

[39] Bara I, Ozier A, Tunon de Lara JM, Marthan R, Berger P. Pathophysiology of bronchial smooth muscle remodelling in asthma. Eur Respir J 2010; 36:1174–1184.

[40] Dunnill MS, Massarella GR, Anderson JA. A comparison of the quantitative anatomy of the bronchi in normal subjects, in status asthmaticus, in chronic bronchitis, and in emphysema. Thorax. 1969; 24:176–17.

[41] Carroll NG, Cooke C, James AL. Bronchial blood vessel dimensions in asthma. Am J Respir Crit Care Med 1997; 155:689–695.

[42] Carroll N, Elliot J, Morton A, James A. The structure of large and small airways in nonfatal and fatal asthma. Am Rev Respir Dis 1993; 147:405–41.

[43] Laitinen LA, Heino M, Laitinen A, Kava T, Haahtela T. Damage of the airway epithelium and bronchial reactivity in patients with asthma. Am Rev Respir Dis 1986; 131:599–606.

[44] Girodet P-O, Ozier A, Bara I, Tunon de Lara JM, Marthan R, Berger P. Airway remodeling in asthma: new mechanisms and potential for pharmacological intervention. Pharmacol Therapeut 2011; 130:325-337.

[45] Herbst RS, Heymach JV, Lippman SM. Lung cancer. N Engl J Med 2008; 359:1367-1380.

[46] Parkin M, Tyczynski JE, Boffetta P, Samet J, Shields P, Caporaso N. Lung cancer epidemiology and etiology. In: Travis WD, Brambilla E, Müller-Hermelink HK, Harris CC, editors. Pathology and Genetics of Tumours of the Lung, Pleura, Thymus and Heart. Geneva: WHO Press; 2004. pp. 12–15.

[47] Molina JR, Yang P, Cassivi SD, Schild SE, Adjei AA. Non-small cell lung cancer: Epidemiology, risk factors, treatment, and survivorship. Mayo Clin Proc 2008; 83:584–94.

[48] Ferlay J, Soerjomataram I, Ervik M, Dikshit R, Eser S, Mathers C, et al. GLOBOCAN 2012 v1.0, Cancer Incidence and Mortality Worldwide: IARC CancerBase No. 11. Lyon, France: International Agency for Research on Cancer; 2013. Available from: http://globocan.iarc.fr, accessed on 14/01/2014.

[49] Travis WD, Brambilla E, Müller-Hermelink HK, Harris CC. Pathology and Genetics of Tumours of the Lung, Pleura, Thymus and Heart. Geneva: WHO Press; 2004.

[50] Koyama H, Ohno Y, Seki S, Nishio M, Yoshikawa T, Matsumoto S, et al. Magnetic resonance imaging for lung cancer. J Thorac Imaging 2013; 28:138-50.

[51] Christensen JD, Tong BC. Computed tomography screening for lung cancer: where are we now? N C Med J 2013; 74:406-410.

[52] Gohagan J, Marcus P, Fagerstrom R, Pinsky P, Kramer B, Prorok P, et al. Baseline findings of a randomized feasibility trial of lung cancer screening with spiral CT scan vs chest radiograph: the lung screening study of the National Cancer Institute. Chest 2004; 126:114–121.

[53] Gohagan J, Marcus P, Fagerstrom R, Pinsky P, Kramer B, Prorok P, et al. Final results of the Lung Screening Study, a randomized feasibility study of spiral CT versus chest X-ray screening for lung cancer. Lung Cancer 2005; 47:9-15.

[54] International Early Lung Cancer Action Program, Henschke CI, Yankelevitz DF, Libby DM, Pasmantier MW, Smith JP, et al. Survival of patients with stage I lung cancer detected on CT screening. N Engl J Med 2006; 355:1763–1771.

[55] Berrington de González A, Kim KP, Berg CD. Low-dose lung computed tomography screening before age 55: estimates of the mortality reduction required to outweigh the radiation-induced cancer risk. J Med Screen 2008; 15:153-158.

[56] US Preventive Services Task Force. Lung cancer screening: recommendation statement. Ann Intern Med. 2004; 140:738–739.

[57] Smith R, von Eschenbach A, Wender R, Levin B, Byers T, Rothenberger D, et al. American Cancer Society guidelines for the early detection of cancer: update of early detection guidelines for prostate, colorectal, and

endometrial cancers: also: update 2001 - testing for early lung cancer detection. CA Cancer J Clin 2001; 51:38–75.

[58] Beckmann N, Tigani B, Ekatodramis D, Borer R, Mazzoni L, Fozard JR. Pulmonary edema induced by allergen challenge in the rat: noninvasive assessment by magnetic resonance imaging. Magn Reson Med 2001; 45:88-95.

[59] Beckmann N, Tigani B, Mazzoni L, Fozard JR. MRI of lung parenchyma in rats and mice using a gradient-echo sequence. NMR Biomed 2001; 14:297-306.

[60] Quintana HK, Cannet C, Schaeublin E, Zurbruegg S, Sugar R, Mazzoni L, et al. Identification with MRI of the pleura as a major site of the acute inflammatory effects induced by ovalbumin and endotoxin challenge in the airways of the rat. Ame J Physiol - Lung C 2006; 291:L651-L657.

[61] Quintana HK, Cannet C, Zurbruegg S, Blé F-X, Fozard JR, Page CP, et al. Proton MRI as a noninvasive tool to asssess elastase-induced lung damage in spontaneously breathing rats. Magn Reson Med 2006; 56:1242–1250.

[62] Tigani B, Schaeublin E, Sugar R, Jackson AD, Fozard JR, Beckmann N. Pulmonary inflammation monitored noninvasively by MRI in freely breathing rats. Biochem Bioph Res Com 2002; 292:216-221.

[63] Tigani B, Cannet C, Zurbrügg S, Schaeublin E, Mazzoni L, Fozard JR, et al. Resolution of the oedema associated with allergic pulmonary inflammation in rats assessed noninvasively by magnetic resonance imaging. Brit J Pharmacol 2003; 140:239-246.

[64] Zurek M. IRM des poumons à temps d'echo courts: méthodes et applications à des modèles expérimentaux chez le rongeur. PhD Thesis. 2010, Université Calude Bernard Lyon 1, Lyon.

[65] Blé F-X, Cannet C, Zurbruegg S, Karmouty-Quintana H, Bergmann R, Frossard N, et al. Allergen-induced lung inflammation in actively sensitized mice assessed with MR imaging. Radiology 2008; 248:834-843.

[66] Zurek M, Boyer L, Caramelle P, Boczkowski J, Crémillieux Y. Longitudinal and noninvasive assessment of emphysema evolution in a murine model using proton MRI. Magn Reson Med 2012; 68:898-904.

[67] Olsson LE, Lindahl M, Onnervik PO, Johansson LB, Palmér M, Reimer MK, et al. Measurement of MR signal and T_2^* in lung to characterize a tight skin mouse model of emphysema using single-point imaging. J Magn Reson Imaging 2007; 25:488-94.

[68] Hatabu H, Alsop DC, Listerud J, Bonnet M, Gefter WB. T_2^* and proton density measurement of normal human lung parenchyma using submillisecond echo time gradient echo magnetic resonance imaging. Eur J Radiol 1999; 29:245-52.

[69] Yablonskiy DA, Haacke EM. Theory of NMR signal behavior in magnetically inhomogeneous tissues: the static dephasing regime. Magn Reson Med 1994; 32:749-763.

[70] Bauman G, Puderbach M, Deimling M, Jellus V, Chefd'hotel C, Dinkel J, et al. Non-contrast-enhanced perfusion and ventilation assessment of the human lung by means of Fourier decomposition in proton MRI. Magn Reson Med 2009; 62:656-664.

[71] Bernstein MA, King KF, Zhou XJ. Handbook of MRI pulse sequences. Burlington: Elsevier, Inc.; 2004. 1017 p.

[72] Karzai W, Cui X, Heinicke N, Niemann C, Gerstenberger EP, Correa R, et al. Neutrophil stimulation with granulocyte colony-stimulating factor worsen ventilation-induced lung injury and mortality in rats. Anesthesiology 2005; 103:996-1005.

[73] Walder B, Fontao E, Totsch M, Morel DR. Time and tidal volume-dependent ventilator-induced lung injury in healthy rats. Eur J Anaesthesiol 2005; 22:785-794.

[74] Haacke EM, Brown RW, Thompson MR, Venkatesan R. Magnetic resonance imaging. Physical principles and sequence design. New York: John Wiley & Sons, Ltd; 1999. 914 p.

[75] Block KT. Advanced methods for radial data sampling in magnetic resonance imaging. PhD Thesis. 2008, Georg-August-Universität Göttingen, Göttingen.

[76] Lauterbur PC. Image formation by induced local interactions: examples employing nuclear magnetic resonance. Nature 1973; 242:190-191.

[77] Magnetic resonance: an introduction to ultrashort TE (UTE) imaging. J Comput Assist Tomogr 2003; 27:825-846.

[78] Tyler DJ, Robson MD, Henkelman RM, Young IR, Bydder GM. Magnetic resonance imaging with ultrashort TE (UTE) pulse sequences: technical considerations. J Magn Reson Imaging 2007; 25:279-289.

[79] Egger C, Cannet C, Gérard C, Jarman E, Jarai G, Feige A, et al. Administration of bleomycin via oropharyngeal aspiration route leads to sustained lung fibrosis in mice and rats as quantified by UTE-MRI and histology. PLoS ONE 2013; 8:e63432.

[80] Takahashi M, Togao O, Obara M, van Cauteren M, Ohno Y, Doi S, et al. Ultra-short echo time (UTE) MR imaging of the lung: comparison between normal and emphysematous lungs in mutant mice. J Magn Reson Imaging 2010; 32:326-333.

[81] Togao O, Ohno Y, Dimitrov I, Hsia CC, Takahashi M. Ventilation/perfusion imaging of the lung using ultra-short echo time (UTE) MRI in an animal model of pulmonary embolism. J Magn Reson Imaging 2011; 34:539-546.

[82] Conti G, Tambalo S, Villetti G, Catinella S, Carnini C, Bassani F, et al. Evaluation of lung inflammation induced by intratracheal administration of LPS in mice: comparison between MRI and histology. Magn Res Mater Phy 2010; 23:93-101.

[83] Lederlin M, Crémillieux Y. Three-Dimensional Assessment of Lung Tissue Density Using a Clinical Ultrashort Echo Time at 3 Tesla: A Feasibility Study in Healthy Subjects. J Magn Reson Imaging. In press, doi: 10.1002/jmri.24429.

[84] Johnson KM, Fain SB, Schiebler ML, Nagle S. Optimized 3D ultrashort echo time pulmonary MRI. Magn Reson Med 2013; 70:1241–1250.

[85] Biederer J, Mirsadraee S, Beer M, Molinari F, Hintze C, Bauman G, et al. MRI of the lung (3/3)-current applications and future perspectives. Insights Imaging 2012; 3:373-386.

[86] Beckmann N, Tigani B, Sugar R, Jackson AD, Jones G, Mazzoni L, et al. Noninvasive detection of endotoxin-induced mucus hypersecretion in rat lung by MRI. Am J Physiol - Lung C 2002; 283:L22-L30.

[87] Beckmann N, Cannet C, Zurbruegg S, Rudin M, Tigani B. Proton MRI of lung parenchyma reflects allergen-induced airway remodeling and endotoxin-aroused hyporesponsiveness: a step toward ventilation studies in spontaneously breathing rats. Magn Reson Med 2004; 52:258-268.

[88] Marzola P, Lanzoni A, Nicolato E, Di Modugno V, Cristofori P, Osculati F, et al. (1)H MRI of pneumococcal pneumonia in a murine model. J Magn Reson Imaging 2005; 22:170-174.

[89] Babin AL, Cannet C, Gérard C, Saint-Mezard P, Page CP, Sparrer H, et al. Bleomycin-induced lung injury in mice investigated by MRI: model assessment for target analysis. Magn Reson Med 2012; 67:499-509.

[90] Babin AL, Cannet C, Gérard C, Wyss D, Page CP, Beckmann N. Non-invasive assessment of bleomycin-induced lung injury and the effects of short-term glucocorticosteroid treatments in rats using MRI. J Magn Reson Imaging 2011; 33:603-614.

[91] Mosbah K, Ruiz-Cabello, Berthezène Y, Crémillieux Y. Aerosols and gaseous contrast agents for magnetic resonance imaging of the lung. Contrast Media Mol Imaging 2008. 3:173-190.

[92] Merbach AE, Toth E. The chemistry of contrast agents in medical magnetic resonance imaging. New York: John Wiley & Sons, Ltd; 2001. 471 p.

[93] Runge VM. Contrast media. In: Runge VM, editor. Clinical MRI. Philadelphia: W.B. Saunders; 2002. pp. 454-472.

[94] Berthezène Y, Vexler V, Clément O, Mühler A, Moseley ME, Brasch RC. Contrast-enhanced MR imaging of the lung: assessments of ventilation and perfusion. Radiology 1992; 183:667-672.

[95] Berthezène Y, Mulher A, Lang P, Shames D, Clement O, Rosenay W, et al. Safety aspects and pharmacokinetics of inhaled aerosolized Gadolinium. J Magn Reson Imaging 1993; 3:125-130.

[96] Haage P, Karaagac S, Adam G, Glowinski A, Günther RW. Comparison of aerosolized gadoteridol and gadopentetate dimeglumine for magnetic resonance ventilation imaging of the lung. Magn Reson Med 2001; 46:803-806.

[97] Suga K, Yuan Y, Nobuhiko O, Okada M, Kawakami Y, Matsunaga N. Potential of magnetic resonance lymphography with intrapulmonary injection of Gadopentetate Dimeglumine for visualization of the pulmonary lymphatic basin in dogs: preliminary results. Invest Radiol 2003; 38:679-689.

[98] Sood BG, Shen Y, Latif Z, Chen X, Sharp J, Neelavalli J, et al. Aerosol delivery in ventilated newborn pigs: an MRI evaluation. Pediatr Res 2008; 64:159-164.

[99] Nakamura H, Ito N, Kotake F, Mizokami Y, Matsuoka T. Tumor-detecting capacity and clinical usefulness of SPIO-MRI in patients with hepatocellular carcinoma. J Gastroenterol 2000; 35:849-855.

[100] Corot C, Warlin D. Superparamagnetic iron oxide nanoparticles for MRI: contrast media pharmaceutical company R&D perspective. Wiley Interdiscip Rev Nanomed Nanobiotechnol 2013; 5:411-422.

[101] Hilger I, Ändra W, Bähring R, Daum A, Hergt R, Kaiser WA. Evaluation of temperature increase with different amounts of magnetite in liver tissue samples. Invest Radiol 1997; 32:705-712.

[102] Strobel K, Hoerr V, Schmid F, Wachsmuth L, Löffler B, Faber C. Early detection of lung inflammation: Exploiting T1-effects of iron oxide particles using UTE MRI. Magn Reson Med 2012; 68:1924-1931.

[103] Goodson BM. Nuclear magnetic resonance of laser-polarized noble gases in molecules, materials, and organisms. J Magn Reson 2002; 155:157–216.

[104] Möller HE, Chen XJ, Saam B, Hagspiel KD, Johnson GA, Altes TA, et al. MRI of the lungs using hyperpolarized noble gases. Magn Reson Med 2002; 47:1029–1051.

[105] Fain S, Schiebler ML, McCormack DG, Parraga G. Imaging of lung function using hyperpolarized helium-3 magnetic resonance imaging: review of current and emerging translational methods and applications. J Magn Reson Imaging 2010; 32:1398-1408.

[106] Ouriadov A, Farag A, Kirby M, McCormack DG, Parraga G, Santyr GE. Lung morphometry using hyperpolarized (129) Xe apparent diffusion coefficient anisotropy in chronic obstructive pulmonary disease. Magn Reson Med 2013; 70:1699-1706.

[107] Owrangi AM, Wang JX, Wheatley A, McCormack DG, Parraga G. Quantitative (1)H and hyperpolarized (3)He magnetic resonance imaging: comparison in chronic obstructive pulmonary disease and healthy never-smokers. Eur J Radiol 2014; 83:64-72.

[108] Aysola R, de Lange EE, Castro M, Altes TA. Demonstration of the heterogeneous distribution of asthma in the lungs using CT and hyperpolarized helium-3 MRI. J Magn Reson Imaging 2010; 32:1379-1387.

[109] Tzeng Y-S, Lutchen K, Albert M. The difference in ventilation heterogeneity between asthmatic and healthy subjects quantified using hyperpolarized 3He MRI. J of Appl Physiol 2009; 106:813-822.

[110] Thomas AC, Potts EN, Chen BT, Slipetz DM, Foster WM, Driehuys B. A robust protocol for regional evaluation of methacholine challenge in mouse models of allergic asthma using hyperpolarized 3He MRI. NMR Biomed 2009; 22:502-515.

[111] Driehuys B, Walker J, Pollaro J, Cofer GP, Mistry N, Schwartz D, et al. 3He MRI in mouse models of asthma. Magn Reson Med 2007; 58:893-900.

[112] Peterson ET, Dai J, Holmes JH, Fain SB. Measurement of lung airways in three dimensions using hyperpolarized helium-3 MRI. Phys Med Biol 2011; 56:3107-3122.

[113] Wang C, Altes TA, Mugler JP, Miller GW, Ruppert K, Mata JF, et al. Assessment of the lung microstructure in patients with asthma using hyperpolarized 3He diffusion MRI at two time scales: comparison with healthy subjects and patients with COPD. J Magn Reson Imaging 2008; 28:80-88.

[114] Heidelberger E, Lauterbur PC. Gas phase 19F NMR zeugmatography: a new approach to lung ventilation imaging. First Annual Meeting of the Society of Magnetic Resonance Medicine 1982; 70–71.

[115] Kuethe DO, Caprihan A, Fukushima E, Waggoner RA. Imaging lungs using inert fluorinated gases. Magn Reson Med 1998; 38:85–88.

[116] Conradi MS, Saam MS, Yablonskiy DA,Woods JC. Hyperpolarized 3He and perfluorocarbon gas diffusion MRI of lungs. Progr NMR Spectrosc 2006; 48:63–83.

[117] Schreiber WG, Eberle B, Laukemper-Ostendorf S, Markstaller K, Weiler N, Scholz A, et al. Dynamic 19F-MRI of pulmonary ventilation using sulfur hexafluoride (SF6) gas. Magn Reson Med 2001; 45: 605–613.

[118] Kuethe DO, Caprihan A, Gach M, Lowe IJ, Fukushima E. Imaging obstructed ventilation with NMR using inert fluorinated gases. J Appl Physiol 2000; 88:2279–2286.

[119] Ruiz-Cabello J, Perez-Sanchez JM, Perez de Alejo R, Rodriguez I, Gonzalez-Mangado N, Peces-Barba G, et al. Diffusion-weighted 19F-MRI of lung periphery: influence of pressure and air-SF6 composition on apparent diffusion coefficients. Respir Physiol Neurobiol 2005; 148:43–46.

[120] Edelman RR, Hatabu H, Tadamura E, Li W, Prasad PV. Noninvasive assessment of regional ventilation in the human lung using oxygen-enhanced magnetic resonance imaging. Nat Med 1996; 2:1236–1239.

[121] Ohno Y, Koyama H, Matsumoto K, Onishi Y, Nogami M, Takenaka D, et al. Oxygen-enhanced MRI vs. quantitatively assessed thin-section CT: pulmonary functional loss assessment and clinical stage classification of asthmatics. Eur J Radiol 2011; 77:85-91.

[122] Ohno Y, Koyama H, Nogami M, Takenaka D, Matsumoto S, Obara M, et al. Dynamic oxygen-enhanced MRI versus quantitative CT: pulmonary functional loss assessment and clinical stage classification of smoking-related COPD. Am J Roentgenol 2008; 190:W93-99.

[123] Stadler A, Stiebellehner L, Jakob PM, Arnold JF, Eisenhuber E, von Katzler I, et al. Quantitative and o(2) enhanced MRI of the pathologic lung: findings in emphysema, fibrosis, and cystic fibrosis. Int J Biomed Imaging 2007; 2007:23624.

[124] Ohno Y, Hatabu H, Takenaka D, Adachi S, Van Cauteren M, Sugimura K. Oxygen-enhanced MR ventilation imaging of the lung: preliminary clinical experience in 25 subjects. Am J Roentgenol 2001; 177:185–194.

[125] Mai VM, Liu B, Li W, Polzin J, Kurucay S, Chen Q, et al. Influence of oxygen flow rate on signal and T(1) changes in oxygen-enhanced ventilation imaging. J Magn Reson Imaging 2002; 16:37–41.

[126] Runge VM, Clanton JA, Lukehart CM, Partain CL, James AE. Paramagnetic agents for contrast-enhanced NMR: a review. Am J Roentgenol 1983; 141:1209-1215.

[127] Greenwood NN, Earnshaw A. Chemistry of the elements. Oxford: Pergamon Press; 1984. 1243 p.

[128] Lai CM, Lauterbur PC. True three-dimensional image reconstruction by nuclear magnetic resonance zeugmatography. Phys Med Biol 1981; 26:851–856.

[129] Bruker Paravision 5.1. User manual, Section A, Chapter 6: Measurements Methods. Ettlingen, Germany: Bruker BioSpin GmbH. 2010.

[130] Jackson JI, Meyer CH, Nishimura DG, Macovski A. Selection of a convolution function for Fourier inversion using gridding. IEEE Trans Med Imaging 1991; 10:473–478.

[131] Maeda A, Sano K, Yokoyama T. Reconstruction by weighted correlation for MRI with time-varying gradients. IEEE Trans Med Imaging 1988; 7:26–31.

[132] Pauly JM. Reconstruction of non-Cartesian k-Space data. International Society of Magnetic Resonance in Medicine, Salt Lake City, USA. Proceeding ISMRM 21 (2013).

[133] Aurenhammer F. Voronoi diagrams - a survey of a fundamental geometric data structure. ACM Comput Surv 1991; 23:345–405.

[134] Wajer FTAW, Lethmate R, de Jong RAJ, Martinez LT, Graveron-demilly D, Fuderer M, et al. MR image reconstruction from sparse and corrupted k-space data. Proc ProRISC/IEEE Ben Work Circ Syst Sign Process, Mierlo (The Netherlands) 1999; 577-584

[135] Ramachandran GN, Lakshminarayanan AV. Three-dimensional reconstruction from radiographs and electron micrographs: application of convolutions instead of Fourier transforms. In Proc Natl Acad Sci USA 1971; 68: 2236–2240.

[136] Joseph PM. Sampling errors in projection reconstruction MRI. Magn Reson Med 1998; 40:460–466.

[137] O'Sullivan JD. A fast function algorithm for Fourier inversion in computer tomography. IEEE Trans Med Imaging 1985; 4:200-207.

[138] Beatty PJ, Nishimura DG, Pauly JM. Rapid gridding reconstruction with a minimal oversampling ratio. IEEE Transactions on Medical Imaging 2005; 24:799–808.

[139] Van Echteld CJA, Beckmann N. A view on imaging in drug research and development for respiratory diseases. J Pharmacol Exp Ther 2011; 337:335-349.

[140] Weissleder R, Pittet MJ. Imaging in the era of molecular oncology. Nature 2008; 452:580-589.

[141] Choi HS, Liu W, Misra P, Tanaka E, Zimmer JP, Itty Ipe B, et al. Renal clearance of nanoparticles. Nat Biotech 2007; 25:1165-1170.

[142] Cai WB, Chen K, Li ZB, Gambhir SS, Chen X. Dual-function probe for PET and near-infrared fluorescence imaging of tumor vasculature. J Nucl Med 2007; 48:1862-1870.

[143] Alric C, Taleb J, Le Duc G, Mandon C, Billotey C, Le Meur-Herland A, et al. Gadolinium chelate coated gold nanoparticles as contrast agents for both X-ray computed tomography and magnetic resonance imaging. J Am Chem Soc 2008; 130:5908-5915.

[144] Choi HS, Liu W, Liu F, Nasr K, Misra P, Bawendi MG, et al. Design considerations for tumour-targeted nanoparticles. Nat Nano 2010; 5:42-47.

[145] Lux F, Mignot A, Mowat P, Louis C, Dufort S, Bernhard C, et al. Ultrasmall rigid particles as multimodal probes for medical applications. Angew Chem 2011; 123:12507-12511.

[146] Mignot A, Truillet C, Lux F, Sancey L, Louis C, Denat F, et al. A top-down synthesis route to ultrasmall multifunctional Gd-based nanoparticles for theranostic applications. Chem Eur J 2013; 19:6122-6136.

[147] Le Duc G, Miladi I, Alric C, Mowat P, Bräuer-Krisch E, Bouchet A, et al. Toward an image-guided microbeam radiation therapy using Gadolinium-based nanoparticles. ACS Nano 2011; 5:9566-9574.

[148] Kryza D, Taleb J, Janier M, Marmuse L, Miladi I, Bonazza P, et al. Biodistribution study of nanometric hybrid gadolinium oxide particles as a multimodal SPECT/MR/optical imaging and theragnostic agent. Bioconjugate Chem 2011; 22:1145-1152.

[149] Maeda H, Wu J, Sawa T, Matsumura, Hori K. Tumor vascular permeability and the EPR effect in macromolecular therapeutics: a review. J Controlled Release 2000; 65:271-284.

[150] Matsumura Y, Maeda H. A new concept for macromolecular therapeutics in cancer chemotherapy: mechanism of tumoritropic accumulation of proteins and the antitumor agent smancs. Cancer Res 1986; 46:6387-6392.

[151] Gelfand EW. Pro: mice are a good model of human airway disease. Am J Respir Crit Care Med 2002; 166:5–6.

[152] Kumar RK, Foster PS. Modeling allergic asthma in mice: pitfalls and opportunities. Am J Respir Cell Mol Biol 2002; 27:267–272.

[153] Leong KP, Huston DP. Understanding the pathogenesis of allergic asthma using mouse models. Ann Allergy Asthma Immunol 2001; 87:96–109.

[154] Wills-Karp M. Murine models of asthma in understanding immune dysregulation in human asthma. Immunopharmacology 2000; 48:263–268

[155] Henderson RW Jr, Tang L-O, Chu S-J, Tsao S-M, Chiang GKS, Jones F, et al. A role for cysteinyl leukotrienes in airway remodeling in a mouse asthma model. Am J Respir Crit Care Med 2002; 165:108-116.

[156] Lederlin M, Ozier A, Montaudon M, Begueret H, Ousova O, Marthan R, et al. Airway remodeling in a mouse asthma model assessed by in-vivo respiratory-gated micro-computed tomography. Eur Radiol 2010; 20:128-137.

[157] Lederlin M, Ozier A, Dournes G, Ousova O, Girodet P-O, Begueret H, et al. In vivo micro-CT assessment of airway remodeling in a flexible OVA-sensitized murine model of asthma. PLoS One 2012; 7:e48493.

[158] Bianchi A, Ozier A, Ousova O, Raffard G, Crémillieux Y. UTE MRI longitudinal non-invasive characterization of a mouse model of chronic asthma: from inflammation to bronchial remodeling assessment. International Society of Magnetic Resonance in Medicine, Salt Lake City, USA. Proceeding ISMRM 21 (2013), p. 643.

[159] Meyer A, Auernheimer J, Modlinger A, Kessler H. Targeting RGD recognizing integrins: drug development, biomaterial research, tumor imaging and targeting. Curr Pharm Des 2006; 12:2723-2747.

[160] Brooks PC, Clark RA, Cheresh DA. Requirement of vascular integrin alpha v beta 3 for angiogenesis. Science 1994; 264:569-571.

[161] Max R, Gerritsen RR, Nooijen PT, Goodman SL, Sutter A, Keilholz U. et al. Immunohistochemical analysis of integrin alpha v beta 3 expression on tumor-associated vessels of human carcinomas. Int J Cancer 1997; 71:320-324.

[162] Chen X, Sievers E, Hou Y, Park R, Tohme M, Bart R, et al. Integrin alpha v beta 3-targeted imaging of lung cancer. Neoplasia 2005; 7:271–279.

[163] Sato T, Konishi K, Kimura H, K. Maeda K, K. Yabushita K, M. Tsuji M, et al. Vascular integrin beta 3 and its relation to pulmonary metastasis of colorectal carcinoma. Anticancer Res 2001; 21:643–647.

[164] Heckmann D, Meyer A, Marinelli L, Zahn G, Stragies R, Kessler H. Probing integrin selectivity: rational design of highly active and selective ligands for the alpha5beta1 and alphavbeta3 integrin receptor. Angew Chem Int Ed Engl 2007; 46:3571–3574.

[165] Liu S. Radiolabeled multimeric cyclic RGD peptides as integrin alphavbeta3 targeted radiotracers for tumor imaging. Mol Pharm 2006; 3:472-487.

[166] Morlieras J, Dufort S, Sancey L, Truillet C, Mignot A, Rossetti F, et al. Functionalization of small rigid platforms with cyclic RGD peptides for targeting tumors overexpressing $\alpha_v\beta_3$-integrins. Bioconjug Chem 2013; 24:1584-1597.

[167] Driscoll KE, Costa DL, Hatch G, Henderson R, Oberdorster G, Salem H., et al. Intratracheal instillation as an exposure technique for the evaluation of respiratory tract toxicity: uses and limitations. Toxicol Sci 2000; 55:24-35.

[168] Costa DL, Lehmann JR, Winsett D, Richards J, Ledbetter AD, Dreher KL. Comparative pulmonary toxicological assessment of oil combustion particles following inhalation or instillation exposure. Toxicol Sci 2006; 91:237-246.

[169] Shoyele SA, Cawthome S. Particle engineering techniques for inhaled biopharmaceuticals. Adv Drug Deliver Rev 2006; 58:1009-1029.

[170] Center for Drug Evaluation and Research (CDER). Guidance for industry. Single dose acute toxicity testing for pharmaceuticals. Food and Drug Administration (FDA). August 1996. http://www.fda.gov/downloads/Drugs/GuidanceComplianceRegulatoryInformation/Guidances/ucm079270.pdf

[171] Aebischer A, Hostettler M, Hauser J, Krämer K, Weber T, Güdel HU, et al. Structural and spectroscopic characterization of active sites in a family of light-emitting sodium Lanthanide tetrafluorides. Angew Chem Int Ed 2006; 45:2802-2806.

[172] Groult H, Bianchi A, Zamai M, Ruiz-Cabello J, Crémillieux Y, Herranz F. MRI and fluorescence imaging with upconverting nanoparticles: a

new multimodal approach for lung targeting. International Society of Magnetic Resonance in Medicine, Salt Lake City, USA. Proceeding ISMRM 21 (2013), p. 3901.

[173] Gerbino AJ, Glenny RW. Lung albumin accumulation is spatially heterogeneous but not correlated with regional pulmonary perfusion. J Appl Physiol 2002; 92:279-287.

[174] Koretsky AP, Silva AC. Manganese-enhanced magnetic resonance imaging (MEMRI). NMR Biomed 2004; 17:527-531.

[175] Yin Z, Aschner JL, dos Santos AP, Aschner M. Mitochondrial-dependent manganese neurotoxicity in rat primary astrocyte cultures. Brain Res 2008; 1203:1–11.

[176] Wendland MF. Applications of manganese-enhanced magnetic resonance imaging (MEMRI) to imaging of the heart. NMR Biomed 2004; 17: 581–594.

[177] Gobbo OL, Zurek M, Tewes F, Ehrhardt C, Crémillieux Y. Manganese: a new contrast agent for lung imaging? Contrast Media Mol Imaging 2012; 7:542-546.

List of Publications, Patent, and Communications

Publications

- *Targeting and in vivo imaging of non-small-cell lung cancer using nebulized multimodal contrast agents*. A. Bianchi, S. Dufort, P.-Y. Fortin, F. Lux, N. Tassali, O. Tillement, J.-L. Coll, Y. Crémillieux. *Proceedings of National Academy of Sciences USA*, 111(25):9247-9252 (2014).
  http://www.pnas.org/content/early/2014/06/04/1402196111.abstract

- *In vivo Magnetic Resonance Imaging for effective non-invasive detection and follow-up of an orthotopic mouse model of lung cancer*. A. Bianchi, S. Dufort, P.-Y. Fortin, F. Lux, G. Raffard, N. Tassali, O. Tillement, J.-L. Coll, Y. Crémillieux. *NMR in Biomedicine*, doi:10.1002/nbm.3142, in press.
  http://onlinelibrary.wiley.com/doi/10.1002/nbm.3142/abstract

- *Quantitative biodistribution and pharmacokinetics of theranostic multimodal gadolinium-based nanoparticles for lungs using Ultrashort-TE MRI*. A. Bianchi, S. Dufort, F. Lux, A. Courtois, O. Tillement, J.-L. Coll, Y. Crémillieux. *Magnetic Resonance Materials in Physics, Biology and Medicine*, doi:10.1007/s10334-013-0412-5, in press.
  http://link.springer.com/article/10.1007%2Fs10334-013-0412-5

- *Ultrashort-TE MRI longitudinal study and characterization of a chronic model of asthma in mice: inflammation and bronchial remodeling assessment*. A. Bianchi, A. Ozier, G. Raffard, O. Ousova, Y. Crémillieux. *NMR in Biomedicine*, 26(11):1451-1459 (2013).
  http://onlinelibrary.wiley.com/doi/10.1002/nbm.2975/pdf

- *Contrast enhanced lung MRI in mice using ultra-short echo time radial imaging and intratracheally administrated Gd-DOTA-based nanoparticles*. A. Bianchi, F. Lux, O. Tillement, Y. Crémillieux. *Magnetic Resonance in Medicine*, 70:1419–1426 (2013).
  http://onlinelibrary.wiley.com/doi/10.1002/mrm.24580/pdf

- *The use of theranostic gadolinium-based nanoprobes to improve radiotherapy efficacy*. L. Sancey, F. Lux, S. Kotb, S. Roux, S. Dufort, A. Bianchi, Y. Crémillieux, *et al. British Journal of Radiology,* doi:10.1259/bjr.20140134, in press.
  http://www.birpublications.org/doi/abs/10.1259/bjr.20140134

Publications submitted or in preparation

- *Nebulized gadolinium-based nanoparticles: a theranostic approach for lung tumor imaging and radiosensitization*. S. Dufort, A. Bianchi, H. Maxime, F. Lux, G. Le Duc, V. Josserand, C. Louis, P. Perriat, Y. Crémillieux, O. Tillement, J.-L. Coll. *Small,* submitted.

- *Intratracheal administration of ultra-small Gd-based nanoparticles: a new protocol for brain tumor targeting*. A. Bianchi, D. Moncelet, F. Lux, E.J. Ribot, O. Tillement, P. Voisin, Y. Crémillieux. *Contrast Media and Molecular Imaging,* in preparation.

- *Upconverting nanoparticles: a new multimodal approach for lung targeting*. H. Groult, J. Ruiz-Cabello, A. Bianchi, M. Zamai, Y. Crémillieux, F. Herranz. *ACS Nano,* in preparation.

Patent

Nanoparticules ultrafines comme agent de contraste multimodale. Y. Crémillieux, A. Bianchi, S. Dufort, J.-L. Coll, F. Lux, O. Tillement. *National Patent FR 12 53438*
International Patent WO 2013/153197 (A1) published in October 2013.
http://worldwide.espacenet.com/publicationDetails/biblio?FT=D&date=20131017&DB=EPODOC&locale=en_EP&CC=WO&NR=2013153197A1&KC=A1&ND=4

Oral communications

- *Intratracheal administration of Gd-based nanoparticles: an effective approach for MRI detection and follow-up of lung tumor*. A. Bianchi*, S. Dufort,F. Lux, N. Tassali, P.-Y. Fortin, O. Tillement, J.-L. Coll, Y. Crémillieux. International Society of Magnetic Resonance in Medicine, Milan, Italy. Proceeding ISMRM 22 (2014), p. 0290.

- *Theranostic multimodal nanoparticles and lung MRI: a winning combination for lung cancer diagnostic and therapy?*. A. Bianchi, S. Dufort, F. Lux, N. Tassali, J.-L. Coll, O. Tillement, Y. Crémillieux*. Contrast Media Research (CMR) symposium, November 2013, Beijing, China.
- *MRI UTE applications in mice models of lung diseases*. A. Bianchi*. International Workshop 'Lung - from molecule to image', September 2013, Bordeaux, France.
- *Theranostic nanoparticles for lung tumors*. F. Lux*, A. Bianchi, S. Dufort, N. Tassali, J.–L. Coll, Y. Crémillieux, O. Tillement. COST Action TD 1004 Annual Meeting, September 2013, Athens, Greece.
- *Intratracheal administration of multimodal gadolinium-based nanoparticles: a new approach for lung tumor imaging*. A. Bianchi*, S. Dufort, F. Lux, N. Tassali, O. Tillement, J.-L. Coll, Y. Crémillieux. Structure Fédérative de Recherche (SFR) Technologies pour la Santé, June 2013, Bordeaux, France.
- *Contrast-enhanced MRI of lung tissue using intra-tracheal delivery of multimodal nanoparticles (AGuIX®): proof-of-concept and preliminary results* . A. Bianchi, S. Dufort, F. Lux, N. Tassali, J.-L. Coll, O. Tillement, Y. Crémillieux*. Nanohybrides 10 workshop, May 2013, Porquerolles, France.
- *Ciblage et thérapie des tumeurs pulmonaires : une approche originale par administration intra-pulmonaire de nanoparticules théranostiques*. S. Dufort*, F. Lux, A. Bianchi, Y. Crémillieux, C. Louis, O. Tillement, J.-L. Coll. Nanohybrides 10 workshop, May 2013, Porquerolles, France.
- *Multimodal nanoparticles to highlight lung tumours by two different pathways*. A. Bianchi, S. Dufort, F. Lux*, J.-L. Coll, O. Tillement, Y. Crémillieux. European Molecular Imaging Meeting Proceedings, n. 75 (2013), May 2013, Turin, Italy.
- *UTE MRI longitudinal non-invasive characterization of a mouse model of chronic asthma: from inflammation to bronchial remodeling assessment*. A. Bianchi*, A. Ozier, O. Ousova, G. Raffard, Y. Crémillieux. International Society of Magnetic Resonance in Medicine, Salt Lake City, USA. Proceeding ISMRM 21 (2013), p. 643.
- *High-resolution pre-clinical lung proton MRI: new applications and challenges*. A. Bianchi* and Y. Crémillieux. Structure Fédérative de Recherche (SFR) Technologies pour la Santé, October 2012, Bordeaux, France.

- *Multimodal gadolinium based nanoprobes for lung investigations*. F. Lux*, S. Dufort, A. Bianchi, V. Josserand, O. Tillement, J.-L. Coll, Y. Crémillieux. World Molecular Imaging Congress Proceedings SS 39 (2012), Dublin, Ireland.

- *MRI techniques for pre-clinical lung imaging: updates*. A. Bianchi*. Mid-Term Π-Net Review Meeting, September 2012, Palma de Mallorca, Spain.

- *Lighting-up the lungs: an UTE MRI investigation of the parenchyma signal enhancement due to intra-tracheal administration of an innovative Si-based Gd contrast agent*. A. Bianchi*, F. Lux, G. Dournes, O. Tillement, Y. Crémillieux, International Society of Magnetic Resonance in Medicine, Melbourne, Australia. Proceeding ISMRM 20 (2012), p. 628.

- *MRI techniques for pre-clinical lung imaging*. A. Bianchi*. First Π-Net Annual Meeting, December 2011, Sheffield, UK.

**Oral presenter*

Posters

- *Intratracheal administration of ultra-small Gd-based nanoparticles: a new protocol for brain tumor targeting* . A. Bianchi*, D. Moncelet, F. Lux, E.J. Ribot, N. Tassali, V. Bouchaud, O. Tillement, P. Voisin, Y. Crémillieux. International Society of Magnetic Resonance in Medicine, Milan, Italy. Proceeding ISMRM 22 (2014), p. 4031.

- *Quantitative biodistribution and Pharmacokinetics of theranostic multi-modal gadolinium-based nanoparticles for lungs using Ultrashort-TE MRI*. A. Bianchi*, S. Dufort, F. Lux, A. Courtois, O. Tillement, J.-L. Coll, Y. Crémillieux. European Society of Magnetic Resonance in Medicine and Biology, Toulouse, France. Proceeding ESMRMB (2013), p. 166 (Abstract 47379).

- *Nanoparticules théranostiques et cancer du poumon : une approche originale par administration intra-pulmonaire*. S. Dufort*, A. Bianchi, F. Lux, C. Louis, Y. Crémillieux, O. Tillement and J.-L. Coll. Journées de recherche respiratoire (J2R), October 2013, Montpellier, France.

- *Absolute concentration, biodistribution and pharmacokinetics of Gd-based contrast agents in lungs using UTE MRI*. A. Bianchi*, S. Dufort, F. Lux, J.-L. Coll, O. Tillement, Y. Crémillieux. International Society of Magnetic

Resonance in Medicine, Salt Lake City, USA. Proceeding ISMRM 21 (2013), p. 4102.

- *MRI and fluorescence imaging with upconverting nanoparticles: a new multimodal approach for lung targeting*. H. Groult, A. Bianchi*, M. Zamai, J. Ruiz-Cabello, Y. Crémillieux, F. Herranz. International Society of Magnetic Resonance in Medicine, Salt Lake City, USA. Proceeding ISMRM 21 (2013), p. 3901.

- *Aérosolisation de nanoparticules théranostiques ciblantes dans le cancer du poumon*. S. Dufort*, F. Lux, C. Louis, A. Bianchi, Y. Crémillieux, V. Josserand, O. Tillement and J.-L. Coll. Journées de recherche respiratoire (J2R), October 2012, Lille, France. Proceeding on 'Revue des Maladies Respiratoires Actualité', Vol 4, Octobre 2012, Numéro Spécial, pag. 23, n. 43.

- *UTE MRI investigation of a chronic asthma mouse model: quantification of peribronchovascular inflammation and correlation with airways hyperresponsiveness*. A. Bianchi*, G. Raffard, O. Ousova, A. Ozier, Y. Crémillieux. International Society of Magnetic Resonance in Medicine, Melbourne, Australia. Proceeding ISMRM 20 (2012), p. 3972.

- *IRM pulmonaire: vers une imagerie haute résolution du poumon*. A. Bianchi*, G. Raffard, O. Ousova, A. Ozier, Y. Crémillieux. Société Française de Résonance Magnétique en Biologie et Médicine (SFRMBM), March 2012, Marseille, France.

**Poster presenter*

Awards

- *First prize awarded by the ISMRM Cancer Study Group* , International Society of Magnetic Resonance in Medicine, Milan, Italy. For: Proceeding ISMRM 22 (2014), p. 4031.

- *Summa Cum Laude ISMRM Merit Award* , International Society of Magnetic Resonance in Medicine, Milan, Italy. For: Proceeding ISMRM 22 (2014), p. 0290.

- *Magna Cum Laude ISMRM Merit Award* , International Society of Magnetic Resonance in Medicine, Milan, Italy. For: Proceeding ISMRM 22 (2014), p. 4031.

- *Best oral presentation award* , Structure Fédérative de Recherche (SFR) Technologies pour la Santé, June 2013, Bordeaux, France.
- *Summa Cum Laude ISMRM Merit Award* , International Society of Magnetic Resonance in Medicine, Salt Lake City, USA. For: Proceeding ISMRM 21 (2013), p. 643.
- *Magna Cum Laude ISMRM Merit Award* , International Society of Magnetic Resonance in Medicine, Melbourne, Australia. For: Proceeding ISMRM 20 (2012), p. 628.
- *First prize for best poster in MRI methodology category* , Société Française de Résonance Magnétique en Biologie et Médecine (SFRMBM), March 2012, Marseille, France.

Scientific Event Organization

Workshop 'Lung - from molecule to image' , Member of the Local Organizing Committee, September 2013, Bordeaux (France).
https://www.pi-network.eu/events/workshop-lung-from-molecule-to-image

Acknowledgements

"At times our own light goes out and is rekindled by a spark from another person. Each of us has cause to think with deep gratitude of those who have lighted the flame within us."

Albert Schweitzer - Nobel Peace Prize in 1952

Arrived at the end of this adventure, it is my pleasure to express my deepest gratitude to everyone who contributed to my work and supported me throughout the whole thesis project.

First of all, I want to thank Dr. Yannick Crémillieux, for his invaluable support, his priceless guidance, and his wise suggestions. I am very grateful to him for having given me the opportunity to begin this amazing work and life experience in the wonderful Bordeaux. Thank you for having given value to my opinions and my ideas since the very first moment, for being always available to answer my questions and to discuss my project. Thank you also for having introduced and guided me through the challenging world of MRI, publications, and conferences. I hope that we will have the possibility to work again together in the future. *Merci beaucoup Yannick!*

I would like to acknowledge Pr. Roger Marthan for welcoming me at the Cardio-thoracic Center of Bordeaux from April 2011 to December 2012. I wish to thank Pr. Jean-Michel Franconi for his warm welcome at the Center for Magnetic Resonance of Biological Systems from January 2013 until now, for his kindness and for having accepted to be an invited member of the jury of this work.

I wish to express my gratitude to Dr. Emmanuel Barbier and Dr. Patrick Berthault for having accepted the demanding work of being reviewer of this thesis. Thank you very much to Dr. Bruno Quesson for having accepted to be member of the jury despite the very short notice. I am very grateful to Dr. Nicolau Beckmann for having accepted to be part of the jury; his publications have inspired my work through my whole project and it is an honour for me

to discuss my results with him. *Muito obrigado!* A special thank you is for Dr. François Lux, for having accepted to be part of the jury but also for the long discussions during the project, for his prompt replies to my questions about his nanoparticles, and for his motivation and dynamism.

I owe many thanks to Dr. Olga Ousova for all the things she has taught me about animal dissection and biological handlings, helping me to become autonomous in performing a number of biological tasks. Thanks to Dr. Marc Biran and Dr. Sylvan Miraux for their help with the MRI scanners, to Dr. Pierre-Yves Fortin for his help with optical imaging, and to Dr. Arnaud Courtois for his kindness, patience and help with toxicological studies. A special thank you is for Dr. Gérard Raffard, for his precious help with any MRI-related technical issue, for his *bricolage* capacities and his prompt debugging interventions. Thanks to Stéphane Sanchez for all the technical support he gave me in animal handling-related issues.

I would like to acknowledge all the collaborators from the University of Lyon and Grenoble: Dr. Sandrine Dufort, Dr. Jean-Luc Coll, and Dr. Olivier Tillement. Thanks for all the fruitful discussions during the several meetings we had and for your enthusiasm, which brought to several publications and good results.

Many thanks to Pr. Jesus Ruiz-Cabello for the coordination of the Π – *net* Network. I take the chance to acknowledge here the fellowship from the European Network Π – *net* (FP7-PEOPLE-2010-ITN-264864) which has made this project possible. Being part of this International Network has allowed me to discuss with some of the most prominent scientists in the field of lung MRI, to take part to prestigious conferences and courses worldwide, and to meet some special guys who have become good friends. A special thanks is therefore dedicated to Felix, Hugo and Alessia, for having shared ups and downs during my doctoral experience and for understanding me so well.

Thank you to *all* the numerous colleagues and office mates I met during my stay at the CRCTB and CRMSB, especially to Imane and Diana for welcoming me at the very beginning and making the start (and not only!) of my adventure so nice. Special thanks to Jennifer for the long discussions, chats and for her continuous support. Thank you also to Damien, for the fruitful collaboration we started and accomplished in a short time. My deep gratitude to Nafiisha, for having supported me during these three years, for having become a good friend, for sharing good coffees and restaurants, for the long

chats and the nice evenings spent outside together. I am sure we will meet often around the world.

A special thank you is for Tom and James, for the great dinners we had together, the nice discussions and their kindness and support from the very first day we met.

Thank you very much to Nespresso, for having kept me awake during long evenings in the lab and for having helped this Italian to feel like at home with all-day-long great coffees.

Special thanks to Thibaut for his continuous and invaluable support and his patience during these last very intense months, for the nice trips together and his precious help with my French.

This thesis has been carried out in three years. Nonetheless, it is the results of several years of hard work and difficult choices which have eventually brought me to this PhD project. I want therefore to express my deepest gratitude to my long-standing friends in Geneva, London, Paris, Delft, Bilbao, Rome and Milan. You have been able to be so close to me when I needed it, even if we were so far by. Last, but not least, I want to thank my family for having supported me in all my choices and for being always on my side, wherever I go, whenever I need.

Grazie!